Visualizing the Interplay of Structural and Electronic Disorders in High-Temperature Superconductors using Scanning Tunneling Microscopy

A DISSERTATION PRESENTED
BY
ILIJA ZELJKOVIC
TO
THE DEPARTMENT OF PHYSICS

IN PARTIAL FULFILLMENT OF THE REQUIREMENTS
FOR THE DEGREE OF
DOCTOR OF PHILOSOPHY
IN THE SUBJECT OF
PHYSICS

HARVARD UNIVERSITY
CAMBRIDGE, MASSACHUSETTS

MAY 2013

Thesis advisor: Jennifer E. Hoffman Ilija Zeljkovic

Visualizing the Interplay of Structural and Electronic Disorders in High-Temperature Superconductors using Scanning Tunneling Microscopy

Abstract

The discovery of high-T_c superconductivity in 1986 generated tremendous excitement. However, despite over 25 years of intense research efforts, many properties of these complex materials are still poorly understood. For example, the cuprate phase diagram is dominated by a mysterious "pseudogap" state, a depletion in the Fermi level density of states which persists above the superconducting critical temperature T_c. Furthermore, these materials are typically electronically inhomogeneous at the atomic scale, but to what extent the intrinsic chemical or structural disorder is responsible for electronic inhomogeneity, and whether the inhomogeneity is relevant to pseudogap or superconductivity, are unresolved questions. In this thesis, I will describe scanning tunneling microscopy experiments which probe the interplay of structural, chemical and electronic disorder in high-T_c superconductors.

First, I will present the imaging of a picoscale orthorhombic structural distortion in Bi-based cuprates. Based on insensitivity of this structural distortion to temperature, magnetic field, and doping level we conclude that it is an omnipresent background not related to the pseudogap state. I will also present the discovery of three types of oxygen disorder in the high-T_c superconductor $Bi_2Sr_2CaCu_2O_{8+x}$: two different interstitials as well as vacancies at the apical oxygen site. We find a strong correlation between the positions of these defects and the nanoscale inhomogeneity in the pseudogap phase, which highlights the importance of chemical disorder in these compounds. Furthermore, I will show the determination of the exact intra-unit-cell positions of these dopants and the effect of different types of intrinsic strain on their placement. I will also describe the identification of chemical disorder in another cuprate $Y_{1-x}Ca_xBa_2Cu_3O_{7-x}$, and the first observation of electronic inhomogeneity of the spectral gap in this

material. Finally, I will present definitive identification of the cleavage surfaces in $Pr_xCa_{1-x}Fe_2As_2$, and imaging of Pr dopants which exhibit lack of clustering, thus ruling out Pr inhomogeneity as the likely source of the high-T_c volume fraction. To achieve the aforementioned results, we employ novel analytical and experimental tools such as an average supercell algorithm, high-bias dI/dV dopant mapping, and local barrier height mapping.

Contents

Listing of figures

Dedicated to my wife Courtney, for her unconditional love and support.

Acknowledgments

I am forever indebted to my family for their unconditional support. To my wife Courtney for being my best friend and partner in crime who helped me make it to the end when, at times, it seemed impossible. To my parents, for their unwavering love and support throughout the years and for making sacrifices to help me achieve my dreams. To my brother, Mihajlo for helping me see the lighter side in life and not take myself too seriously.

I would also like to thank my labmates and friends who helped, both professionally and personally, on numerous occasions. To Liz Main, for being an amazing mentor who generously invested much of her time and energy into training me. To Dennis Huang, for being the best mentee I could have hoped for, who made the final stretch of my Ph.D. so much more manageable. To Can-Li Song, for his positive attitude and enthusiasm for science. To Nick Litombe who was always a phone call away ready to help, working on achieving greater things from BNL. To Anjan Somyanarayanan, for his insight over the years, and for making the long days and weekends feel a little shorter. To Michael Yee, for all the good times we had, both in the lab and in the sun, and more good times to come. To Yang He, for his passion for physics and many exciting exchanges of scientific ideas. To Magdalena Huefner, for her willingness to listen when I needed to vent and for our many conversations about life and physics. To Jeehoon Kim, Yi Yin, and Martin Zech for invaluable advice and guidance when first starting up in the lab. To Alex Frenzel, Cun Ye, Sarah Schlotter and Harry Mickalide for shared laughs and making the lab a more pleasant place.

I would like to thank my friends outside of the world of science, John Kim and Leanna Work for sticking with me from day one and helping me feel at home in Boston. To my tennis partners and friends throughout the years Erin Fleming, Tarek Austin, Greg Leya, Jake Dockterman, Anthony Carpenter, Matthew Anstey, and Ronald Kamdem who kept me sane and were always ready to hit when I was stressed, or just sit down and talk on the side of the court about nearly anything.

Finally, I would like thank my thesis committee, Prof. Subir Sachdev and Prof. Markus Greiner for valuable feedback and interesting ideas about future scientific projects. To Prof. Eric Hudson, for his immense contributions to nearly every project I was involved with, invaluable advice and patience no matter how busy he was. Most of all, I'd like to thank my thesis advisor, Prof. Jenny Hoffman for her wisdom, guidance and generous financial support over the past five and a half years. The opportunities and equipment she provided and the environment she created helped me excel and achieve the lofty goals I set for myself when I first started graduate school. I have been lucky enough to learn from her about all aspects of a scientific project, from acquiring data to completing a manuscript, and none of my academic success would be possible without her guidance.

Thank you all again so much. I could not have done this without you.

1 Introduction

1.1 Conventional Superconductors

Conventional superconductors exhibit two defining properties: (I) vanishing of electrical resistivity below a critical temperature T_c, and (II) expulsion of magnetic flux below a critical field H_c. The former was discovered by Kamerlingh-Onnes in 1911 [1], and the latter by Meissner and Oschsenfeld in 1933 [2]. Almost 50 years after the initial discovery, Bardeen, Cooper and Schrieffer proposed a theory explaining the mechanism of superconductivity (BCS theory) [3]. According to BCS theory, a small attractive force between electrons, arising from their retarded interaction with the lattice (electron-phonon coupling), can pair the otherwise repulsive electrons, opening up a spectral gap in the electronic density of states (DOS) corresponding to the pairing energy. These "Cooper pairs" form an aggregate ground state which facilitates movement of charge through the crystal without loss of energy from scattering.

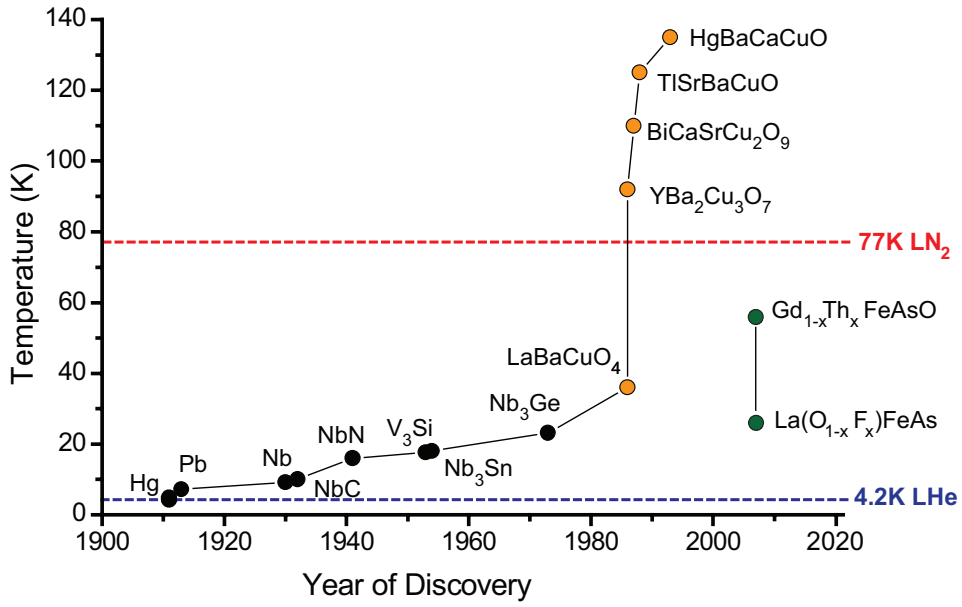

Figure 1.2.1: Timeline of the discovery of new superconductors. Orange circles represent Cu-based high-T_c superconductors, and green circles represent Fe-based high-T_c superconductors.

1.2 Cu-based High-T_c Superconductors

By the 1980s, superconductivity was considered theoretically solved but technologically marginal as the highest T_c was only 23 K for Nb_3Ge. Furthermore, McMillan had predicted the maximum T_c for phonon-induced Cooper pairing to be around 40 K [4], which is still inconveniently low for widespread commercial application. Then in 1986 came the discovery of an oxide superconductor with T_c of 30 K (nominal composition $Ba_xLa_{5-x}Cu_5O_{5(3-y)}$) [5], whose properties could not be explained by the BCS theory. Within one year, T_c in this new class of superconductors had already broken the liquid nitrogen barrier with the discovery of $YBa_2Cu_3O_{7-x}$ (YBCO) with T_c of 93 K [6] (Fig. 1.2.1). Since the common property of all these materials was the layered crystal structure that contained one or more CuO_2 planes, they were called "cuprates."

In contrast to the conventional superconductivity of elements, simple alloys, and stoichiometric compounds, high-T_c superconductivity in cuprates typically arises by off-stoichiometric doping of an

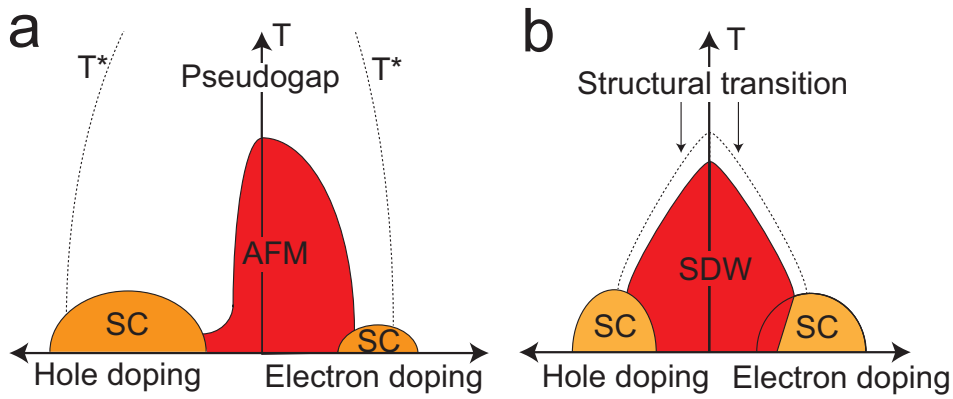

Figure 1.2.2: Phase diagrams for (a) Cu-based and (b) Fe-based high-T_c superconductors. The horizontal axis in both cases represents charge carrier doping.

antiferromagnetic parent compound. The parent compound is a Mott insulator due to the Coulomb repulsion that prevents double occupancy of Cu lattice sites. Upon the introduction of extra charge carriers into the system (hole or electron doping), the charges begin to hop between sites, and the electronic properties of these materials change dramatically [7]. As antiferromagnetism is weakened by doping, the material becomes superconducting, with T_c rising to a maximum and falling again, while the decreasing spectral gap indicates weakening pairing in the "overdoped" regime. Another prominent feature in the cuprate phase diagram is the mysterious "pseudogap" (PG) state characterized by the opening of a gap in the electronic DOS even above T_c, predominantly on the underdoped side (Fig. 1.2.2a). After more than 25 years of cuprate research, neither superconductivity nor the PG are well understood, and it is still debated whether the PG is a manifestation of a competing/coexisting order of charge- or spin-density wave (CDW)[8], or a Cooper-paired precursor to the superconducting state [9].

1.2.1 Crystal Structure

Crystal structures of some of the prominent members of the cuprates family are shown in Fig. 1.2.3. The experiments described in Chapters 3-5 have been performed on Bi-based cuprates (Bi-2212 shown in Fig. 1.2.3a), and the measurements presented in Chapter 6 have been acquired on Ca-doped YBCO (Fig. 1.2.3b).

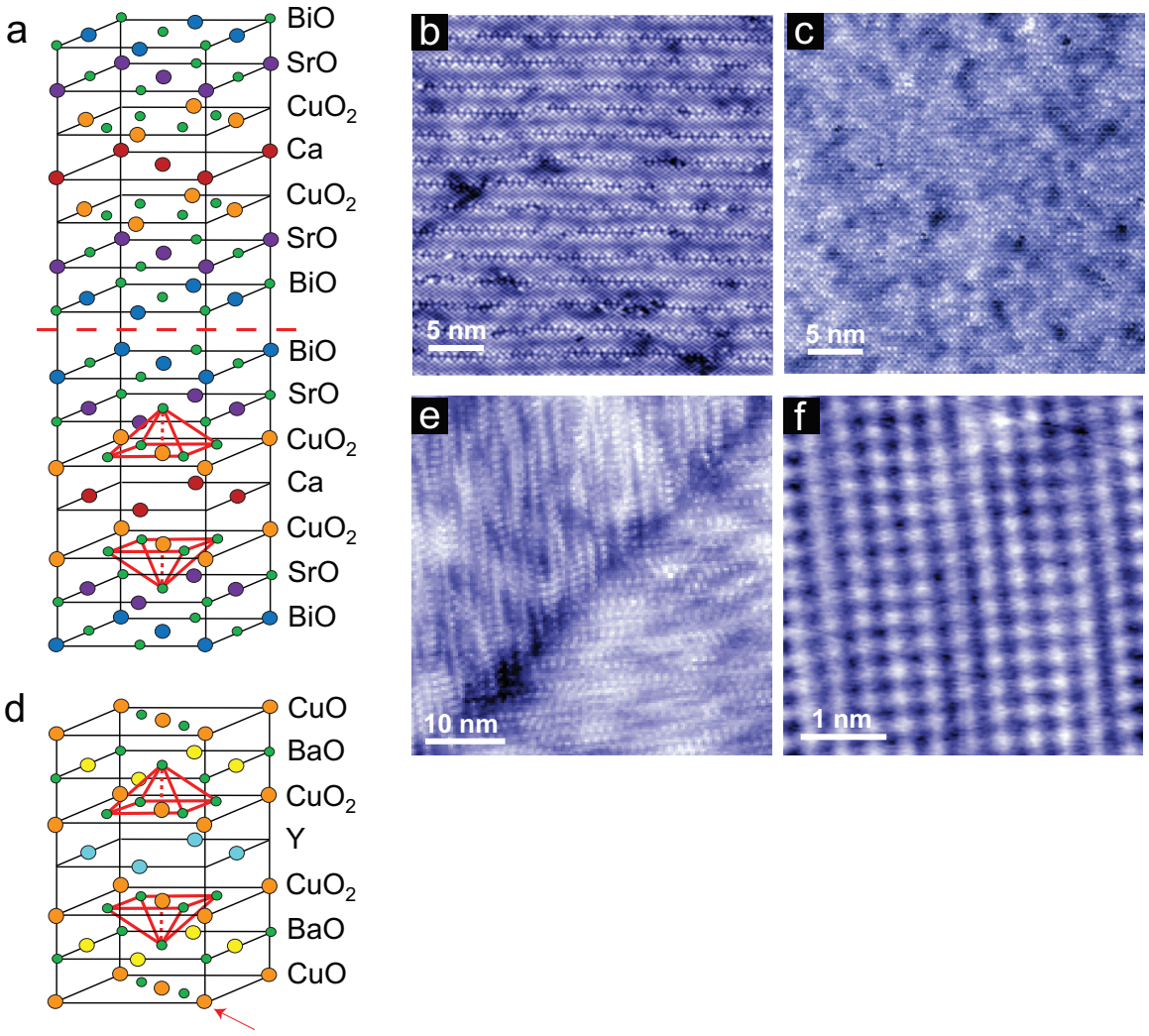

Figure 1.2.3: (a) Unit cell of Bi-2212. The crystal cleaves between two BiO layers. STM topographs of the BiO layer in (b) Bi-2212 and (c) Pb-doped Bi-2201. (d) Unit cell of YBCO. The crystal does not have a natural cleavage plane, and typically reveals either (e) CuO chain plane, or (f) BaO plane in STM topographs.

The family tree of Bi-based cuprates, discovered in 1988 [10, 11], boosted T_c up to ∼110 K, and constituted the first generation of commercially produced high-T_c cables [12]. Since adjacent BiO layers are weakly bonded by the van der Waals force, Bi-based cuprates typically cleave on a charge neutral plane between the two BiO layers (see dashed line in Fig. 1.2.3a for Bi-2212)), and has thus been the main target among cuprates for STM studies. STM experiments reveal a clear Bi lattice in topographs, as well as bright and dark "patches" arising from dI/dV spectral inhomogeneity (Fig. 1.2.3b). An additional complication in many Bi-based cuprates is the structural "supermodulation" (SM), a ∼ 25 Å incommensurate sinusoidal modulation that pervades the bulk of the material. It is seen in STM topographs with additional "$" quasiperiodic distortions at the modulation crests (Fig. 1.2.3b). Pb dopants substituted at the Bi sites can be used to partially or completely suppress this superstructure [13] as seen for Pb-doped Bi-2201 in Fig. 1.2.3c. Bi-based cuprates are non-stoichiometric, with several types of interstitial atoms, lattice site vacancies, and isovalent or aliovalent substitutions introduced into these compounds to achieve superconductivity.

In contrast to Bi-based cuprates, YBCO lacks a natural cleavage plane (Fig. 1.2.3d), but cryogenically-cleaved surfaces usually reveal either the BaO plane [14–17] (Fig. 1.2.3e) or CuO chain plane [14, 16–20] (Fig. 1.2.3f). Although these surfaces may be imaged with atomic resolution, neither show a superconducting gap.

1.3 Fe-based High-T_c Superconductors

The discovery of high-T_c superconductivity in Fe-based materials (Fe-SCs) in 2008 [21] provided a new opportunity for comparison with cuprates [22]. Similar to cuprates, Fe-SCs exhibit a dome-shaped superconducting phase diagram with a layered crystal structure and an antiferromagnetic parent compound (Fig. 1.2.2b). However, the parent state antiferromagnetism is itinerant, and of a different ordering wavevector than cuprates. Superconductivity can be induced or enhanced in Fe-based parent compounds by a wider variety of mechanisms [23, 24], including electron or hole doping, chemical or external pressure, and apparently even treatment with alcoholic beverages [25]. Almost five years since the initial discovery, the maximum T_c in bulk Fe-SCs remains capped at ∼ 57 K for $Sm_{0.95}La_{0.05}O_{0.85}F_{0.15}FeAs$ [26], while superconductivity up to 65 K has very recently been reported in single layer FeSe [27].

1.4 Dissertation Structure

High-T_c superconductors are typically electronically inhomogeneous at the atomic scale, but to what extent the intrinsic chemical or structural disorder is responsible for electronic inhomogeneity, and whether the inhomogeneity is relevant to superconductivity, are unresolved questions. In contrast to bulk-probe techniques that measure average properties over large areas of the sample, scanning tunneling microscopy (STM) is a real-space technique able to measure the electronic density of states with atomic resolution. In this thesis, I will talk about the experiments I have done on investigating the interplay of chemical disorder, strain, and electronic inhomogeneity in high-T_c superconductors.

In Chapter 2, I will give a brief theoretical background on scanning tunneling microscopy technique, and talk about different types of measurements possible.

In Chapter 3, I will discuss the first real-space detection of structural distortion and its relation to the PG state in Bi-based cuprates.

In Chapter 4, I will talk about the first direct imaging of all oxygen interstitial atoms, as well as oxygen vacancies in Bi-2212, and the correlation between their positions and the observed inhomogeneity in electronic DOS.

In Chapter 5, I will provide a detailed determination of interstitial oxygen dopant intra-unit-cell locations and their dependence on strain due to both SM buckling and orthorhombic distortion in Bi-2212.

In Chapter 6, I will describe the experiments on Ca-doped YBCO samples involving the observed inhomogeneity in spectral gap, as well as an unknown set of C_2-symmetric impurities.

In Chapter 7, I will show the utility of local barrier height mapping in determining the nature of different surface morphologies observed in an Fe-SC $Pr_xCa_{1-x}Fe_2As_2$.

2

Scanning Tunneling Microscopy

2.1 Basic Principles

Scanning tunneling microscopy (STM) was pioneered by Binnig and Rohrer in 1982 [28], a remarkable discovery subsequently awarded a Nobel Prize in Physics in 1986. The experimental technique is based on the principles of quantum tunneling of electrons between two electrodes separated by a potential barrier. The experimental setup consists of a sharp metallic tip which is brought within several Å of a conducting metallic surface using a 3-dimensional piezoelectric scanner (Fig. 2.1.1a). This scanner can position the tip both laterally (in the xy-plane) and vertically (in the z-direction) with sub-Å precision.

Application of voltage between the tip and the sample allows electrons to quantum-mechanically tunnel between the two (Fig. 2.1.1b). The resulting tunneling current can be calculated using the time-dependent perturbation theory. If a positive V is applied to the sample, the Fermi level of the sample shifts down with respect to the Fermi level of the tip, and electrons tunnel from the occupied states of the

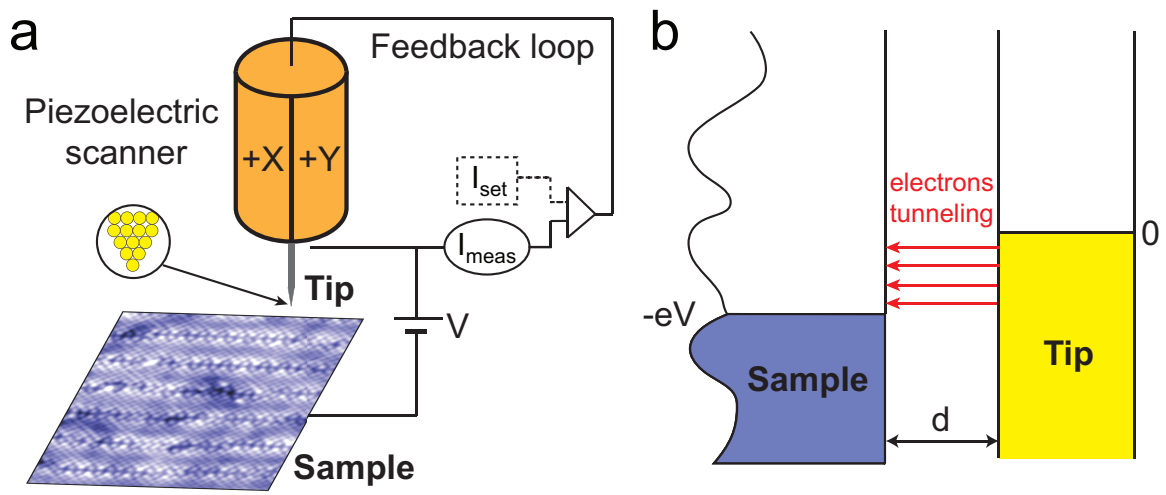

Figure 2.1.1: (a) Schematic representation of STM. A voltage V is applied between the tip and the sample. The tip is rastered across the surface in the xy plane and its z coordinate is adjusted using the three-dimensional piezoelectric scanner controlled by a feedback loop. (b) Quantum tunneling of electrons between the tip and the sample across a vacuum barrier of width d upon the application of a voltage bias V between the two. If a positive V is applied to the sample, the Fermi level of the sample shifts down with respect to the Fermi level of the tip, and electrons tunnel from the occupied states of the tip into the empty states of the sample.

tip into the empty states of the sample (Fig. 2.1.1b). The contribution to the current from tunneling of electrons from sample to tip, and from tip to sample at energy ε is:

$$i_{sample\to tip} = -2e\frac{2\pi}{\hbar}|M|^2(\rho_s(\varepsilon)\cdot f(\varepsilon))\cdot(\rho_t(\varepsilon - eV)\cdot[1 - f(\varepsilon - eV)]) \tag{2.1}$$

$$i_{tip\to sample} = -2e\frac{2\pi}{\hbar}|M|^2(\rho_t(\varepsilon - eV)\cdot f(\varepsilon - eV))\cdot(\rho_s(\varepsilon)\cdot[1 - f(\varepsilon)]) \tag{2.2}$$

where $|M|^2$ is the matrix element, $\rho_s(\varepsilon)$ and $\rho_t(\varepsilon)$ are density of states (DOS) of the sample and the tip respectively, and $f(\varepsilon)$ is the Fermi distribution given by:

$$f(\varepsilon) = \frac{1}{1 + e^{\frac{\varepsilon}{k_B T}}} \tag{2.3}$$

Summing the two contributions, and integrating over all energies gives:

$$I = -\frac{4\pi e}{\hbar}\int_{-\infty}^{\infty} |M|^2 \rho_s(\varepsilon)\rho_t(\varepsilon - eV)[f(\varepsilon)\cdot[1 - f(\varepsilon - eV)]] - f(\varepsilon - eV)\cdot[1 - f(\varepsilon)]d\varepsilon \tag{2.4}$$

Since thermal broadening $k_B T \sim 0.36meV$ at T$\sim$ 4K where most of the data presented in this thesis have been acquired, the above integral can be reduced to:

$$I \approx -\frac{4\pi e}{\hbar}\int_{0}^{eV} |M|^2 \rho_s(\varepsilon)\rho_t(\varepsilon - eV)d\varepsilon \tag{2.5}$$

In most conventional STM studies, tip consists of W or PtIr alloy which has a flat density of states around Fermi level (this is confirmed during the process of high-bias field-emission on a Au substrate by acquiring I *vs.* V curves that should be flat). In this scenario, $\rho_t(\varepsilon - eV) \approx \rho_t(0)$, and:

$$I \approx -\frac{4\pi e}{\hbar}\rho_t(0)\int_{0}^{eV} |M|^2 \rho_s(\varepsilon)d\varepsilon \tag{2.6}$$

Furthermore, the matrix element $|M|^2$ is nearly energy-independent [29], and can be taken out of the integral to obtain:

$$I \approx -\frac{4\pi e}{\hbar}\rho_t(0)|M|^2\int_{0}^{eV} \rho_s(\varepsilon)d\varepsilon \tag{2.7}$$

Using the assumption that the vacuum barrier between the tip and the sample is a simple square barrier, and applying WKB approximation, the matrix element $|M|^2$ can be written as:

$$|M|^2 \approx e^{-2\frac{s}{\hbar}\sqrt{2m\varphi}} \tag{2.8}$$

where m is the electron mass, s is the width of the vacuum barrier, and φ is the effective local barrier height (LBH), which represent some mixture of the tip and sample work functions [30].

By combining Eqns. 2.7 and 2.8, the expression for the tunneling current becomes:

$$I \approx -\frac{4\pi e}{\hbar}e^{-s\sqrt{\frac{8m\varphi}{\hbar^2}}}\rho_t(0)\int_{0}^{eV} \rho_s(\varepsilon)d\varepsilon \tag{2.9}$$

In summary, tunneling current measured in STM studies at bias V is proportional to the integral of the density of states from the Fermi level to eV.

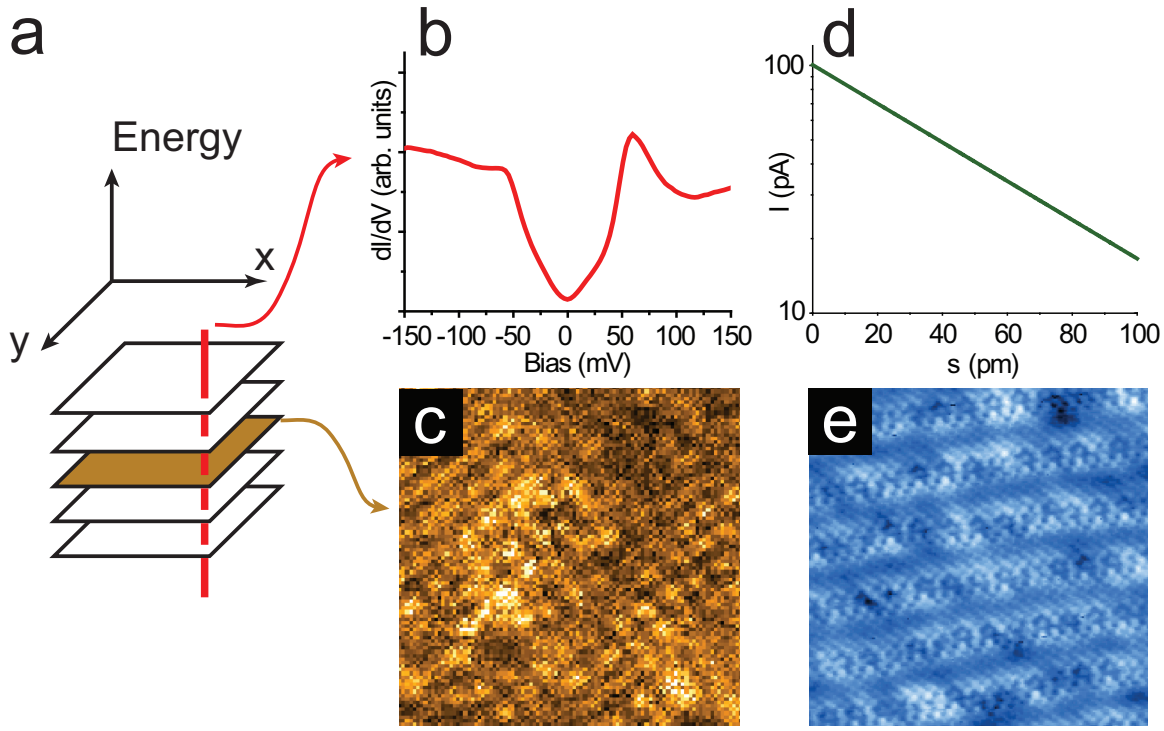

Figure 2.2.1: (a) Schematic of 3-dimensional data sets obtained on a pixel grid (DOS-maps). Each yellow sheet represents a single dI/dV map acquired at a different energy. Red line denotes a single dI/dV spectrum. (b) Single dI/dV spectrum obtained on Bi-2212. (c) An example of a dI/dV map obtained at $\sim$30 mV showing "checkerboard" charge order in Bi-2212. (d) Example of an $I-Z$ spectrum which can be used to extract LBH. (e) An example of a typical topographic measurement obtained on Bi-2212. Data shown in (b-e) have all been acquired using the STM shown in Fig. 2.3.1a.

2.2 Types of Measurements

2.2.1 Topograph

STM is most commonly used in the constant-current topographic mode. As the tip is rastered across the surface in the xy-plane at a fixed bias voltage V, the feedback loop adjusts the position of the tip in the z-direction to maintain the measured current I_{meas} at a fixed setpoint value I_{set} (Fig. 2.1.1a). The z trajectory of the tip effectively maps the surface contour.

However, as seen from Eqn. 2.9, tunneling current is dependent on tip sample separation as well as the integral of the density of states from Fermi level to eV. Therefore, for a sample with a homogenous DOS, this contour purely corresponds to the geometric surface corrugations. However, most materials exhibit a spatially heterogeneous DOS, which means that STM topographs of these compounds represent a combination of effects due to geometric corrugations and electronic density of states. Example of a topograph of Bi-2212 acquired with the STM built in the Hoffman lab (Fig. 2.3.1a) is shown in (Fig. 2.2.1e).

2.2.2 dI/dV SPECTRUM

In addition to acquiring information about the surface geometry, STM can obtain electronic DOS at energies of up to several electron volts, both in occupied and unoccupied sample states. The measurement is done by turning off the feedback loop (which fixes the tip-sample distance d), sweeping the bias voltage V, and measuring the current response $I(V)$. As seen from from Eqn. 2.9, I will be proportional to the integral of the density of states from Fermi level to eV. Taking a numerical derivative, it can be shown that:

$$\frac{dI}{dV} \propto \rho_s(eV) \tag{2.10}$$

From a practical stand point, taking a numerical derivative of I *vs.* V curve, to obtain the conductance dI/dV is extremely noisy. To circumvent this problem, dI/dV is usually measured using a lock-in amplifier technique, where a small bias voltage modulation dV (typically a few millivolts) is added to V, and the change in the tunneling current dI is measured to obtain dI/dV. An example of a typical dI/dV spectrum on Bi-2212 acquired using the home-built STM in Fig. 2.3.1a is shown in Fig. 2.2.1b.

2.2.3 dI/dV MAPPING

dI/dV spectra can be obtained on a densely-spaced pixel grid, which results in a 3-dimensional data set often referred to as a "DOS map" (Fig. 2.2.1a). Extracting a single "slice" (dI/dV map) at any desired energy essentially reveals spatial distribution of the density of states. An example of a dI/dV map can be seen in Fig. 2.2.1c, which shows "checkerboard" charge modulation in Bi-2212. In the experiments presented in this thesis, square grids of 200 to 400 pixel length have been used over $\sim$ 50 nm areas of the sample.

2.2.4 $I - Z$ SPECTRUM

From Eqn. 2.9, it can be calculated that:

$$\ln(I) \approx -s\sqrt{\frac{8m\varphi}{\hbar^2}} + \ln(\int_0^{eV} \rho_s(\varepsilon)d\varepsilon) \tag{2.11}$$

Therefore, by measuring the tunneling current I as a function of tip-sample separation s ("$I - Z$ spectrum"), we can obtain φ which is the effective local barrier height (LBH).

In practice, this process is done by stabilizing the tip in tunneling using the feedback loop (typically at 100 pA and 100 mV STM setup condition), and turning off the feedback loop. Then, by varying the voltage applied to the scantube, tip is moved away from the sample surface, and this distance s is recorded simultaneously with measuring the tunneling current I. As it can be seen from a typical $I - Z$ curve shown in Fig. 2.2.1d, $\ln(I)$ *vs.* s is linear, as expected from Eqn. 2.11. Furthermore, the slope a of this curve can be extracted to obtain the LBH:

$$\varphi = \frac{(\hbar a)^2}{8m} \tag{2.12}$$

2.3 HOME-BUILT STM SYSTEM IN THE HOFFMAN LAB

Scanning probes used in the Hoffman lab are all home-built. The particular STM system used to acquire most of the data presented in this thesis has been built by my colleagues, Elizabeth Main and Adam Pivonka, and myself (Fig. 2.3.1). The microscope itself is only ∼6 inches tall, and ∼2 inches in diameter, and the Z-walker range is ∼1 inch (Fig. 2.3.1a). Tip is pointing upwards and the sample is pointing downwards as shown in Fig. 2.3.1b. Both the tip and the sample can be changed *in situ* using a ∼6-foot long, vertical magnetic manipulator.

The system (Fig. 2.3.1c) is designed to be ultra-high vacuum (UHV) compatible, which in turn constrained the choice of the materials (e.g. no brass). There are several levels of vibration isolation present– both the room and the experiment table are floated on air springs to reduce any external vibrations coupling into the measurements. Although no magnetic field data will be presented in this thesis, the system is equipped with a 9 T vertical, and 3 T horizontal magnetic field.

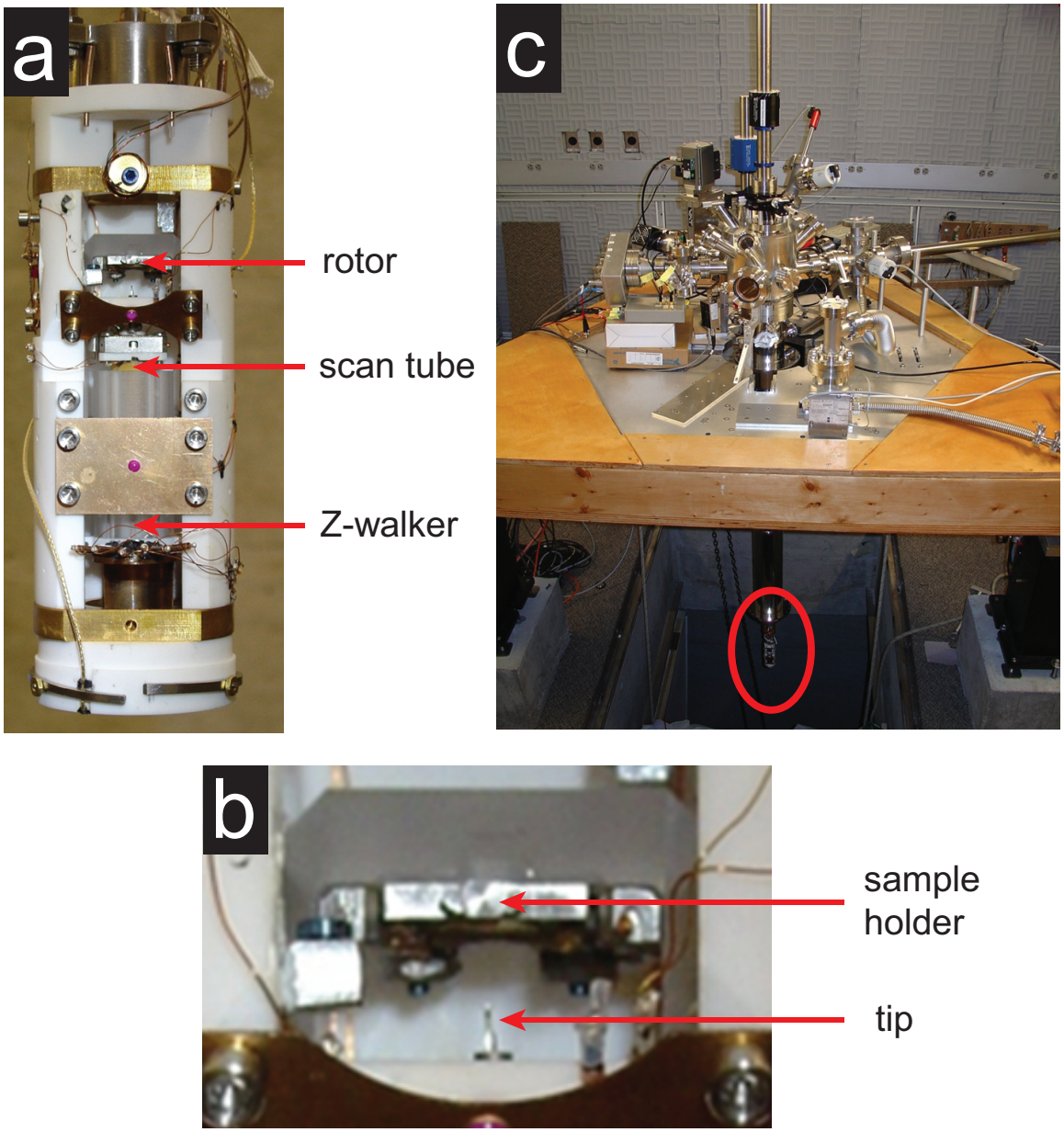

Figure 2.3.1: (a) STM (∼6 inches tall) built by Elizabeth Main. (b) Zoom-in on the sample holder and the tip. Prominent features in (a) and (b) are denoted by arrows. (c) The experimental setup built by Elizabeth Main, Adam Pivonka and Ilija Zeljkovic. The position of the microscope is denoted by red ellipse.

3

Real-space Detection of Orthorhombic Distortion in Bi-based Cuprates

3.1 Pseudogap as a Broken-symmetry State

Numerous symmetry-breaking electronic states have been theoretically proposed to explain the PG in the cuprate phase diagram (Fig. 1.2.2a). A two-dimensional CB charge order, may break translational but not rotational symmetry [31], while coexisting spin and charge density wave "stripes" [32] break both (though a precursor nematic state may break only rotational symmetry [33]). More exotic states, like the *d*-density wave, similarly break translational symmetry, but also time-reversal symmetry, while preserving their product [34]. Intra-unit-cell orbital current loops break time-reversal and inversion symmetry but also preserve their product [35]. The experimental realization of these symmetry breaking states, and their identification with the PG, remain highly debated.

Electronic states in Bi-based cuprates have been heavily investigated by a variety of techniques.

Angle-resolved photoemission spectroscopy (ARPES) has shown electronic states breaking time-reversal symmetry [36], as well as particle-hole and translational symmetry [37]. STM has shown evidence for electronic CB states breaking translational symmetry [38–42] and nematic states breaking rotational symmetry [43]. Furthermore, STM has found nanoscale variations in these symmetry breaking states [38–41, 44, 45]. Thus, to investigate the role of structure in these broken symmetry electronic states, it is imperative to make atomic scale measurements of the structural symmetry.

Since strong electronic distortions are typically accompanied by structural distortions, determining the relationship between these orders can be complicated. However, a clue comes from their (co-)dependence on other parameters. In cuprates, both superconductivity and the PG are highly dependent on doping, temperature, and magnetic field. In this chapter, I will show the first imaging of structural symmetry breaking due to orthorhombic distortion in Bi-based cuprates, and investigate whether this structural symmetry breaking is similarly dependent on these parameters, or whether it is an omnipresent background within which the electronic states evolve.

3.2 Detection of the Orthorhombic Distortion

Structural symmetries are traditionally measured by scattering experiments, such as X-ray or neutron scattering to determine bulk symmetries, or low energy electron diffraction (LEED) to determine surface symmetries. Although nearly tetragonal, a $\sim 0.5\%$ difference between a and b axes [11] makes the true structure orthorhombic. We apply the Lawler-Fujita drift-correction algorithm on all our data to correct for temperature drift (typically < 10 mK), piezo hysteresis, and piezo nonlinearity present during the process of data acquisition (see Appendix A.1). The global structural symmetry can be seen in the Fourier transforms of STM topographies (Figs. 3.2.1d-f). The dominant features are the tetragonal lattice vectors $\vec{Q}_x$ and $\vec{Q}_y$, and, in fields of view where the supermodulation has not been suppressed by Pb, the wavevector $\vec{Q}_{sm}$. However, in each case we also find one, and only one, of the orthorhombic wavevectors $\vec{Q}_a$ or $\vec{Q}_b$, shown schematically in Fig. 3.2.2a. The presence of an orthorhombic wavevector confirms the in-plane relative shift of the two Bi atoms already noted in the average supercells (see Fig. 3.2.2a). This shift reduces the symmetry of the crystal by removing mirror planes perpendicular to the b and c axes and replacing them with glide planes, thus changing the space group of the crystal from orthorhombic *Fmmm* to orthorhombic *Amaa*. Crystals in this space group still have three-dimensional inversion symmetry; for

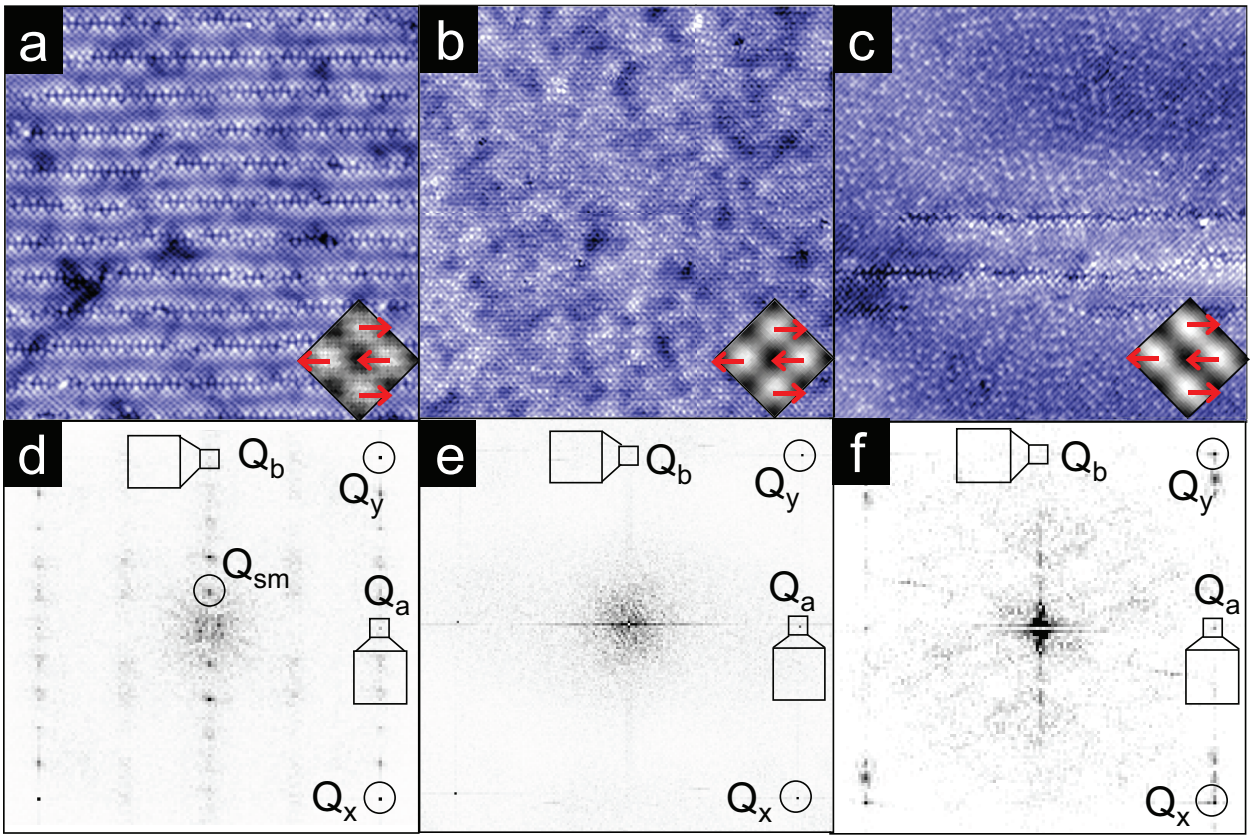

Figure 3.2.1: (a-c) Topographic images of 30 nm square regions of the BiO lattice from: optimally doped Bi-2212 with supermodulation, optimal $T_c = 35$ K Bi-2201 with Pb doping completely suppressing the supermodulation, and overdoped $T_c \sim 0$ K Bi-2201, also doped with Pb but with remnants of the supermodulation respectively. Each was cropped from larger (up to 80 nm) fields of view, for ease of viewing. Insets show the average supercell with arrows denoting the shifts of the Bi atoms. (d-f) Fourier transforms of (a-c), showing peaks at the tetragonal Bragg vectors $\vec{Q}_x$ and $\vec{Q}_y$ as well as at the orthorhombic $\vec{Q}_a = (\vec{Q}_x + \vec{Q}_y)/2$ (but not at the equivalent $\vec{Q}_b$). In (d) the supermodulation creates an additional incommensurate peak at $\vec{Q}_{sm}$.

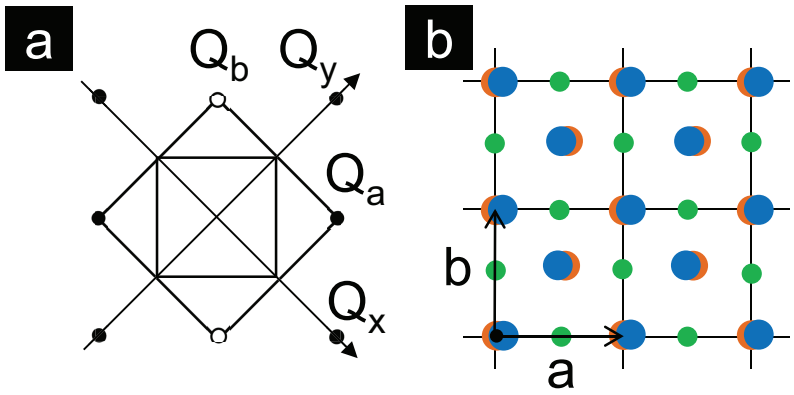

Figure 3.2.2: (a) In momentum space, atomic Bragg vectors (black circles) at $\vec{Q}_x = (2\pi/a_o, 0)$, $\vec{Q}_y = (0, 2\pi/a_o)$, define the tetragonal Brillouin zone (black square). Orthorhombic vectors (circles) $\vec{Q}_a = (\pi/a_o, \pi/a_o)$, $\vec{Q}_b = (-\pi/a_o, \pi/a_o)$ define the orthorhombic Brillouin zone (dashed square). (The average Bi-Bi nearest neighbor distance is $a_o = 0.383$ nm.) The orthorhombic distortion appears as a density wave along the a-axis, with alternate Bi rows moving closer/farther apart, leading to strength at $\vec{Q}_a$ in the FTs. $\vec{Q}_b$ (open circle) is notably absent. (b) In real space, the distortion in the surface layer of Bi (blue) and O (green) atoms appears as shifts of two Bi sub-lattices in opposite directions along the orthorhombic a-axis. This distortion breaks inversion symmetry at the Cu site, but preserves a single mirror plane along the a-axis. The undistorted Cu lattice (orange), two layers beneath the Bi atoms, is shown for reference (but does not appear in topographic images). The displacement d, of one Bi atom from its undistorted position, is marked here and reported on the left axis of Figs. 3.4.1b-d as a fraction of the orthorhombic lattice constant a_o, and on the right axis of Figs. 3.4.1b-d in picometers.

instance in Bi-2212, the inversion center lies in the calcium layer. However, distortion removes the two-fold rotation symmetry along the c axis, effectively breaking two-dimensional inversion symmetry in the BiO plane.

The presence of only one of Q_a or Q_b indicates that, in Figs. 3.2.1a-c, the Bi shift is along the same orthorhombic lattice axis throughout the field of view. This Bi shift is consistent with a distortion observed in supermodulated and un-supermodulated Bi-2201 and Bi-2212, by multiple bulk techniques [11, 46]. STM now becomes the first technique to measure this distortion locally.

3.3 Quantifying the local magnitude

3.3.1 Real-space method

Starting with a drift-corrected topograph (schematic shown in Fig. 3.3.1a), we create an average single-Bi unit cell with more pixels per atom than our raw data (typically 15 x 15 pixels per unit cell). For each pixel in the actual topograph, the location can be calculated with picoscale precision in relation to the nearest Bi atom. The data from that pixel is then placed in the appropriate bin in the average unit cell (Fig. 3.3.1b). This process builds up a histogram of weight at each sub-unit-cell-resolved position in the average unit cell, ultimately showing a high-resolution map of an average Bi atom (Fig. 3.3.1c). An analogous process can be used to create an average supercell of any size.

The creation of an average supercell allows an improvement of intra-unit-cell spatial resolution, at the expense of inter-unit-cell variation. This method allows us to detect variations in atomic positions as small as a few thousandths of a unit cell. For example, from a 2 x 2 supercell, we fit a peak to each of the four "atoms" in order to calculate their exact positions, and find orthorhombic distortion shifts as small as 0.5% of a unit cell. The 2 x 2 supercells for several different Bi-based cuprates are shown as insets in Fig. 3.2.1a-c.

We compare our technique to the original supercell averaging technique used by Lee *et al.* [47]. Lee's starting point for aligning the different unit cells to be averaged was a real-space Gaussian fit to each atomic peak in the topograph. Their fitting procedure allowed location of the atom with 20 picometer accuracy, but proved sufficiently time consuming that only 28 unit cells were ultimately averaged. Our algorithm which combines Lawler's drift correction and supercell averaging can locate individual atoms in un-supermodulated BSCCO with typical $\sim$8 picometer absolute accuracy and $\sim$2 picometer relative accuracy within a single field of view [48]. Furthermore, the centers of these atoms can be automatically located, and the resultant average supercell computed, for $>$10,000 unit cells in just a few seconds of run time.

3.3.2 Fourier-space method

We derive here the relationship between the two observed quantities: the value of the complex Fourier component at Q_a (shown in Fig. 3.2.2a), and the displacement d (shown in red in Fig. 3.2.2b) directly measured in the average supercell.

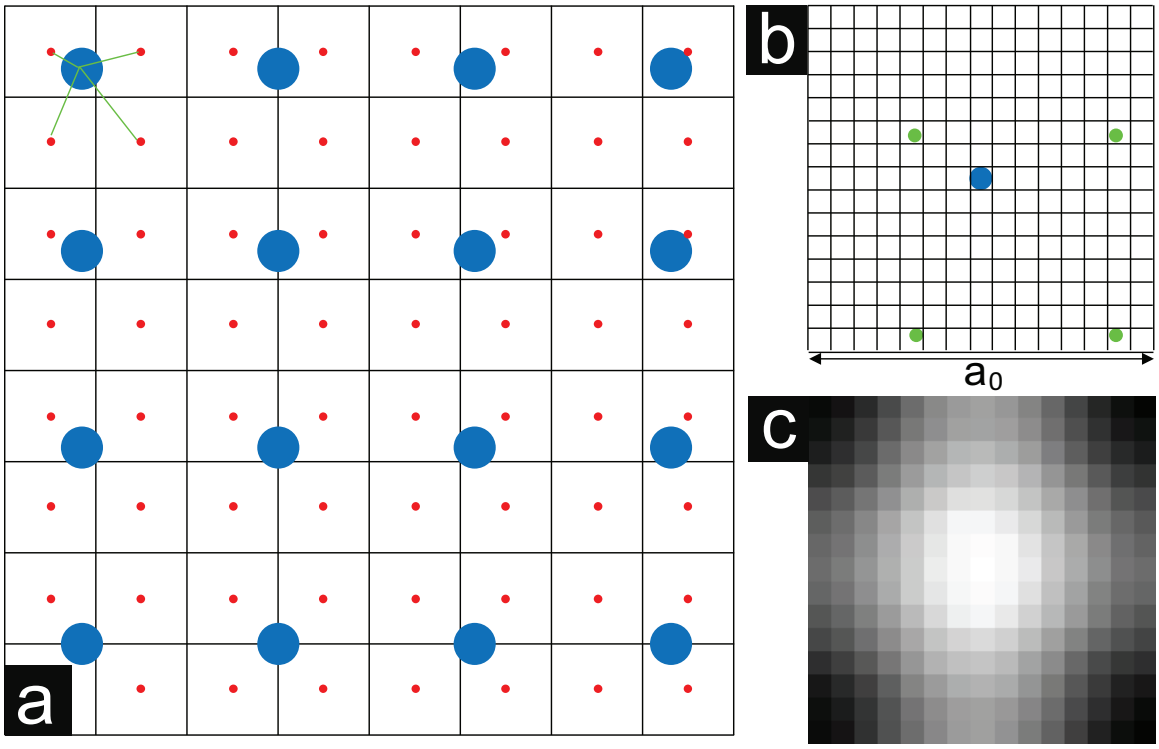

Figure 3.3.1: (a) Schematic of a drift-corrected topographic image with Bi atoms represented as blue circles. The data is acquired in a pixel grid outlined in black; the center of each pixel is marked with a red dot. The resolution of this image is only slightly better than the Nyquist frequency for atoms. (b) Schematic of the average 1 x 1 unit cell we will create with 15 x 15 pixels. We calculate the exact distance of every pixel in (a) to the nearest Bi atom (4 example distances are shown in green in (a)), then place it in the average unit cell in (b) to create a weighted histogram at each sub-unit-cell pixel. (c) Example of the final average unit cell obtained from a real topographic image.

We start by representing the topographic signal $T(\vec{r})$ and its spatial derivative $\nabla_{\vec{r}}(T(\vec{r}))$ in terms of the Bragg peak wavevectors $\vec{Q}_x$ and $\vec{Q}_y$, the wavevector of the orthorhombic distortion $\vec{Q}_a$, and the complex Fourier component A at wavevector $\vec{Q}_a$. (We normalize the expression so that a Cu atom sits at the origin, and the strength of the signal at wavevectors $\vec{Q}_x$ and $\vec{Q}_y$ is equal to 1.)

$$T(\vec{r}) = e^{\imath\vec{Q}_x\vec{r}} + e^{-\imath\vec{Q}_x\vec{r}} + e^{\imath\vec{Q}_y\vec{r}} + e^{-\imath\vec{Q}_y\vec{r}} + Ae^{\imath\vec{Q}_a\vec{r}} + A^*e^{-\imath\vec{Q}_a\vec{r}} \tag{3.1}$$

$$\begin{aligned}\nabla(T(\vec{r})) = \imath\vec{Q}_x e^{\imath\vec{Q}_x\vec{r}} - \imath\vec{Q}_x e^{-\imath\vec{Q}_x\vec{r}} + \imath\vec{Q}_y e^{\imath\vec{Q}_y\vec{r}} - \imath\vec{Q}_y e^{-\imath\vec{Q}_y\vec{r}} + \\ A\imath\vec{Q}_a e^{\imath\vec{Q}_a\vec{r}} - A^*\imath\vec{Q}_a e^{-\imath\vec{Q}_a\vec{r}}\end{aligned} \tag{3.2}$$

Our objective is to find the value of $\vec{r}$ at which $T(\vec{r})$ reaches its maximum. This is the position in space to which the distorted Bi atom moves, with respect to an undistorted (0,0) position. Setting the gradient of $T(\vec{r})$ to 0, and using the fact that $\vec{Q}_a = (\vec{Q}_x + \vec{Q}_y)/2$, we find that:

$$\begin{aligned}\vec{Q}_x(e^{\imath\vec{Q}_x\vec{r}} - e^{-\imath\vec{Q}_x\vec{r}} + \frac{A}{2}e^{\imath\vec{Q}_a\vec{r}} - \frac{A^*}{2}e^{-\imath\vec{Q}_a\vec{r}}) + \\ \vec{Q}_y(e^{\imath\vec{Q}_y\vec{r}} - e^{-\imath\vec{Q}_y\vec{r}} + \frac{A}{2}e^{\imath\vec{Q}_a\vec{r}} - \frac{A^*}{2}e^{-\imath\vec{Q}_a\vec{r}}) = 0\end{aligned} \tag{3.3}$$

Since $\vec{Q}_x$ and $\vec{Q}_y$ are orthogonal, both parenthetic expressions must vanish. Because the parenthetic expressions are equal, we see that $\vec{Q}_x \cdot r = \vec{Q}_y \cdot r$. Because $\vec{Q}_a = (\vec{Q}_x + \vec{Q}_y)/2$, we see that $\vec{Q}_a \cdot r = \vec{Q}_x \cdot r = \vec{Q}_y \cdot r$. In full generality, we express the complex distortion strength A in terms of its half amplitude and phase, $A = 2A_0e^{\imath\theta}$. Therefore,

$$\begin{aligned}&\sin(\vec{Q}_x \cdot \vec{r}) + A_0\sin(\vec{Q}_a \cdot \vec{r} + \theta) = 0 \\ &\sin(\vec{Q}_y \cdot \vec{r}) + A_0\sin(\vec{Q}_a \cdot \vec{r} + \theta) = 0 \\ &\Rightarrow \sin(\vec{Q}_a \cdot \vec{r}) + A_0\sin(\vec{Q}_a \cdot \vec{r} + \theta) = 0\end{aligned} \tag{3.4}$$

From this expression, we find the distortion d as a percent of the orthorhombic unit cell.

$$2\pi d = \vec{Q}_a \cdot \vec{r} = \frac{1}{2\pi}\arctan\left(\frac{-A_0\sin(\theta)}{1 + A_0\cos(\theta)}\right) \tag{3.5}$$

One can simplify this expression considerably by noting that the orthorhombic distortion is odd about each Cu site. In other words, the ideal topography $T(\vec{r})$ could be expressed more simply as:

$$T(\vec{r}) = 2\cos(\vec{Q_x}\cdot\vec{r}) + 2\cos(\vec{Q_y}\cdot\vec{r}) + 4A_o\sin(\vec{Q_a}\cdot\vec{r}) \tag{3.6}$$

(using the same normalization as in Eqn. 3.1). Therefore, for the perfect lattice, $\theta = -\pi/2$. In this case we find simply that $2\pi d = \arctan(A_o)$.

However, imperfections in the application of the drift correction algorithm, at most $\sim 3\%$ of a unit cell [48], may introduce a small phase error, so that $\theta = -\pi/2 + \varepsilon$. We then find:

$$2\pi d = \arctan\left(\frac{A_o\cos(\varepsilon)}{1 + A_o\sin(\varepsilon)}\right) \tag{3.7}$$

Because all quantities (d, A_o, and ε) are small, we expand the argument as:

$$2\pi d \approx \arctan(A_o(1 - \frac{1}{2}\varepsilon^2)(1 - A_o\varepsilon)) \approx \arctan(A_o(1 - A_o\varepsilon - \frac{1}{2}\varepsilon^2)) \approx \arctan(A_o) \tag{3.8}$$

In conclusion, the complex value A of the Fourier transform at the Q_a point is expected to be purely imaginary. Small (up to 3% unit cell) errors from imperfect drift correction may introduce a small real component to A, but such errors contribute only a second order correction to the relation $2\pi d = \arctan(A_o)$.

3.4 Orthorhombic Distortion as a Function of Doping, Temperature and Magnetic Field

The question remains: what relationship, if any, does this structural distortion bear to the variety of predicted and observed electronic orders, particularly to highly-debated claims [35] that the PG is characterized by intra-unit-cell inversion symmetry breaking? To investigate this, we characterize the dependence of the structural distortion on parameters which are known to heavily influence electronic ordered states: doping, temperature, and magnetic field. Fig.3.4.1a locates in a three-dimensional phase diagram the 21 datasets in which we measured the structure. The key results are summarized in Figs. 3.4.1b-d. We do not find a dependence of the structural distortion on doping, temperature, or field,

across a wide range of values. We have measured the distortion both inside and outside the superconducting state, and in samples with vastly different PG energies, yet the structural distortion appears insensitive to these effects. We therefore conclude that the structural inversion symmetry breaking state is an omnipresent background against which the electronic states evolve, and not the long-sought PG state itself.

In order to further investigate the spectral effect of strain from the inversion symmetry breaking orthorhombic distortion, we compare the gap at the two inequivalent Bi sites in the orthorhombic unit cell. We find no evidence that the gap changes between these two sites. A representative example (chosen from our largest image) is shown in Fig. 3.4.2.

3.5 Imaging the Mirror Plane

In non Pb-doped Bi-2212, we find that the orthorhombic distortion lies along the *a*-axis (wavevector at $\vec{Q}_a$), orthogonal to the supermodulation in all 10 samples investigated. The probability that this is a coincidence is less than 0.1 %. In Pb-doped samples, however, the supermodulation is suppressed to the point where it no longer forces the orthorhombic distortion along the *a*-axis. Although without the supermodulation it is impossible for us to differentiate between the *a* and *b* axes, we did, as shown in Fig. 3.5.1, find one domain boundary, where the distortion rotates by 90°. This is rare – in all other images, up to 80 nm square, we find, as shown in Fig. 3.2.1, a single orthorhombic distortion vector. The probability of finding a domain boundary is on the order of $4L/D$, where L is the size of our image and D is the size of a domain; from 15 images of average size 50 nm, we estimate the size of a domain to be on the order of one micrometer.

To find domain boundaries we map the spatial dependence of the strength of the topographic signal A at the orthorhombic wavevectors. This is calculated by demodulating the signal (shifting the Fourier transform so the desired wavevector $\vec{q}$ is at zero frequency, low-pass filtering and then inverse transforming), giving us a spatially dependent Fourier amplitude $A(\vec{q}, \vec{r})$. One of $A(\vec{Q}_a, \vec{r})$ and $A(\vec{Q}_b, \vec{r})$ will be zero and the other non-zero, so that a map of the difference, $D(\vec{r}) = A(\vec{Q}_a, \vec{r}) - A(\vec{Q}_b, \vec{r})$, will have a roughly uniform magnitude and sign. The spatial distributions of these maps are reflected in the error bars of Fig. 3.4.1. In Fig. 3.5.1, however, the sign of $D(\vec{r})$ flips between the upper and lower half of the

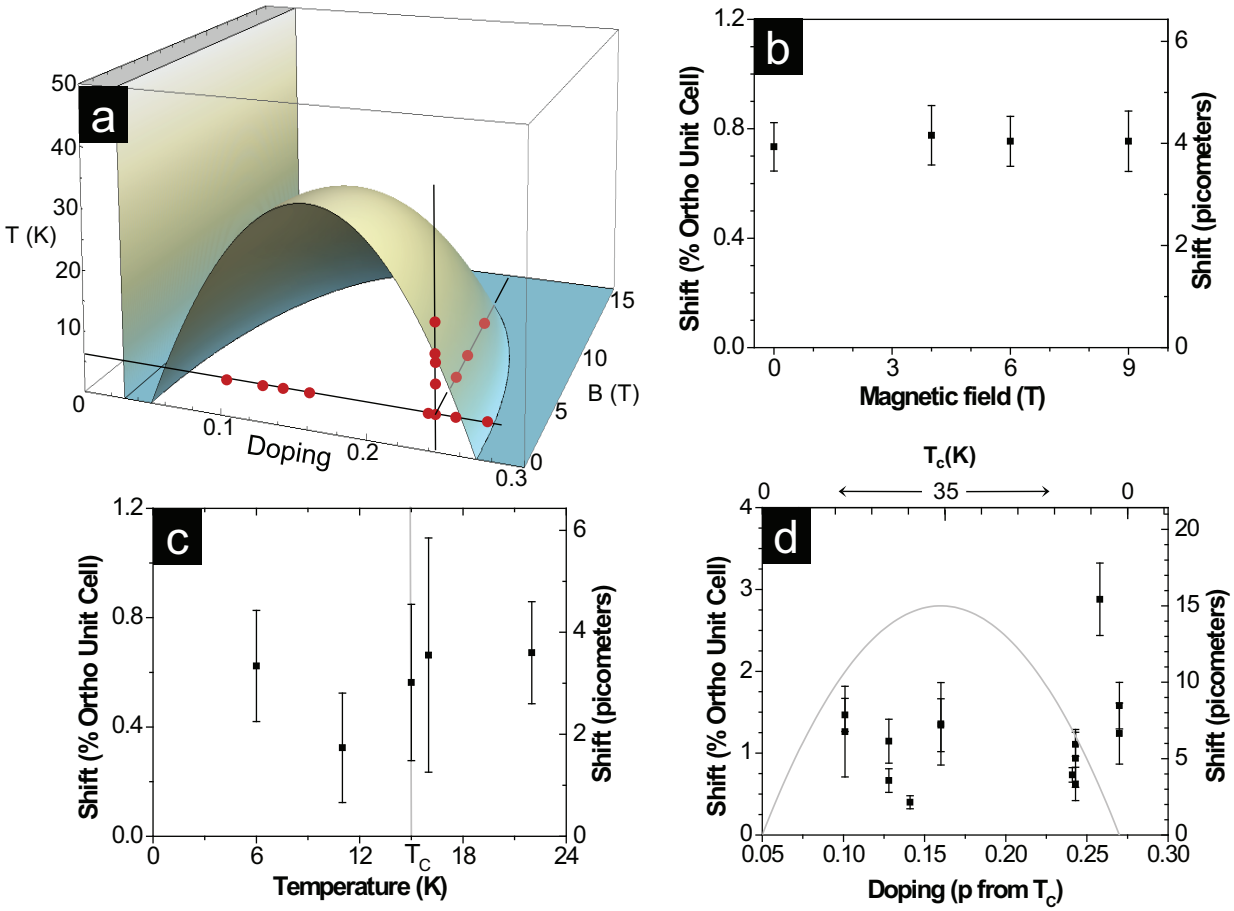

Figure 3.4.1: (a) Schematic phase diagram of Bi-2201, locating (red dots) the 15 experimental conditions under which the 21 datasets used in this figure were taken. (b-d) show orthorhombic distortion as a function of (b) magnetic field, (c) temperature, and (d) doping [49]. (b) and (c) each contain data from a single tip and region of overdoped Bi-2201 samples with $T_c = 16$ K and 15 K respectively. Additional scatter in (d) may reflect differences in tip quality or field of view across the 14 samples.

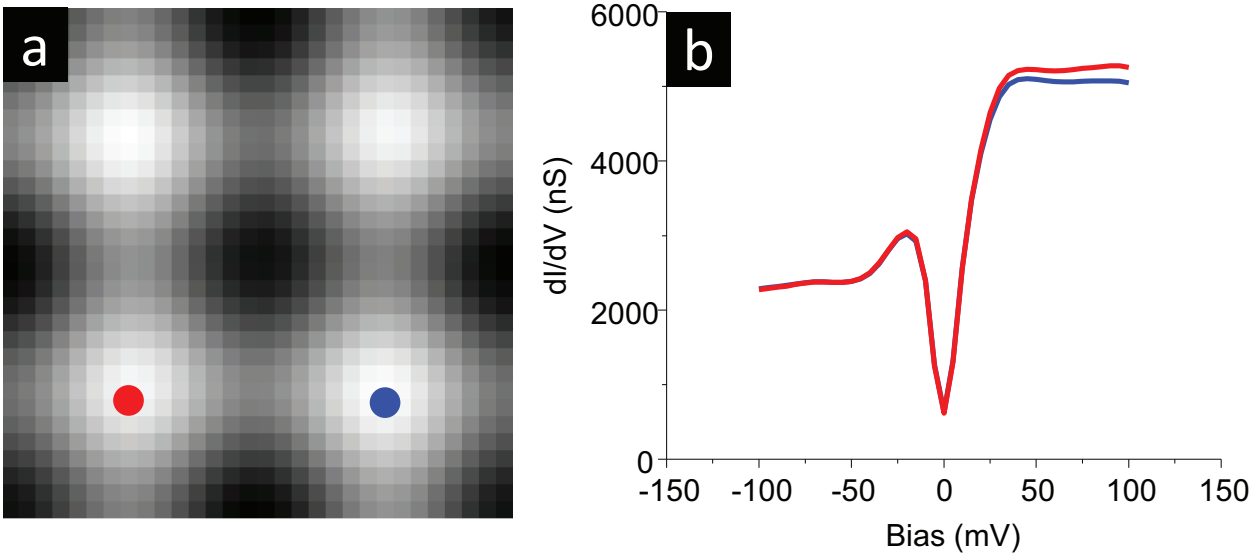

Figure 3.4.2: (a) 2 x 2 average supercell from T_c=35 K underdoped Bi-2201 with Pb dopants used to suppress the supermodulation. (b) Average spectra from the two inequivalent Bi sites show identical gap energy.

figures, highlighting the rotation of the distortion axis between these two regions. The difference is also clear in Fourier transforms from the two different regions (Figs. 3.5.1c-d).

3.6 Conclusion and Discussion

In conclusion, we have demonstrated the first local imaging of the orthorhombic distortion present across the phase diagram in Bi-based cuprates. Furthermore, we have devised a novel algorithm to extract the magnitude of this distortion from STM topographs, and have shown how to utilize two-dimensional Fourier-transforms to detect the local mirror plane. Based on lack of dependence of magnitude of the orthorhombic distortion on temperature, magnetic field and doping, coupled with insensitivity of dI/dV spectra to the position at the two inequivalent Bi sites, we conclude that the PG state is not sensitive to the strain of the orthorhombic distortion.

In claiming a broken electronic symmetry state, one should know whether the electronic order breaks or preserves the structural symmetry of the crystal. Bulk probes such as X-ray diffraction and neutron scattering cannot determine whether electronic and structural orders choose the same symmetries

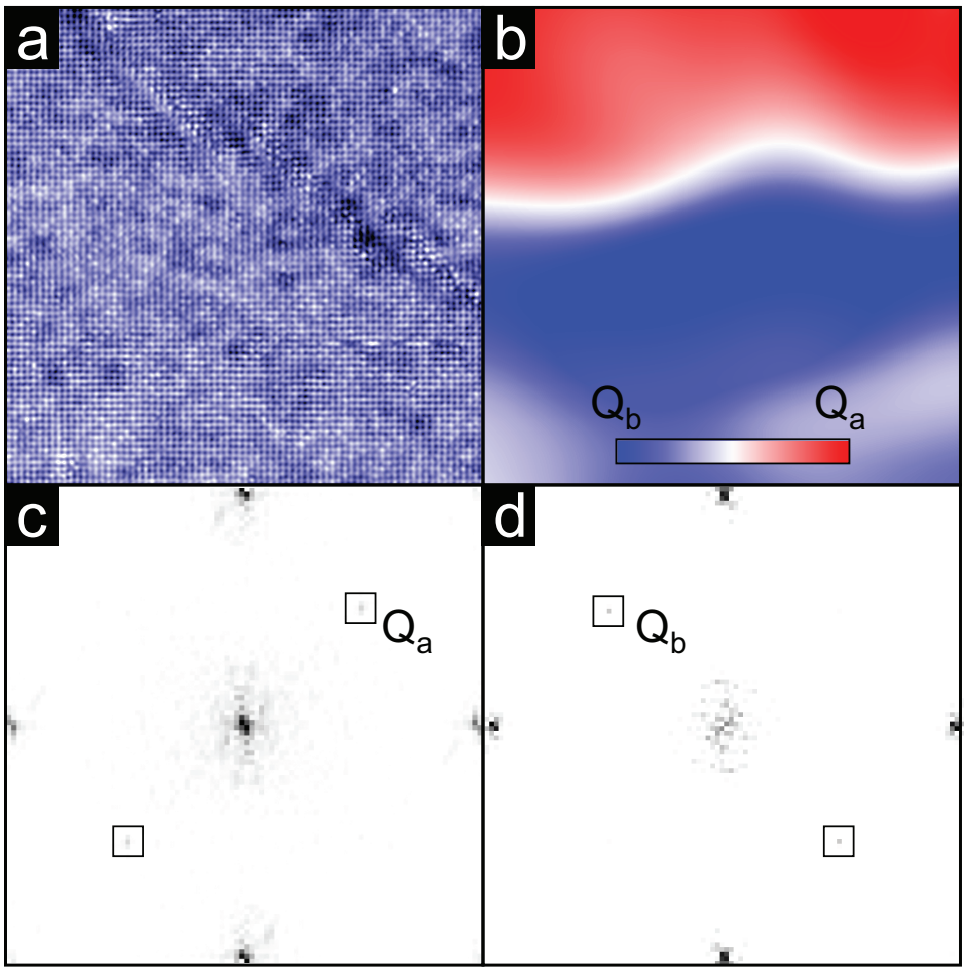

Figure 3.5.1: (a) Topographic image of $T_c = 25$ K underdoped Bi-2201. (b) The distortion map, $D(\vec{r}) = A(\vec{Q_a}, \vec{r}) - A(\vec{Q_b}, \vec{r})$, of the same field of view, where $A(\vec{q}, \vec{r})$ is the spatially dependent Fourier amplitude. A change in sign (color) indicates the rotation of the distortion axis and associated mirror plane across the domain boundary separating top and bottom of the figure. (c-d), Fourier transforms of the top and bottom of (a) respectively, highlight the rotation of the orthorhombic distortion vector from $\vec{Q_a}$ to $\vec{Q_b}$.

locally; in contrast, STM can investigate these symmetries on atomic length scales. For example, we suggest that future STM studies should search for modification of the local electronic symmetry across structural domain boundaries, such as that shown in Fig. 3.5.1. Furthermore, as the structural inversion symmetry breaking may lead to the appearance of electronic inversion symmetry breaking, we suggest that any reports identifying this inversion symmetry breaking with the PG phase should explicitly track the broken symmetry with temperature, magnetic field, and doping, as we have done, to ensure that it changes as would be expected with the changing PG energy scale. Finally, implementation of our average supercell algorithm, coupled with the ability of STM to measure structural and electronic symmetries locally, will become an important part of future STM studies, not only on cuprates, but on many important materials, such as the new iron-based superconductors, where the cleaved surface structure remains controversial [50]. Our real-space algorithm can even enable atom-specific high-resolution unit cell mapping not possible with Fourier techniques, in cases where two visibly different species are stochastically mixed at the sample surface, such as Se and Te site in $FeTe_{1-x}Se_x$ which can be sorted automatically based on their bimodal distribution of topographic height [51].

4

Oxygen Dopant Disorder and Pseudogap in Bi-2212

4.1 Nanoscale Electronic Inhomogeneity in Bi-2212

STM studies of Bi-2212 have revealed several types of spatial nanoscale inhomogeneity in the electronic density of states.

- **Spectral gap magnitude.** The Fermi level gap in the density of states is found to vary by $\sim 100\%$ in width, on a 2-3 nm length scale, across a wide range of doping [41, 52]. Because of the similar energy scales near optimal doping [8], there has been persistent confusion between the identification of the superconducting gap and the pseudogap (PG) – a mysterious depression in the near-ε_F density of states which surprisingly persists far above the superconducting T_c on the underdoped side of the phase diagram 1.2.2a. Many early STM studies discuss superconducting gap inhomogeneity, but more recent normalization [53] and fitting [54] techniques reinforce that the PG represents a distinct energy scale and phase [55], and suggest that the observed spectral gap inhomogeneity is due primarily to variations in the PG. This is significant, because it is believed

that the PG phase competes with superconductivity [54, 56], so the nanoscale variations in PG suggest the possibility to control and mitigate its competition, if only the hidden variable determining its local strength can be found.

- **Checkerboard charge order.** A second type of inhomogeneity is a disordered periodic modulation of the spectral weight which is static but most noticeable at energies within and near the PG energy. The wavevector of this modulation tracks the antinodal nesting wavevector across a wide range of doping in single [44] and double [57] layer BSCCO. This modulation has been termed "checkerboard" [38], "fluctuating stripes" [39, 45], "electronic glass" [57], or "charge density wave" (CDW) [42]; for simplicity we will use the latter terminology. Field [38], doping [41], and temperature [45] dependence suggest that this static spatial modulation is in fact the electronic ordered phase associated with the PG.

- **Quasiparticle interference.** A third type of disordered periodic inhomogeneity arises from elastic scattering between degenerate states; this dispersing 'quasiparticle interference' (QPI) may exist at similar wavevectors to the static checkerboard modulation, but only at a limited range of energies within the superconducting gap [58].

Although several theoretical studies have predicted nanoscale electronic inhomogeneity [59, 60], the roles of spontaneous electronic phase separation [59] and chemical disorder [60] remain unresolved. Since a combination of off-stoichiometric doping by oxygen intercalation and/or cation substitution is necessary to achieve superconductivity in Bi-based cuprates, this chemical disorder has been the main candidate to cause the observed spatial inhomogeneity in the electronic DOS. In particular, the random distribution of interstitial oxygen dopants within the crystal seems like an obvious explanation behind the inhomogeneity in the spectral gap [60]. However, this hypothesis was difficult to test since typical, low-energy STM experiments were unable to locate these dopants, and more challenging experiments at higher energies were needed. In a pioneering study, McElroy *et al.* imaged a set of interstitial oxygen atoms in Bi-2212 as atomic-scale resonances in dI/dV images at -0.96 V bias **(type-B Oxygen atoms)** [61]. However, the correlation between the locations of the observed O dopants and the magnitude of the spectral gap was relatively weak and of unexpected sign: although it is well-established that the dominant spectral gap, now known to be the PG, decreases monotonically with increasing O dopant concentration [8], McElroys O dopants were more likely to be found in the areas of the high PG.

To resolve the issue, one carefully tuned theory suggested that the dominant local effect of interstitial oxygens may be strain, which increases the local pairing strength [62, 63]. A second proposal by Zhou *et al.* [64] postulated the existence of two types of interstitial oxygen dopants: type-B Os observed by McElroy, which live around the BiO plane and contribute only delocalized charge, and **type-A Oxygen atoms**, which reside around the SrO plane and have an immediate electrostatic effect, locally hole-doping the adjacent CuO_2 layer. Therefore, Zhou *et al.* predicted that the type-A oxygens would follow the expected global trend: a strong anticorrelation with the PG. However, the type-A oxygens were predicted to have resonances even farther below Fermi level than the –0.96 V type-B Os. This experimental challenge has prevented their observation to date. In this chapter, I will describe the first imaging of type-A Os, as well as surprising vacancies at the apical O site (**AOVs**), and their correlation with the observed electronic inhomogeneity in Bi-2212.

4.2 Imaging of Atomic-scale Defects

Fig. 4.2.1a shows a topograph of the BiO surface of Bi-2212 with T_c=55 K, demonstrating atomic resolution at +1 V bias. Fig. 4.2.1b shows $dI/dV(-1V)$ map acquired over the same area as Fig. 4.2.1a, containing atomic scale features of similar form and concentration to the previously observed type-B O dopants [61]. Fig. 4.2.1c extends the energy range down to show $dI/dV(-1.5V)$ map, resolving for the first time a second set of atomic scale features presumed to be the predicted type-A interstitial oxygen [64]. Fig. 4.2.1d extends the energy range above Fermi level to show $dI/dV(+1V)$ map, revealing a third set of atomic scale features. No other distinct atomic-scale features emerge in differential conductance images at biases between -2 V and +1.6 V.

Typical dI/dV spectra at each of the three types of dopants, and the background, are shown in Fig. 4.2.1e. The defining features used to identify the impurities, such as the peak around –1 V for a type-B oxygen, and the sudden changes of the slope around –1.2 V and +0.8 V for type-A and +1 V feature, respectively, are robust for different setup conditions, locations, and samples. In order to determine and verify the identity of +1 V features, which were previously unobserved and not theoretically predicted, we look at: (I) dependence of concentration with doping, and (II) lateral intra-unit-cell position.

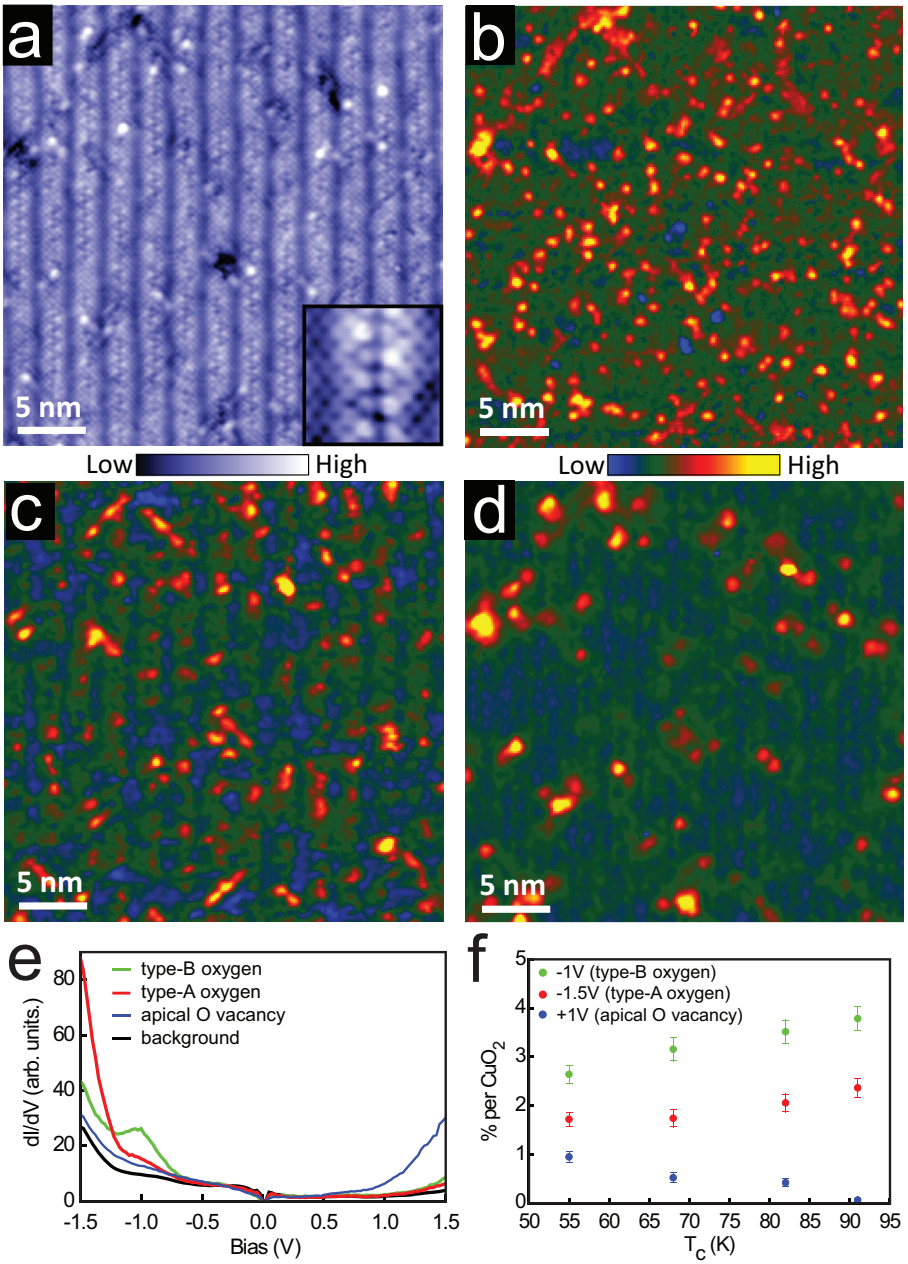

Figure 4.2.1: (a) Atomically resolved topographic image of Bi-2212 with $T_c = 55$ K, acquired at $V_{sample} = +1$ V and setpoint current $I = 150$ pA over a 35 nm area (inset, 3 times magnification). (b-d) dI/dV images in the same area as (a), acquired at $V_{sample} = -1$, -1.5, and $+1$ V, respectively. (e) dI/dV spectra over each dopant type, from the T_c=82 K sample. Each colored spectrum is the average of all imaged dopants of its type within a 30-nm field of view; the black trace shows the average spectrum far from dopants. Setup condition: 260 pA and -650 mV. (f) Density of each type of dopant imaged within four samples studied.

4.2.1 Oxygen defect concentration dependence on hole doping

We repeat the same high-bias measurement, and map the three types of dopants on four different samples, and show that the density of each type of dopant vs. T_c in Fig. 4.2.1f. As expected, we observe a monotonic decrease in the number of both types of interstitial oxygen dopants with falling T_c. However, the +1 V features increase from virtually zero for optimally doped Bi-2212, to almost 1% per CuO_2 plaquette for the T_c=55 K sample. This rules out cation substitutions, since annealing up to 840°C does not change the cation concentrations in Bi-2212 [65], and it can be concluded that these defects are a direct consequence of oxygen vacancies at lattice sites.

4.2.2 Intra-unit cell location of +1 V features

There are three distinct O lattice sites (all laterally offset from one another) where O vacancies could be created (Fig. 4.2.2a). To determine the exact positions of the atomic-scale features appearing in differential conductance maps at biases higher than +0.8 V, we first utilize the Lawler-Fujita drift-correction algorithm [43] on each dataset to locate each Bi atom with picoscale accuracy (Appendix A.1). When this algorithm is used with correction length scale Λ greater than the supermodulation wavelength $\Lambda_{SM} \sim 7a_o$, the effect is to remove the inevitable slow thermal and piezo drift which occur during a multi-hour map, without altering the true structure of the surface. However, for the purpose of locating the dopant features within the unit cell, we need a "perfect" square grid. We therefore choose a short correction length scale $\Lambda \sim a_o$ which removes both the slow drift which is an experimental artifact, and also most of the real lateral distortion of the supermodulation, as seen in Fig. 4.2.2b.

We next perform a Gaussian fit to find the center of each feature in the +1V dI/dV map, and determine its lateral location with respect to the nearest atoms in the corrected topograph. We directly compare the +1 V feature locations to each of the three distinct O lattice sites, illustrated in Fig. 4.2.2a. Fig. 4.2.2c-e shows the lateral position of each +1 V feature within the unit cell, for two samples. For each sample, the same set of +1 V features is replotted 3 times, with respect to each layer, to emphasize its relation to the 3 inequivalent oxygen lattice sites. Due to the large size of the dopant (full width at half max ~0.75 nm, compared to the 0.383 nm unit cell size), and due to the difficulty in removing 100% of the supermodulation distortion, there remains some scatter in the lateral locations, but we are still able to distinguish clearly between the three possible O sites. We find that the +1 V features are consistent only

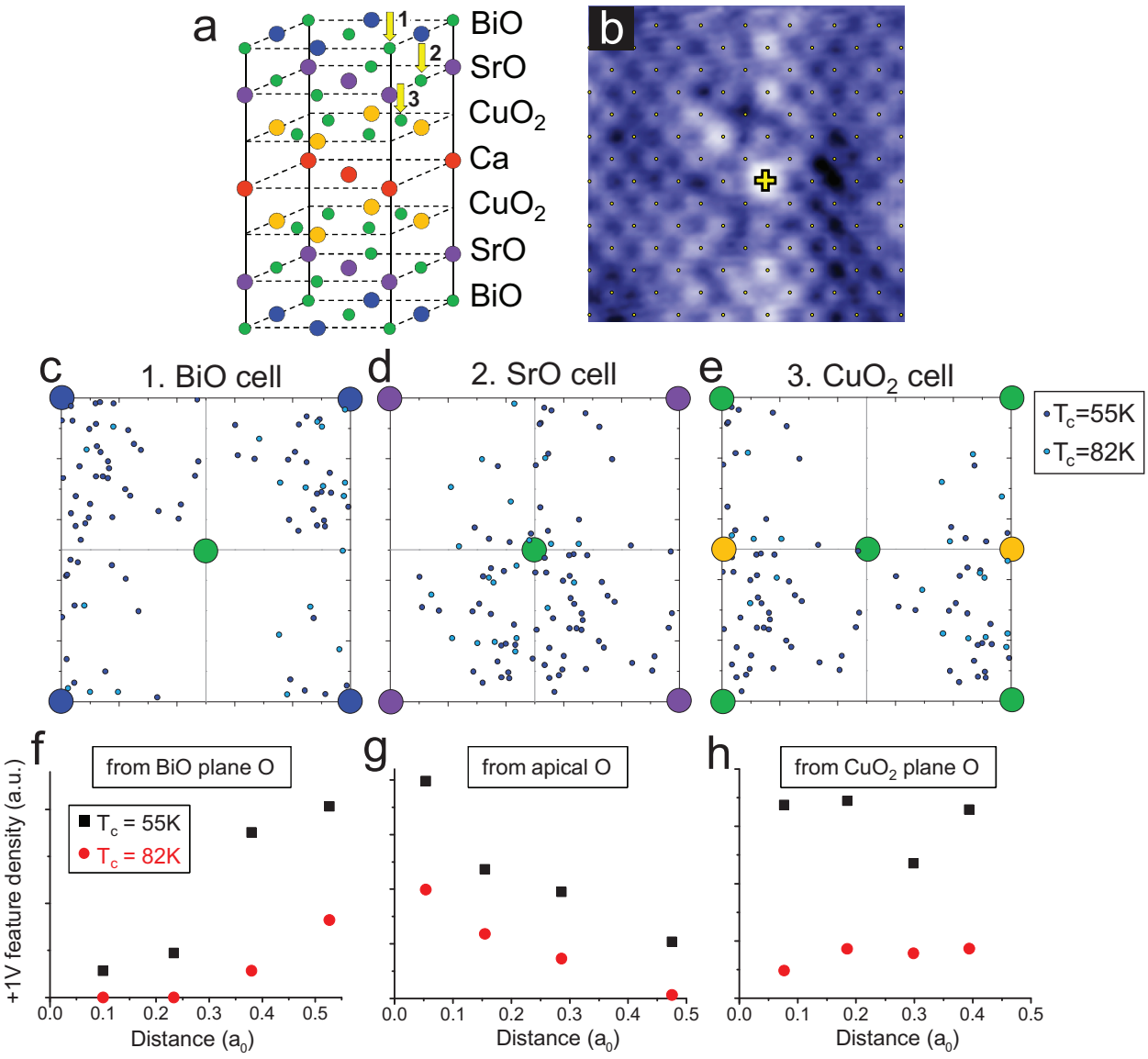

Figure 4.2.2: (a) Top half of Bi-2212 unit cell denoting the three inequivalent lattice oxygen sites. (b) Drift-corrected Bi-2212 topograph (V_{sample}=600 pA, I_{set}=+150 mV) over a 4 nm area, with a perfect square lattice of small yellow circles superimposed. The yellow cross denotes the position of one +1 V feature. The brightness of this spot suggests that the +1 V feature is not a missing Bi atom. (c-e) Positions of each localized +1V feature (blue dots) within a single unit cell in two samples. (c) is plotted with respect to the BiO layer (Bi: blue; O:green); (d) is plotted with respect to the SrO layer (Sr: purple; O: green); (e) is plotted with respect to the CuO_2 layer (Cu: orange; O: green).(f-h) Areal density of +1 V features as a function of lateral distance from each of the three distinct oxygen lattice sites shown in (c-e).

with the apical oxygen site. This conclusion is reinforced by plotting the density of observed +1 V features vs. distance from each of the 3 possible O sites, in Fig. 4.2.2f-h.

4.3 Correlation of Oxygen Dopants with the Pseudogap State

Having identified the positions of three types of O dopants, I proceed to discuss the correlation between the local observation of these and the inhomogeneous PG state. Fig. 4.3.1a-c shows the three types of dopants (type-B O, type-A O and AOV respectively), superimposed on a PG map acquired for the T_c=55 K sample (see Appendix A.2.1 for details of PG determination). Any correlation between type-B Os and PG is too weak to be seen by the naked eye. In contrast to Zhou's prediction, the type-A Os are correlated with regions of large PG. One immediately sees the strongest correlation between AOVs and PG. Fig. 4.3.1d shows the crosscorrelations between the positions of the dopant atoms and the corresponding gap map (for crosscorrelation algorithm details, see Appendix A.2.2). Fig. 4.3.1e shows the average PG as a function of distance from the nearest dopant. This behavior is consistent across the three underdoped samples studied (Appendix A.2.3).

We examined more carefully the surprising departure from Zhou's prediction in Fig. 4.3.2, which plots the local PG energy versus the local concentration of each dopant type. For the type-B interstitial Os in Fig. 4.3.2a, the local trend within each sample shows correlation between increased local oxygen concentration and increased local PG; the global trend between samples shows anticorrelation between global oxygen concentration and global PG. In contrast to Zhou's prediction, Fig. 4.3.2b shows that a qualitatively similar juxtaposition of local and global trends holds for the type-A interstitial oxygens in the three underdoped samples. However, Fig. 4.3.2c shows excellent alignment of local and global trends for the correlation between AOV density and PG. This suggests that, in underdoped samples, variations in the local hole concentration, and thus the local PG, are governed primarily by the local removal of holes by AOVs, rather than the strain or the donation of localized holes from the interstitial oxygens. The interstitial oxygens, previously predicted [60] to determine the local gap, do contribute de-localized holes, but in underdoped samples even the type-A interstitial O positions remain correlated to regions of decreased local hole concentration, likely due to a tendency to remain close to the AOVs. In the optimally doped sample, the AOV concentration is negligible, so the local hole concentration may be set by the next-closest dopant to the CuO_2 plane, the type-A interstitial O, as predicted by Zhou *et al.* [64]. Indeed,

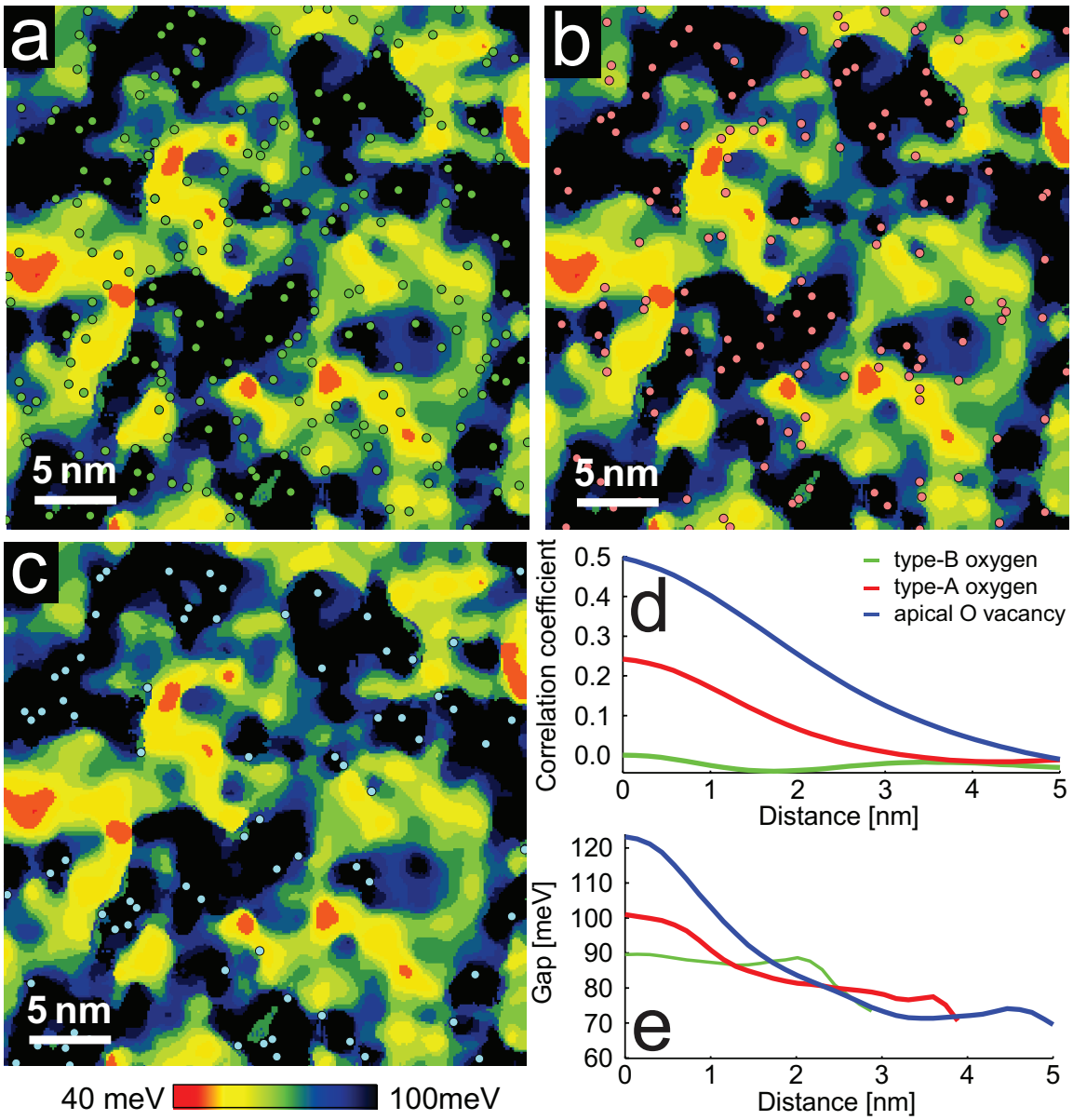

Figure 4.3.1: Locations of (a) type-B interstitial Os (green circles), (b) type-A interstitial oxygens (red circles), and (c) AOVs (blue circles) superimposed on top of the PG map of the T_c=55 K sample. (d) Cross-correlation coefficient relating the PG to the distance to the nearest dopant. (e) Average PG versus distance from the nearest dopant of each type. In (d) and (e), green, red, and blue lines represent type-B oxygens, type-A oxygens, and AOVs, respectively.

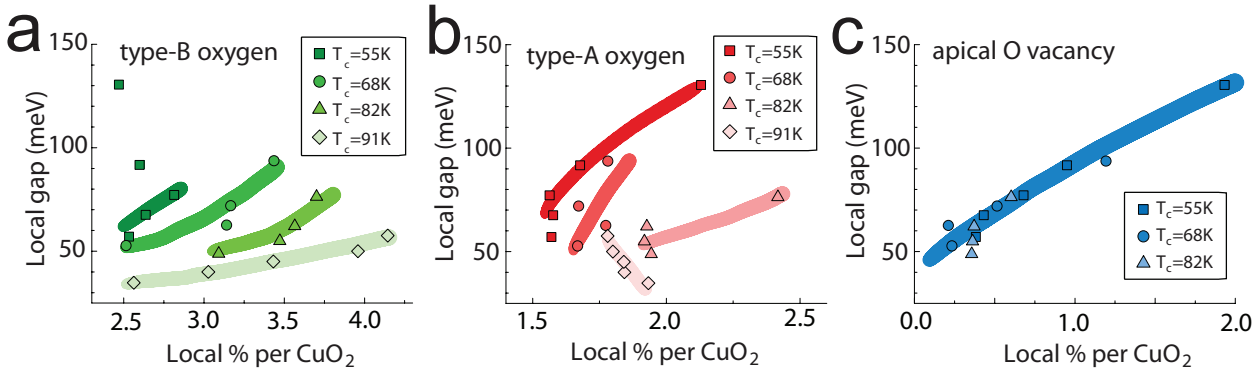

Figure 4.3.2: For each sample, we create a local density map of the number of a given dopant type per region of radius x∼2 nm. The values in the density map are then binned based on the PG value at the corresponding pixel. The average PG value in each bin is then plotted versus the average dopant density value within each bin. (a) Local PG versus local density of type-B interstitial oxygen dopants, from the four different samples used in this study. (b) Local PG versus local density of type-A interstitial oxygen dopants, from the four different samples used in this study. (c) Local PG versus local density of apical oxygen vacancies, from the three underdoped samples used in this study. Trend lines in (a) to (c) are guides to the eye.

Fig. 4.3.2b shows that the local PG decreases with increasing local type-A concentration in the T_c=91 K sample. We therefore reconcile the apparent contradiction between the global [8] and local [44, 61] doping trends for both types of interstitial oxygens.

4.4 Correlation of Oxygen Dopants with Checkerboard Charge Order

Another manifestation of electronic inhomogeneity is a disordered CB modulation of the spectral weight that is static and possibly associated with the PG phase. A closely related disordered QPI periodic inhomogeneity may exist at similar wave vectors to the static CB, but only at a limited range of energies within the superconducting gap [58]. It was previously claimed that type-B O dopants are found in the minima of the QPI patterns [61], at both positive and negative energies. However, QPI has opposite spatial phase for filled and empty states [66], suggesting that the previously observed correlation [61] relates instead to the CB.

First, we have closely examined the energy dependence of the CB pattern observed in our Bi-2212 samples. Due to insensitivity of CB wavevector to imaging bias (see Appendix A.3.1), it can be concluded

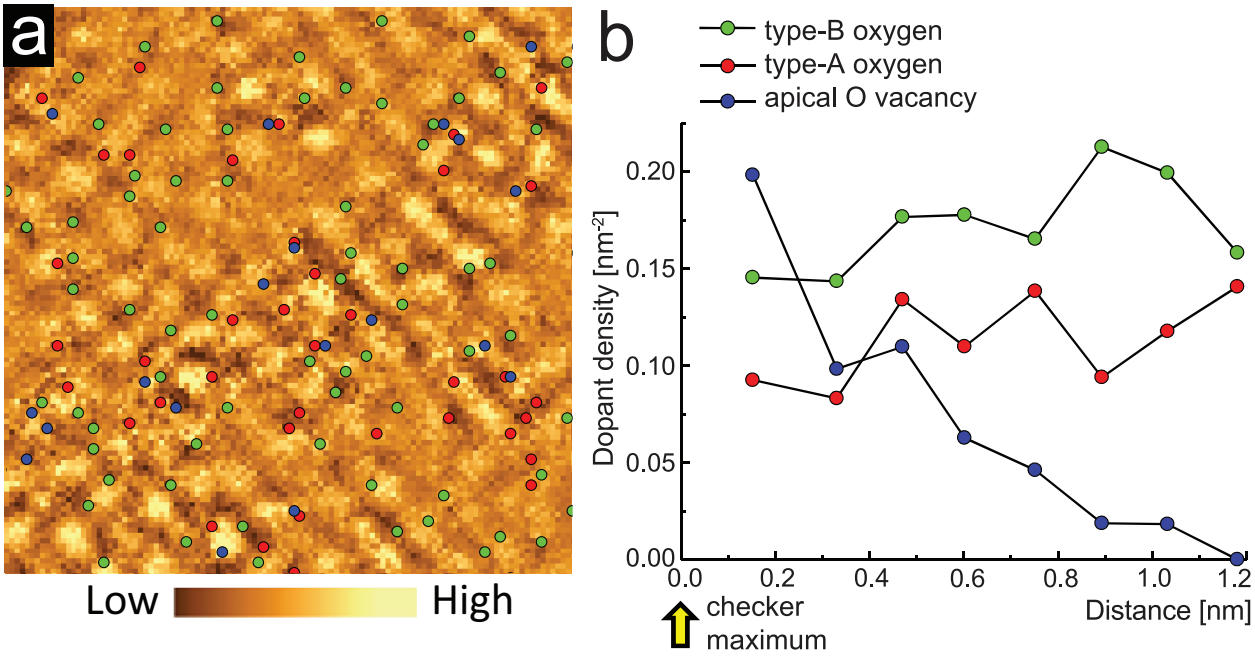

Figure 4.4.1: (a) Fourier-filtered dI/dV image of the T_c=55 K sample at +36 mV, showing a clear CB (setup: V_{sample}=−150 mV; I_{set}=800 pA). Type-B Os, type-A Os, and AOVs are superimposed as green, red, and blue circles, respectively. (b) Dopant density of each dopant type versus distance from the center of the nearest CB maximum.

that the phenomenon observed is indeed static CB modulation, and not energy-dispersive QPI.

Figure 4.4.1a shows the distribution of the three types of observed atomic dopants on top of a low-pass filtered $dI/dV(36\text{ mV})$ image. A histogram of the distance from each dopant to the center of the nearest "checker" (Fig. 4.4.1b) demonstrates the strong tendency of AOVs to lie in the peaks of the imaged CB and a weaker tendency for interstitial O dopants to lie in the troughs (see Appendix A.3.2 for algorithm details). We therefore conclude that the AOVs play the primary role in pinning the CB.

4.5 Comparison of Oxygen Disorder to Other Types of Disorder

In addition to previously described O dopant disorder, there exist several other kinds of chemical disorder in Bi-2212 investigated in literature.

- **Sr site defects.** Since Bi-2212 crystals are difficult to synthesize in the perfectly stoichiometric form [67], extra Bi atoms are commonly used to facilitate the growth process, and most crystals contain $\sim 5-10\%$ excess Bi substituted at the Sr site [67]. Because the Sr site is located next to the apical O site (which is directly above Cu, see crystal structure in Fig. 1.2.3a), it might be expected that the substitution at this site would have a strong effect on the electronic properties of the crucial CuO_2 plane. Kinoda *et al.* imaged Sr site defects as a set of bright features in STM topographs of Pb-doped Bi-2212 at bias greater than + 1.4 V. The dI/dV spectrum on top of a Sr site defect shows a resonance peak at + 1.7 V. Even though no quantitative analysis was presented [68], we have analyzed the published data to obtain only a small positive correlation between the two of ~ 0.25 as compared to ~ 0.5 for AOVs. Hence, although not the strongest correlation, Sr site defects also seem to be correlated with the observed PG state inhomogeneity.

- **Cu site defects.** It has been reported that Cu site impurities (Ni, Zn dopants and intrinsic crystal defects), have a tendency to appear in the areas of small spectral gap (<50 meV) [69]. However, since spectral gap inhomogeneity is observed in the absence of Zn or Ni doping (or intrinsic crystal defects which we rarely observe in our extensive studies of Bi-2212), we rule these out as the cause of the spectral gap variation. Nevertheless, due to the correlation of their distributions with the areas of the small spectral gap, it seems plausible that the electronic inhomogeneity could be pinned by (some of) these impurities.

- **Pb substitutions.** Kinoda *et al.* studied heavily-overdoped Bi-2212 crystals with Pb substitutions [68] and claimed to observe no correlation between the Pb dopant positions and the magnitude of the spectral gap, therefore ruling out these dopants as the cause or the pinning sites of the nanoscale heterogeneity. The lack of correlation between Pb dopants and the spectral gap was consequently confirmed in Pb-doped Bi-2201 crystals [70]. Both experiments seem to agree that although Pb dopants add carriers and alter structure, their effect on the electronic properties is not localized.

4.6 Conclusion and Discussion

In conclusion, we have extended the energy range of local spectroscopy on Bi-2212 by $\sim$50% to image for the first time two types of interstitial O dopant atoms, as well as AOVs. We have shown that AOVs have the strongest local correlation with the areas of the large PG, whereas the correlation of type-A O and

type-B O dopants with PG is comparatively much weaker. It can be concluded that AOVs enhance the magnitude of PG phase locally and pin the maxima of CB charge modulation, while the interstitial O atoms contribute mostly delocalized charge and may exhibit weak tendency to occur in the minima of CB charge modulation. Based on other experimental studies, the correlation of other types of defects such as Sr and Cu site defects, and Pb substitutions seem to be weaker compared to the AOVs. Finally, the discovery of AOVs and type-A O resolves an outstanding mystery of opposing local *vs.* global correlations between interstitial O dopants and the PG.

But a question remains – does dopant inhomogeneity cause PG inhomogeneity or merely pin intrinsic inhomogeneity, caused perhaps by strong correlations? Because the 2- to 3- nm length scale of PG inhomogeneity remains the same across a wide range of dopant concentrations (Fig. A.2.3a, inset), intrinsic PG inhomogeneity seems plausible. However, our experiment shows clearly that the dopant locations that are fixed at room temperature, particularly the apical oxygen vacancies, do enhance the local PG strength that is subsequently determined on cooling through the PG transition temperature T^*.

Finally, is there a relationship between apical oxygens and superconductivity itself? In fact, apical oxygen effects may be credited for the discovery of high-T_c superconductivity, as Müller was originally driven to explore the LaBaCuO system by the expectation of strong electron-phonon coupling due to the Jahn-Teller effect in the CuO_6 octahedral environment, specifically the displacement of the Cu-apical-O bond [5]. However, subsequent isotope effect measurements suggested that any phonon contribution to superconductivity is dominated by CuO_2 plane oxygen [71]. We conjecture that AOVs influence the superconductivity indirectly in underdoped samples by reducing the local hole concentration, which locally strengthens the PG, tying up antinodal states [54, 56], and locally decreasing the Fermi level carriers that would otherwise be available for coherent pairing. Calculations also showed a correlation between T_c and apical oxygen height and emphasized the importance of the axial orbital for the hopping and phase coherence necessary for superconductivity [72, 73]. Thus, AOVs may lower the local superconducting T_c and/or critical current J_c. We propose a possible route to increase T_c in Bi-2212: underdope to increase the pairing potential [74] but explore different annealing recipes to allow interstitial oxygen removal without creating AOVs, the defects most favorable to the PG and possibly competitive to superconductivity. Recently, a $\sim 15\%$ increase in maximum T_c has been predicted from alternate dopant arrangements [75].

5

Oxygen Dopant Disorder and Strain in Bi-2212

5.1 Introduction

As discussed in previous chapters, Bi-based cuprates are an exceptionally complex family of materials. Even though STM has proven to be the front-runner technique in studying these materials at the atomic scale [76, 77], the interpretation of the results has sometimes been hindered by the intricacy of the crystal structure. The ideal lattice of Bi-2212 is complicated due to the presence of commensurate (see Chapter 3) and incommensurate supermodulation (SM) structural distortions [11] that pervade the bulk of the crystal, off-stoichiometric doping of oxygen atoms and cation-substitutions [65, 67]. In Chapter 4, we have shown the first direct imaging of all oxygen dopants introduced in the parent compound to induce superconductivity in this material. However, the exact intra-unit-cell positions and electronic effects of these dopants remain controversial.

With recent advances in algorithms used to analyze STM data [43], it is now possible to determine the positions of atoms in STM topographs with picometer precision. Using the Lawler–Fujita drift-correction

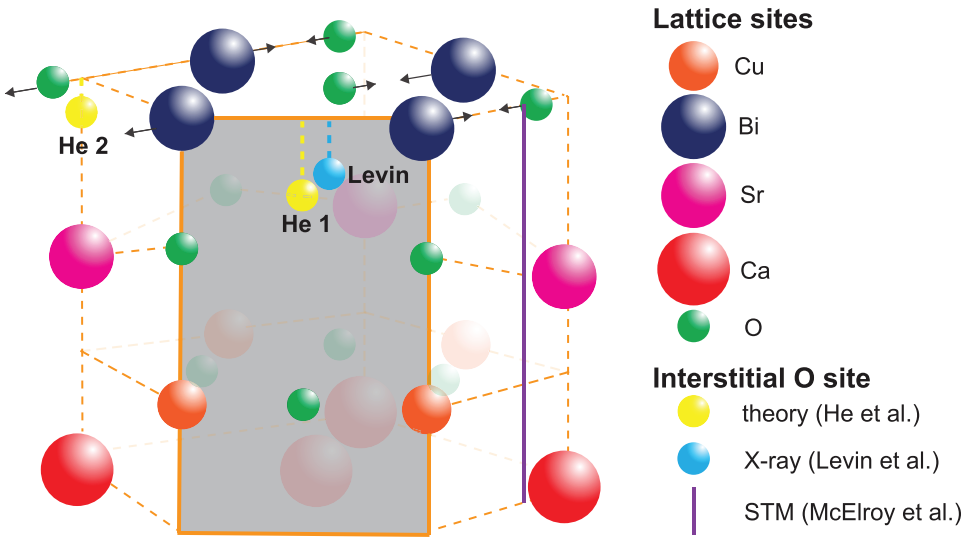

Figure 5.2.1: Gray shaded area represents a vertical "cut" through the crystal structure of Bi-2212 to emphasize the positions of type-B Os. Yellow spheres represent the type-B O positions predicted by theory, and light blue sphere is the position extracted from X-ray experiments. Pink vertical line shows the position of type-B O atoms obtained by McElroy *et al.* Only four layers (BiO, SrO, CuO_2 and Ca) of the Bi-2212 unit cell are shown for simplicity. Black arrows denote the direction of orthorhombic distortion of Bi and O atoms in the BiO layer.

algorithm [43], we are able to pinpoint the exact positions of both types of interstitial oxygen dopants within the unit cell, and show how their distributions are related to AOVs. We also discovered that the spatial distribution of one type of interstitial oxygen atoms is tied to the periodicity of the SM.

5.2 Previous Experimental and Theoretical Studies

Early X-ray studies on dopant disorder in Bi-2212 [78–81] have found extra oxygen atoms inserted into the BiO plane, but their exact positions within the unit cell have been complicated to extract due to the difficulty of analyzing higher harmonics of the SM. In an X-ray study done almost 20 years ago, Levin *et al.* determined that the interstitial oxygen atoms are laterally located one half of the distance between neighboring Bi atoms [81] (blue sphere in Fig. 5.2.1). No real-space probe has been able to evaluate this observation until an STM study imaged one subset of oxygen dopants as atomic-scale resonances in

dI/dV maps at -1 V bias (type-B O) [61], and determined their position to be approximately 0.9 Å away from the O in the BiO layer, along the BiO direction (purple line in Fig. 5.2.1). A theoretical study used density-functional calculations to determine several stable positions of type-B O atoms within the unit cell that reproduced the resonance in dI/dV at -1 V bias [82]. The most energetically favorable position was found to be in a vertical plane connecting two neighboring Bi atoms ("He1" yellow sphere in Fig. 5.2.1). However, none of these theories or experiments took into account the orthorhombic distortion of the unit cell (Chapter 3).

5.3 Intra-unit-cell Position Determination

To determine the positions of both type-A and type-B O dopants within the Bi-2212 unit cell, we acquire topographs and simultaneous dI/dV images of BiO layer at -1 and -1.5 V bias (Chapter 4), and locate the exact positions of oxygen dopants with respect to the Bi lattice seen in the topographs. We use the Lawler-Fujita drift-correction algorithm [43] with short correction length scale $\sim a_o$ on all our data that removes the artifact slow drift due to experimental conditions and most of the true lateral distortion due to incommensurate SM, and places Bi atoms on a nearly perfect square lattice (Appendix A.1). To determine the centers of individual dopant atoms, we use a simple two-dimensional Gaussian fitting method. Since apparent positions of dopants determined by this method can be influenced by other dopants in the vicinity, we determine the positions of only the dopants where we can choose a rectangular fitting window (FW) that completely encompasses exactly one atom. The dopant position determined by this procedure is insensitive to the size of the FW that we choose, as it varies by less than 0.4% of a unit cell with the varying size of FW.

Fig. 5.3.1a shows the scatterplot of the lateral positions of type-B O dopants within two different orthorhombic BiO unit cells. In a perfect tetragonal cell, type-B O locations would appear to be directly above the O site in the BiO layer (O(Bi)), which would be impossible due to the lattice O already occupying the site. However, we resolve this apparent discrepancy by separating the distribution of dopant locations into two distinct positions within the orthorhombic unit cell. Each lattice O shifts $\sim$12% away from the high symmetry point [83], and we now find that type-B interstitial Os are located on the opposite side of the unit cell from the shifted lattice O. Furthermore, the distribution of type-B Os is "stretched" along one particular Bi-O direction which is parallel to the SM wavevector in both samples

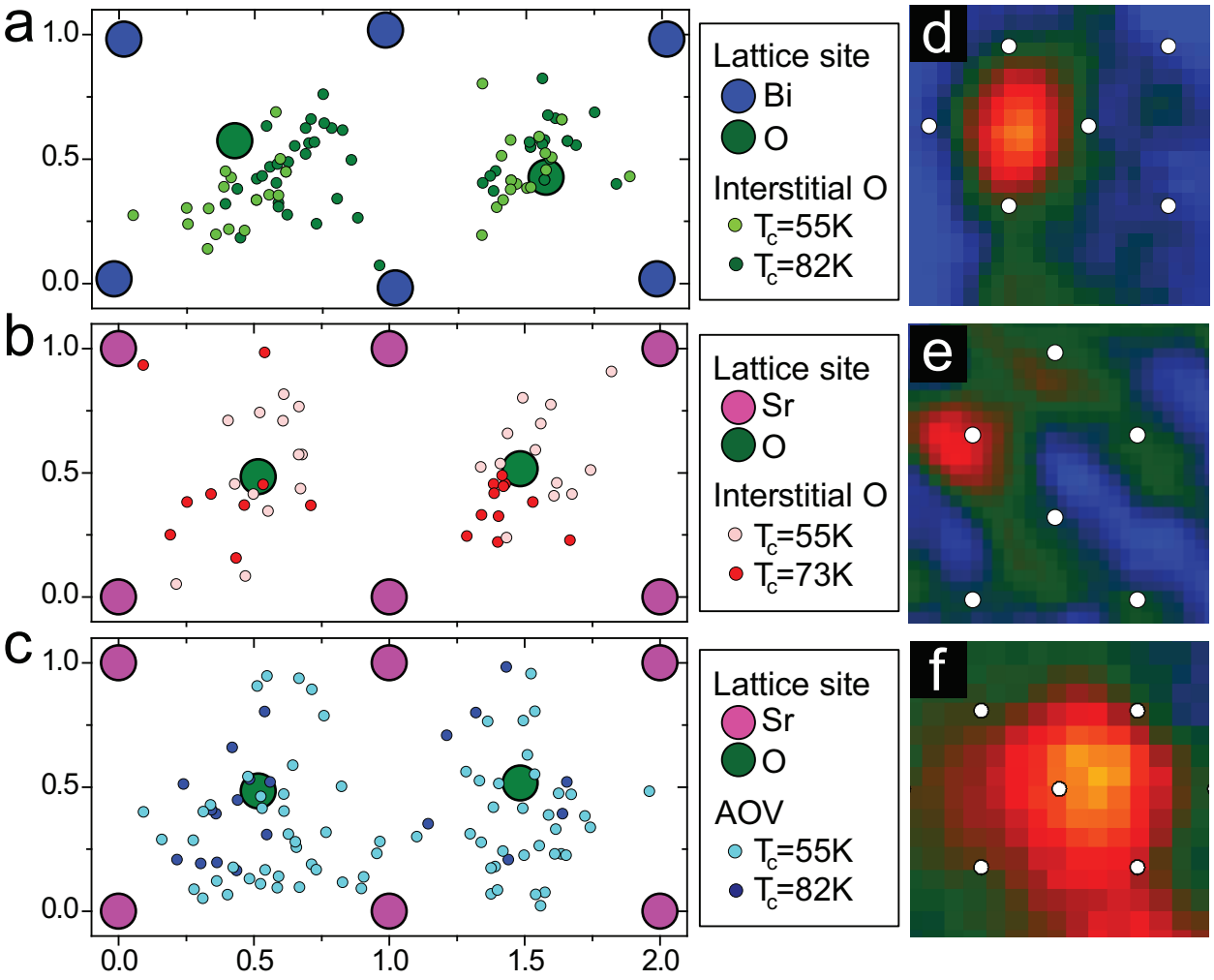

Figure 5.3.1: (a-c) Distributions of type-B O, type-A O and AOV within the orthorhombic unit cell for two different samples. Coordinates of the lattice atoms in all panels have been taken from a neutron diffraction study by Miles *et al.* [83]. (d-f) dI/dV map of 1 nm square region containing a single type-B O (-1 V), type-A O (-1.5 V) and AOV ($+1$ V) respectively, for T_c=73 K sample. Setup conditions for (d-f) are -1 V, -1.5 V, $+1$ V and 300 pA, 50 pA, 200 pA respectively. Open white circles show the idealized Bi lattice in the simultaneously acquired BiO topographs.

studied. It can be concluded that type-B O atoms lie directly below O(Bi), consistent with the second most energetically favorable position "He 2" shown in Figure 5.2.1.

We repeat the same process to locate the positions of type-A Os, place them within two distinct orthorhombic SrO unit cells, and find that they lie at the lattice O site in the SrO layer (O(Sr)) (Fig. 5.3.1b). No discernible difference can be seen between the distributions in the two orthorhombic unit cells, which is somewhat expected as the orthorhombic distortion affecting O(Sr) is much smaller than the corresponding distortion of O(Bi). However, O(Sr) is vertically displaced by $\sim$ 0.6 Å compared to the plane containing Sr atoms, thus possibly leaving enough space for type-A Os to position themselves just below O(Sr). For comparison, we plot again the scatterplot of AOVs in Fig.5.3.1c (shown in Chapter 4). Due to the apparent larger size of the AOVs (compared to interstitial Os), a greater scatter of points exists between Fig. 5.3.1a and Figs. 5.3.1a-b. In order to illustrate the difference in apparent sizes between different dopants in dI/dV images, Figs. 5.3.1d-f show a 1 nm dI/dV map with exactly one type-B O, type-A and AOV respectively. The surprising conclusion of the analysis of positions of both types of interstitial oxygen atoms is that the two clearly different positions we observe are both inconsistent with the theoretically predicted position "He 1" and X-ray position "Levin", both shown in Fig. 5.2.1.

5.4 Relationship between Oxygen Disorder and Supermodulation Structural Buckling

We further investigate the relationship between the distribution of interstitial oxygen atoms, AOVs, and the incommensurate structural SM. The period of the SM in Bi-2212 is $\sim$7 unit cells, and is oriented 45° with respect to the Cu-O bond. We use an algorithm described in detail by Slezak *et al.* [84] to determine the phase of the SM for every pixel in the field-of-view (FOV), and calculate the average density of the dopants of each type as a function of the SM phase. Fig. 5.4.1a shows a 2.5 nm wide atomically-resolved topograph of Bi-2212. Type-A O dopant density as a function of the SM phase is shown in Fig. 5.4.1b, and it reveals a strong inclination of type-A O dopants to sit in the peaks of the SM. This observation is in contrast to previously investigated type-B O dopant spatial dependence [84] that might exhibit a weak bimodal distribution for some samples, peaking at both the crests and the troughs of the SM (Fig. 5.4.1c). So for the first time we have identified a set of oxygen dopants that are spatially distributed with the SM periodicity. AOVs may also be more likely to appear in the peaks of the SM (Fig. 5.4.1d), but this

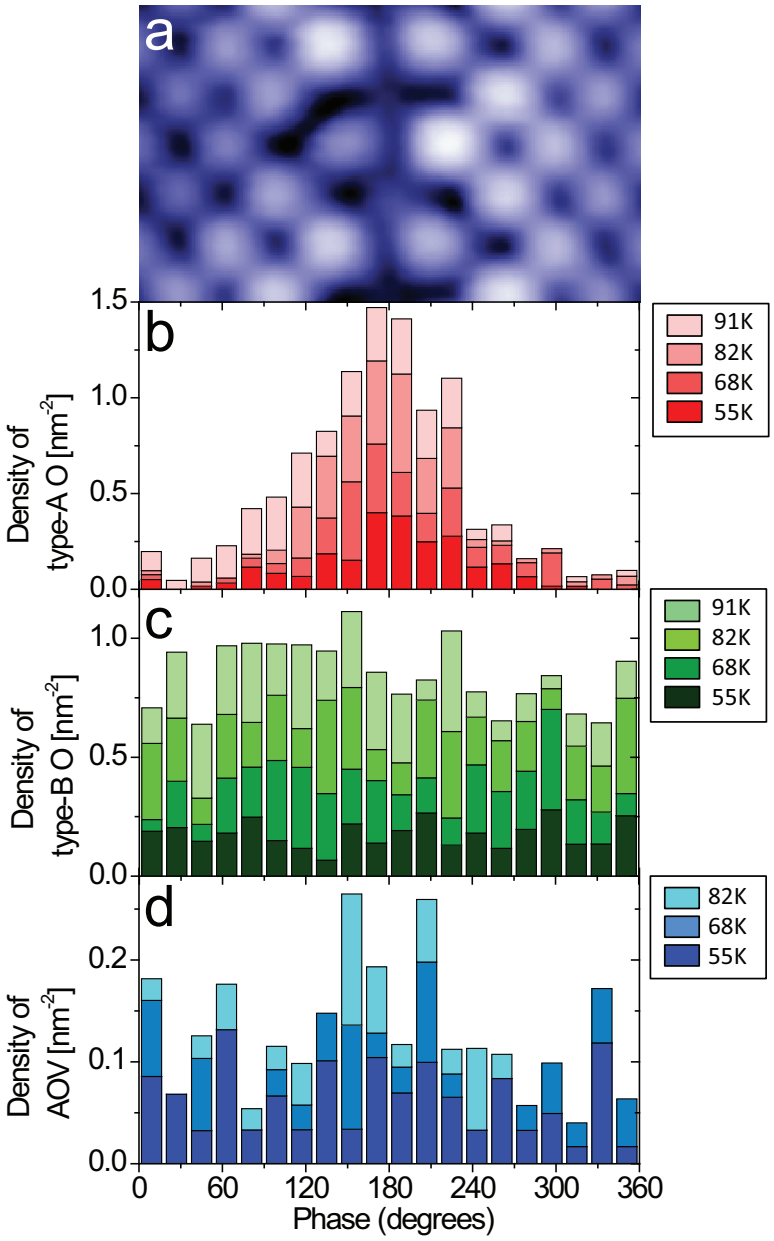

Figure 5.4.1: (a) BiO layer STM topograph acquired at 200 mV and 50 pA, ∼2.5 nm wide, showing distortions in the Bi lattice over one period of the SM. (b-d) Histograms of densities of type-A O, type-B O and AOVs respectively as a function of the phase of the SM. Different shades of red, green and blue indicate data obtained on samples of different doping concentrations. Peak of the SM is at 180 degrees as emphasized by the topograph in (a).

tendency is much weaker compared to the sharply peaked distribution of type-A Os in Fig. 5.4.1b.

5.5 Nature of Oxygen Dopant Distributions

Having identified the positions of all interstitial oxygen atoms and AOVs within the same FOV, we proceed to determine if different sets of dopants are prone to clustering, or if their distributions are uncorrelated with one another. The algorithm used to extract this information essentially histograms and compares pair-wise distances in experimental and random datasets to extract their ratio as a function of distance (described in detail in Appendix B.1). If the obtained ratio quotient is:

- >1 then the dopants **attract** (prefer clustering)
- ~ 1 then the dopant distribution is **random**
- <1 then the dopants **repel** and are even more homogenous than you would expect from a random distribution

Both type-A and type-B Os show a tendency to repel each other (Fig. 5.5.1a-b) in all samples except for type-A Os in the most underdoped T_c=55 K sample. This tendency is expected from particles of like-charge that prefer keeping themselves as far as possible from one another. The distribution of type-A Os in the T_c=55 K sample is likely affected by AOVs, as the two have a strong positive correlation in all samples (Fig. 5.5.1c), with the correlation being the strongest in the T_c=55 K sample. The interstitial atom – lattice vacancy pairs, known as Frenkel defects that were first theoretically predicted to exist in 1926 [85], have since also been observed as displaced oxygen atoms near lattice vacancies in TiO_2 [86]. Furthermore, since AOVs create a cloud of local positive charge, one would expect negatively charged interstitial oxygen atoms to be attracted towards the vacancies. We also observe a positive correlation between type-B O atoms and AOVs (Fig. 5.5.1d), but this correlation seems to be much weaker than the correlation between type-A Os and AOVs. Since AOVs have a well-defined position in the SrO layer, this information provides us with a clue that type-A O atoms are indeed in the SrO layer, as it has been previously predicted [64]. Finally, we find that the AOVs like to cluster together, with a preferable separation of $\sim$2-4 nm (Fig. 5.5.1e). Correlation between type-A O and type-B O is inconsistent between different samples, exhibiting a weak negative correlation in the most underdoped sample, and a positive correlation in the optimally doped sample in the absence of AOVs (Fig. 5.5.1f).

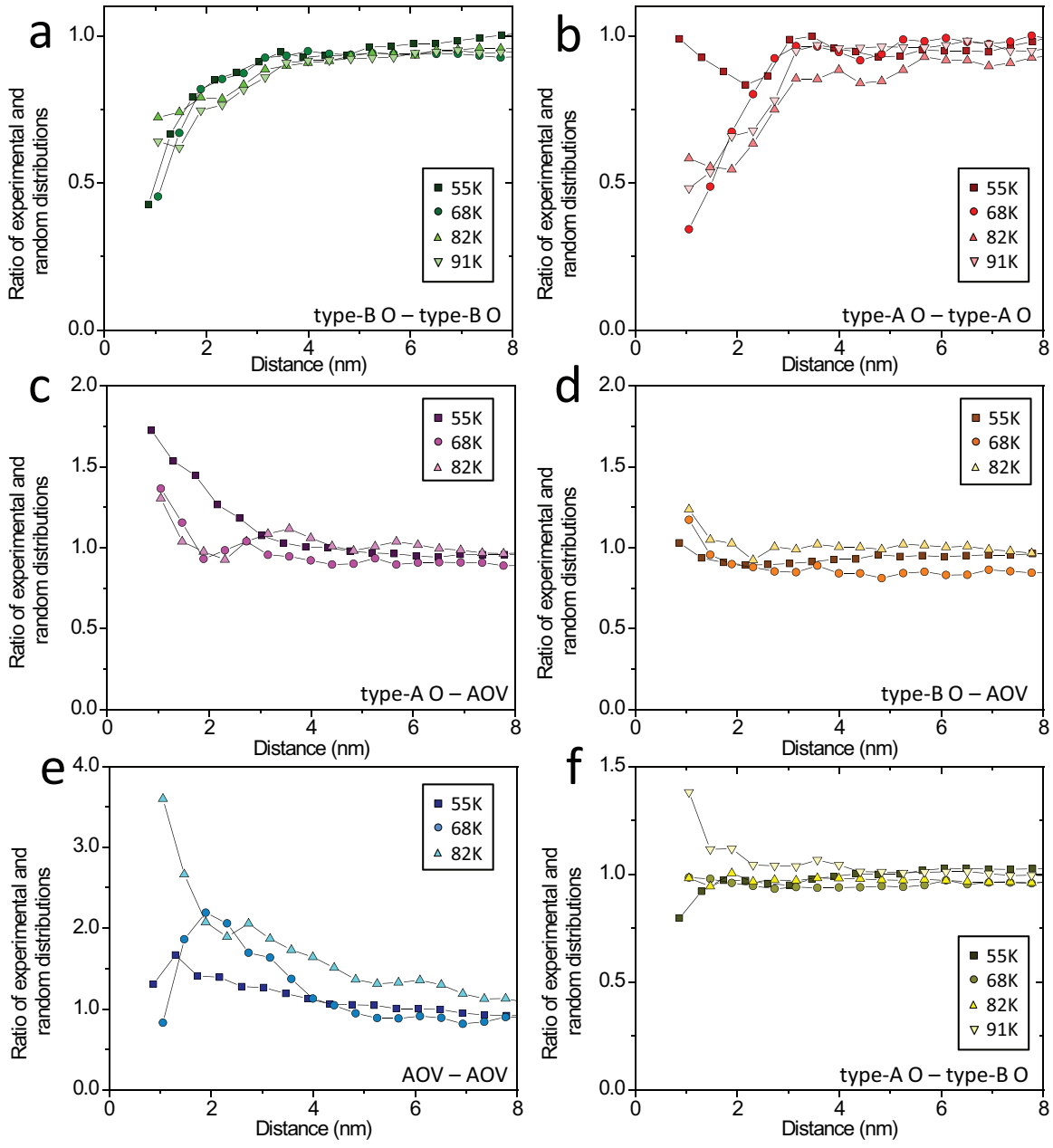

Figure 5.5.1: (a-f) Ratios of experimental and random distributions of dopants as a function of distance for type-B O – type-B O, type-A O – type-A O, type-A O – AOV, type-B O – AOV, AOV – AOV, and type-A O – type-B O respectively. Values of the ratio greater than 1 indicate inclination of two types of dopants to appear closer to each other compared to a random distribution, whereas values that are less than 1 signal tendency of the two types of dopants to "repel" each other.

5.6 Conclusion and Discussion

In this Chapter, we have presented a comprehensive investigation of the role of strain on the intra-unit-cell placement of both types of interstitial oxygen dopants, and discussed the correlation of interstitial Os and AOVs. We have shown that type-B O dopant lateral position is located at the O site in the BiO plane (consistent with "He 2" position, see Fig. 5.2.1), and that the strain of the orthorhombic distortion plays an important part in allowing this intra-unit-cell location. Furthermore, type-A O dopants are located closer to the apical O site, likely just below O(Sr) in the SrO layer as previously predicted [64] due to their strong tendency to occur in the vicinity of AOVs (which have a well-defined position in the SrO plane). Type-A O dopants also exhibit a strong tendency to lie in the peaks of the incommensurate SM. We hypothesize that SM strain, which "pushes" atoms further apart in its crest, creates extra space for type-A O dopants to fit within the crystal. We hope that the precise identification of the exact positions of all interstitial oxygen atoms within the unit cell will allow more computational modeling and theoretical work to be done to further the understanding of the impact of strain on the electronic states in Bi-2212.

6

Impurity-induced Bound States and Electronic Inhomogeneity in $Y_{1-x}Ca_xBa_2Cu_3O_{7-x}$

6.1 Introduction

The main obstacle in studying YBCO single-crystals using surface-sensitive probes is the surface "overdoping" catastrophe produced during the process of cleaving [87], which in turn results in a non-superconducting topmost bilayer. Furthermore, YBCO lacks a natural cleavage plane, and cryogenically-cleaved surfaces usually reveal either the BaO plane or CuO chain plane. The BaO termination plane is observed in STM topographs as a clean square lattice of Ba atoms (Fig. 1.2.3f). The cleaved CuO chain surface exhibits a complicated one-dimensional modulation (Fig. 1.2.3e) initially attributed to a CDW state [18, 19, 88], but later proposed to be a consequence of superconducting quasiparticle scattering, likely due to O vacancies in the CuO chain plane [89]. Although these surfaces may be imaged with atomic resolution, neither show a gap which is proven to be of superconducting

origin by temperature or magnetic field dependence. As-grown surfaces of YBCO do retain their bulk superconducting properties as demonstrated by direct vortex imaging [90], but lack the atomic resolution of cryogenically-cleaved YBCO. Recently, Ca substitution at the Y site in YBCO has been shown to circumvent the overdoping problem [87]. Furthermore, Zabolotnyy *et al.* hypothesized that this substitution resulted in an alternate cleavage plane due to the strain introduced by the Ca dopants. To test this hypothesis, a local probe is naturally needed.

6.2 Surface Morphology

Single-crystals of underdoped $Y_{1-x}Ca_xBa_2Cu_3O_{7-x}$ (Ca-YBCO) used in the study contain $\sim$10% Ca substitution at the Y site, which has been checked with energy-dispersive X-ray measurements. Each Ca^{2+} substitution at the Y^{3+} donates one hole to the bulk. Since Ca-YBCO is a double-layer system, $\sim$10% Ca substitutions leads to $\sim$5% hole doping per CuO_2. For the equivalent Ca-free $YBa_2Cu_3O_{7-x}$ (YBCO) crystals with oxygen content $6 + x = 6.4$, we estimated a hole doping level of $\sim$7% based on the *c*-axis lattice parameter of the crystal [91]. Therefore, we annealed the Ca-doped crystals to this oxygen doping level, which should give a total hole doping level of $\sim$12%. The Ca-YBCO crystals have a superconducting T_c of about 30 K, defined as the midpoint of the transition (Fig. 6.2.1a).

Single crystals of Ca-YBCO with T_c of $\sim$30 K are cleaved in ultra-high vacuum at cryogenic temperature, and immediately inserted into the STM head where they are imaged with a PtIr tip, cleaned by field emission on polycrystalline Au foil. Fig. 6.2.1b shows a typical STM topograph obtained on cryogenically-cleaved surfaces of Ca-YBCO samples. In contrast to the atomically-resolved CuO chain plane or BaO surface seen in optimally doped YBCO (without Ca substitutions), no atomic resolution has been achieved in Ca-YBCO. The surface is disordered but atomically flat, with no step edges or valleys appearing over several hundred nanometer areas (Fig. 6.2.1c). Our observation is consistent with the hypothesis that Ca doping in YBCO results in an alternate cleavage plane, which is distinct from either CuO or BaO planes and is presumed to be the Y/Ca layer [87]. We deem the CuO_2 surface termination unlikely to explain the disordered surface seen in Figs. 6.2.1b-c, as atomically-resolved CuO_2 surfaces have been imaged in Bi-2212 [92], and we observe no atomic signature. We further note that similar observations of a disordered surface has been reported in $Pr_xCa_{1-x}Fe_2As_2$ where reconstruction of a fraction of the Ca-layer results in a "web-like" surface morphology (Chapter 7). Therefore, we suggest that

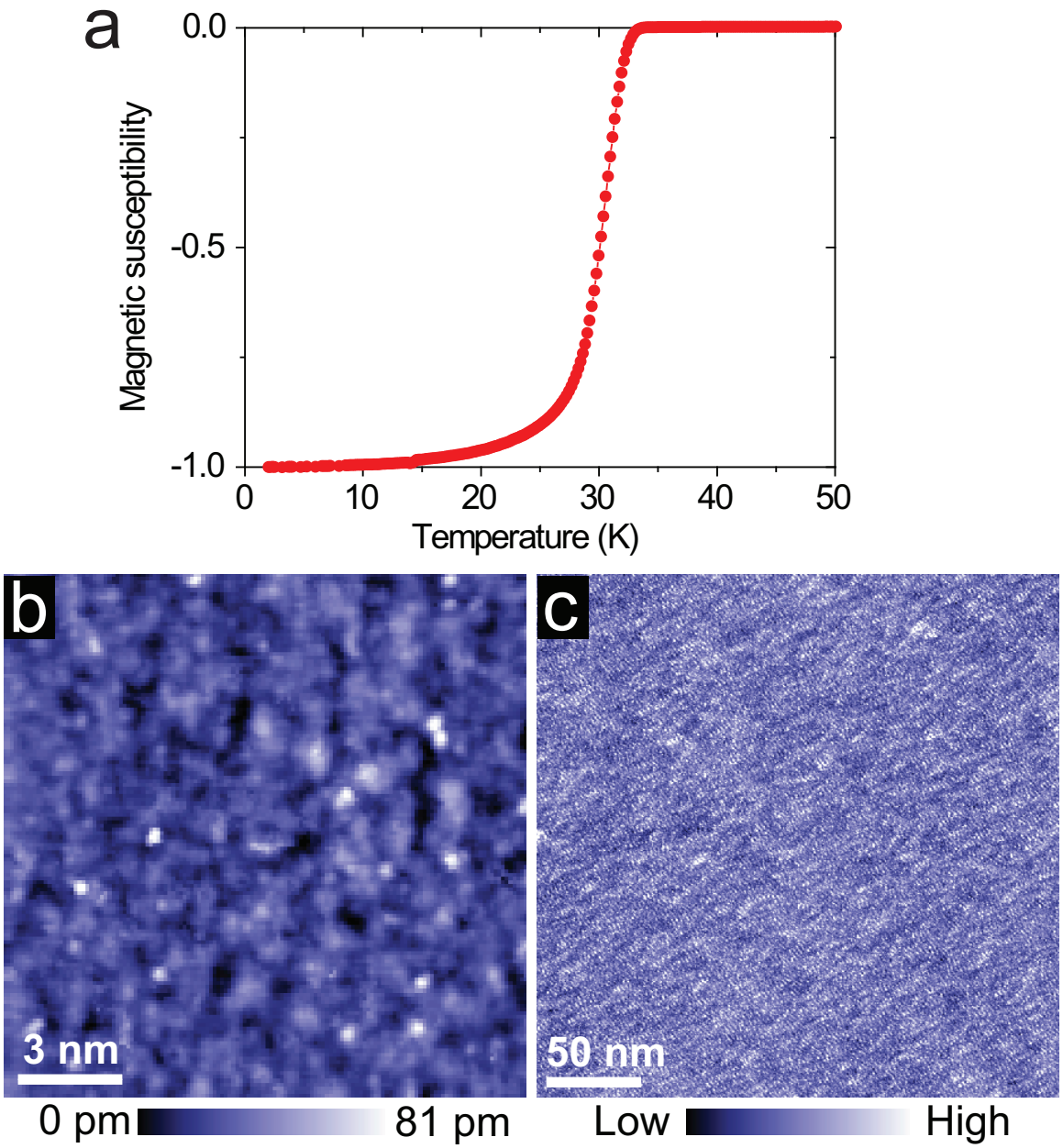

Figure 6.2.1: (a) Magnetic susceptibility measurements of Ca-YBCO samples with T_c ∼30 K as determined by the midpoint of the superconducting transition. STM topographs of Ca-YBCO, revealing a new, disordered surface morphology over (b) 15 nm, and (c)∼300 nm square regions. Setup conditions in (b): I_{set}=500 pA and V_{set}=-60 mV; in (c): I_{set}=10 pA and V_{set}=-500 mV.

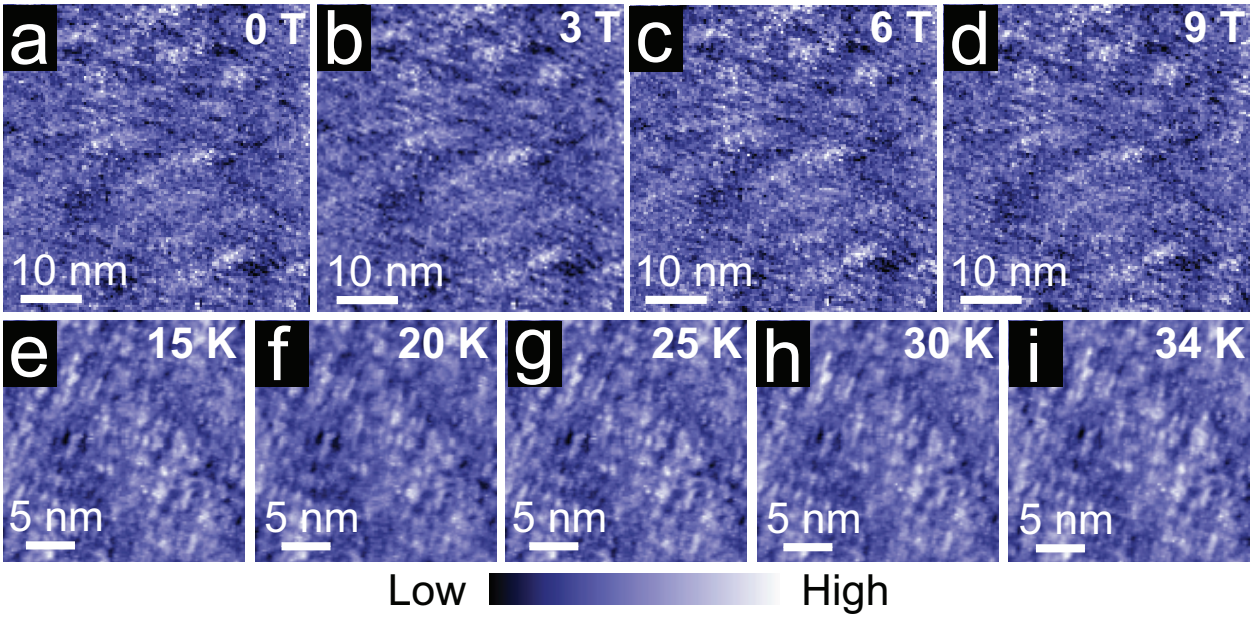

Figure 6.3.1: (a-d) STM topographs acquired over the same region of the sample at 7 K and 0, 3, 6, and 9 T magnetic fields respectively. (e-i) STM topographs acquired over the same square region of the sample at 0 T magnetic field and 15 K, 20 K, 25 K, 30 K, and 34 K respectively.

Ca-YBCO crystals indeed cleave at the Y/Ca layer (see crystal structure in Fig. 1.2.3d).

6.3 Spectral Gap Dependence

Typical spectroscopic measurements on the surface shown in Fig. 6.2.1b consistently show a gap in the density of states. To determine the nature of this gap, we investigate its dependence on temperature and the applied magnetic field. In order to show the ability to track the same area of the sample at different temperatures and magnetic fields, we show the regions of the sample where average dI/dV spectra have been obtained (Fig. 6.3.1).

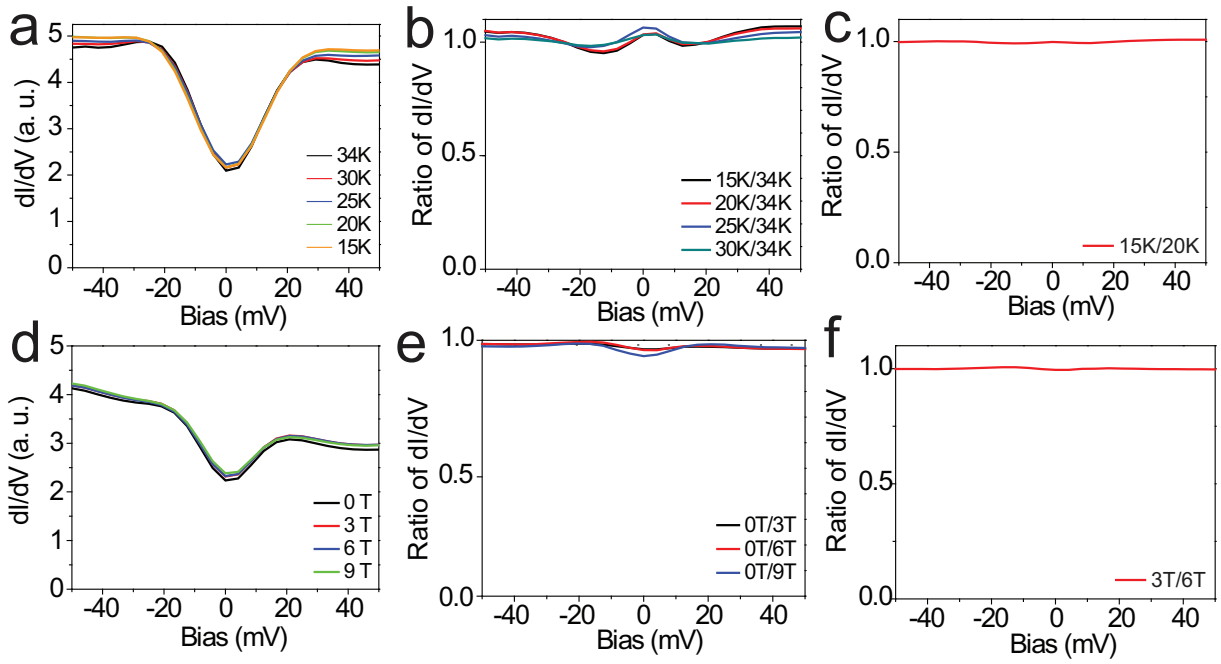

Figure 6.3.2: (a) Average dI/dV spectra from region in Figs. 6.3.1e-i at different temperatures, all thermally-broadened to 34 K. (b) Ratio of dI/dV spectra below T_c (15 K, 20 K, 25 K, and 30 K) and above T_c (34 K). (c) Division of average dI/dV spectra from (a) at temperatures of 15 K and 20 K showing less than 1% difference. (d) Average dI/dV spectra from a 50 nm square region in Figs. 6.3.1a-d at different magnetic fields. (e) Ratio of dI/dV spectrum at 0 T, and the ones acquired at 3 T, 6 T, and 9 T. (f) Ratio of average dI/dV spectra from (d) for 3 T and 6 T, exemplifying no difference in spectra to 1 %. Setup in (a,b,c): I_{set}=50 pA, V_{set}=-50 mV; (d,e,f): I_{set}=100 pA, V_{set}=-100 mV, 7 K.

6.3.1 The evolution of dI/dV spectra with temperature

Average dI/dV spectra acquired over the same 20 nm square region of the sample and thermally broadened to 34 K are shown in Fig. 6.3.2a. Thermal broadening represents convolution with the derivative of the Fermi function. This procedure accounts for the decrease in STM energy resolution at higher temperatures, and allows direct comparison of dI/dV curves obtained at different temperatures. The spectral gap observed is insensitive to the change in temperature from below to above T_c, which implies that the prominent gap observed is not of superconducting origin.

In a related cuprate Bi-2201, Boyer *et al.* have shown that the prominent gap observed by STM is also not of superconducting origin, but is actually the mysterious PG [53]. However, they were able to extract the hidden superconducting gap of $\sim 15\%$ by the division of dI/dV spectra acquired at different temperatures. In Ca-YBCO, the ratios of dI/dV spectra acquired below and above T_c (Figs. 6.3.2b-c) do not show a gap. We emphasize that the spectral division technique is very sensitive to subtle STM tip changes (even though average dI/dV spectra in Fig. 6.3.2a appear nearly identical), and confirm the lack of emergence of a superconducting gap by the division of dI/dV spectra at 15 K and 20 K, which shows no gap to less than 1% (Fig. 6.3.2c). Therefore we conclude that the spectral gap observed in Ca-YBCO using STM is not superconducting, although ARPES has been able to detect superconducting signatures in the same material [87]. We hypothesize that the contradiction stems from the difference in experimental techniques– ARPES might be able to probe deeper into the crystal compared to STM, which is likely only sensitive to a few atomic layers, far less than one bilayer unit cell. Therefore, we can conclude that the Ca-YBCO surface also suffers the overdoping catastrophe of non-Ca-doped YBCO samples, at least as far as STM studies are concerned.

6.3.2 The evolution of dI/dV spectra with magnetic field

To further confirm the origin of the spectral gap, we investigate its dependence on the applied magnetic field. When a magnetic field is applied to a type-*I* superconductor, magnetic flux is expelled to a thin layer on the surface. In contrast, in type-*II* superconductors such as high-T_c superconductors, magnetic flux penetrates as quantized flux tubes called vortices.

Previous STM studies have imaged disordered vortex lattices in several cuprates, such as Bi-2212 [38, 93], and YBCO [90]. Vortices in these studies appear as regions of: (I) higher differential conductance in dI/dV maps near the Fermi level, or (II) lower differential conductance in dI/dV maps close to the spectral gap energy. In contrast to vortex imaging in these compounds, no vortices have been detected in Bi-2201 under the application of magnetic field using either of these methods [94]. However, simple division of average dI/dV spectra in and out of magnetic field revealed the opening of a gap, signaling the existence of superconductivity [94].

In ten approaches on two different samples, we have been unable to image the vortex lattice in Ca-YBCO. Fig. 6.3.2d shows average dI/dV spectra over the same region of the sample under the application of different magnetic fields which look qualitatively very similar. Furthermore, the division of

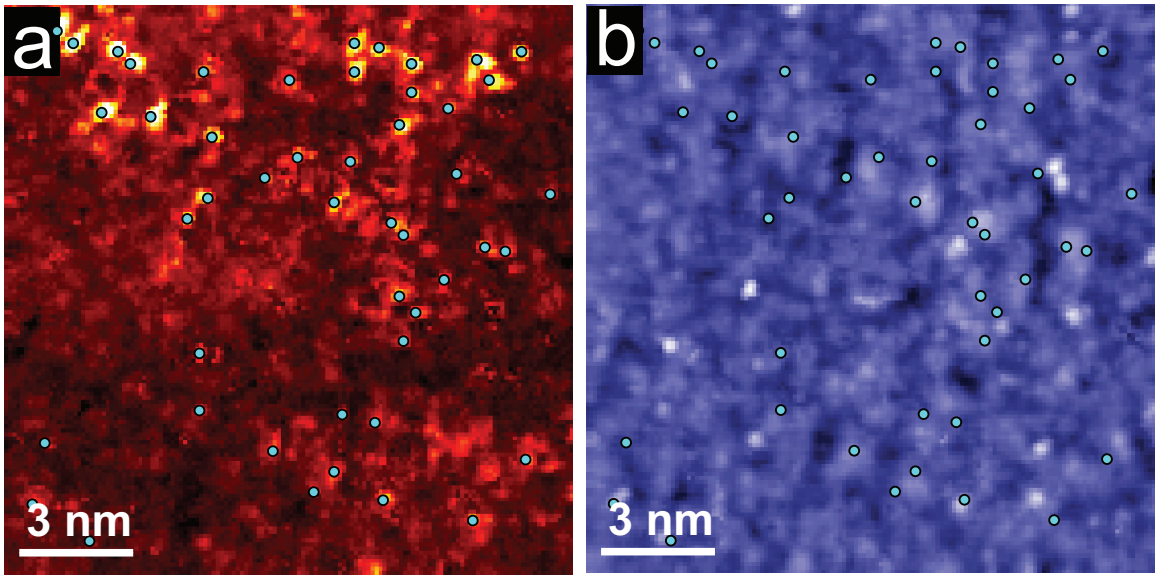

Figure 6.4.1: Dopant locations identified by the algorithm denoted as light-blue circles superimposed on top of (a) topograph and (b) integral of dI/dV from -9 mV to 9 mV. Setup: I_{set}=50 pA, V_{set}= -60 mV, and 7 K.

average dI/dV spectra at different magnetic fields confirm our previous conclusion (Figs. 6.3.2e-f), as the division of dI/dV spectra at 3 T and 6 T reveals no gap to less than 1%. This is another indication of suppression of superconductivity at the surface of Ca-YBCO.

6.4 Imaging of Resonances in the CuO Chain Plane

Having identified the prominent gap in dI/dV as the PG, we proceed to investigate a set of impurities revealed in dI/dV maps. Fig. 6.4.2a shows an integral of dI/dV from -9 mV to 9 mV, which was acquired simultaneously with the topograph shown in Fig. 6.2.1b and reveals a set of atomic-scale features as regions of high differential conductance. Using the dopant locator algorithm with DD=2.1 Å, NS=4.3 Å, and SW=16.7 Å (Appendix B.2) we count approximately 48 ± 7 resonances in the field-of-view (Fig. 6.4.1), which corresponds to a density of $\sim 3.2\% \pm 0.5\%$ per unit cell .

Let us compare this quantity to the expected number of O vacancies and Ca dopants in the crystal:

- **O vacancies.** The particular batch of samples we studied is determined to have ∼6.4 O atoms per unit cell (7 makes the crystal structure perfectly stoichiometric). Since O vacancies are thought to occur primarily in the CuO chain plane [95], 60% of all unit cells imaged would contain an O vacancy (or ∼900 of them should be detected in a 15 nm square region). The number of unknown features that we observe is one order of magnitude fewer. Thus, the observed resonances are unlikely to be O vacancies.

- **Ca dopants.** Based on energy-dispersive X-ray measurements, our samples contain ∼10% Ca substitutions at the Y sites. This density is a factor of 3 different from that of the unknown features we observe, which might suggest that these atomic-scale regions of high-conductance around Fermi level are Ca dopants.

Figs. 6.4.2b-c show a series of dI/dV spectra along a line starting at the center of one representative impurity outwards. These spectroscopic measurements reveal two bound states, symmetric around the Fermi level, that result in *negative differential conductance* at energies of $\sim \pm 30$ meV.

A series of dI/dV maps across different energies encompassing a single impurity are shown in Fig. 6.4.3. The observed spatial signature is C_2- but not C_4-symmetric, which allows us to pinpoint the location of these features to possibly be in the CuO chain plane, as it is the only layer that structurally breaks the C_4 symmetry. Since the density of these resonances is not consistent with the expected density of O vacancies as discussed earlier, we believe that Cu-site defects (likely Cu vacancies) in the CuO chain plane are the culprits behind the structural origin of these resonances.

Our identification is strengthened by similar spectroscopic signatures in dI/dV that originate as a consequence of Cu-site defects in other cuprates. In Bi-2212, Zn [96] and Ni [97] substitutions for Cu, as well as unknown features likely to be Cu vacancies [76, 98] induce bound states at the Fermi level and suppress gap-edge peaks. The fact that Zn substitutions and native defects, both presumed to be non-magnetic impurities directly in the crucial CuO_2 superconducting layer, showed strong sub-gap resonances gave strong support to the sign-changing d-wave superconducting order parameter. In Bi-2201, a set of intrinsic Cu-site defects (likely vacancies) induce two peaks symmetric around the Fermi level [99], qualitatively very similar to what we observe in Fig. 6.4.2c. Furthermore, since these features maintained their spectroscopic signature well above T_c, Chatterjee *et al.* concluded that the spatial and energy distribution of the impurity state is not determined by the superconducting gap, but rather by the

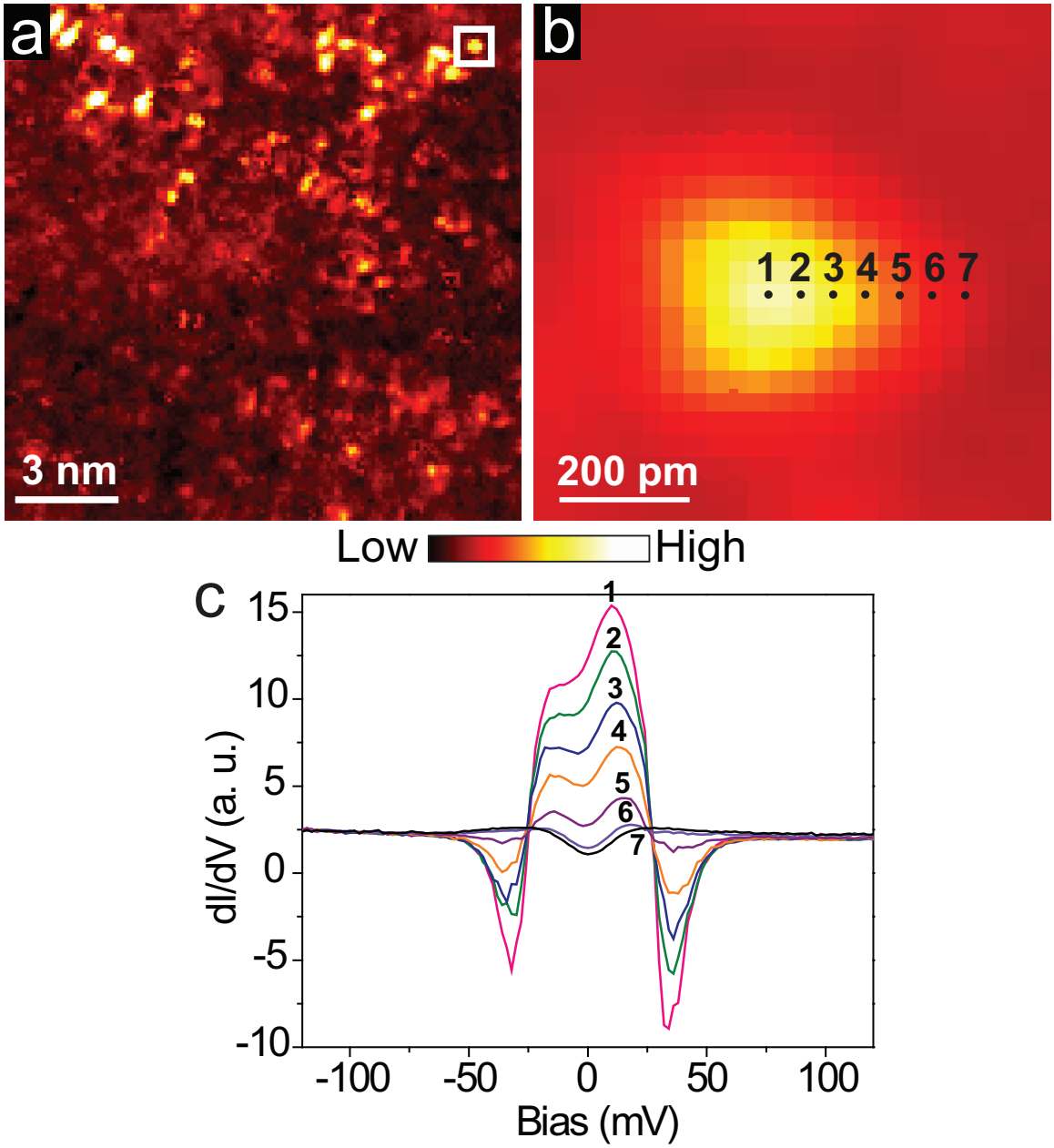

Figure 6.4.2: (a) Integral of dI/dV maps from -9 mV to +9 mV bias, simultaneously acquired with the topograph in Fig. 6.2.1b, showing a set of resonances as bright, atomic-scale features. (b) dI/dV(0 mV) map, zooming-in on a resonance denoted by white square in (a). (c) dI/dV spectra obtained at the positions denoted in (b), starting from the center of the impurity outwards. Setup in (a): I_{set}=500 pA and V_{set}= -60 mV; in (b,c): I_{set}=100 pA and V_{set}= -120 mV.

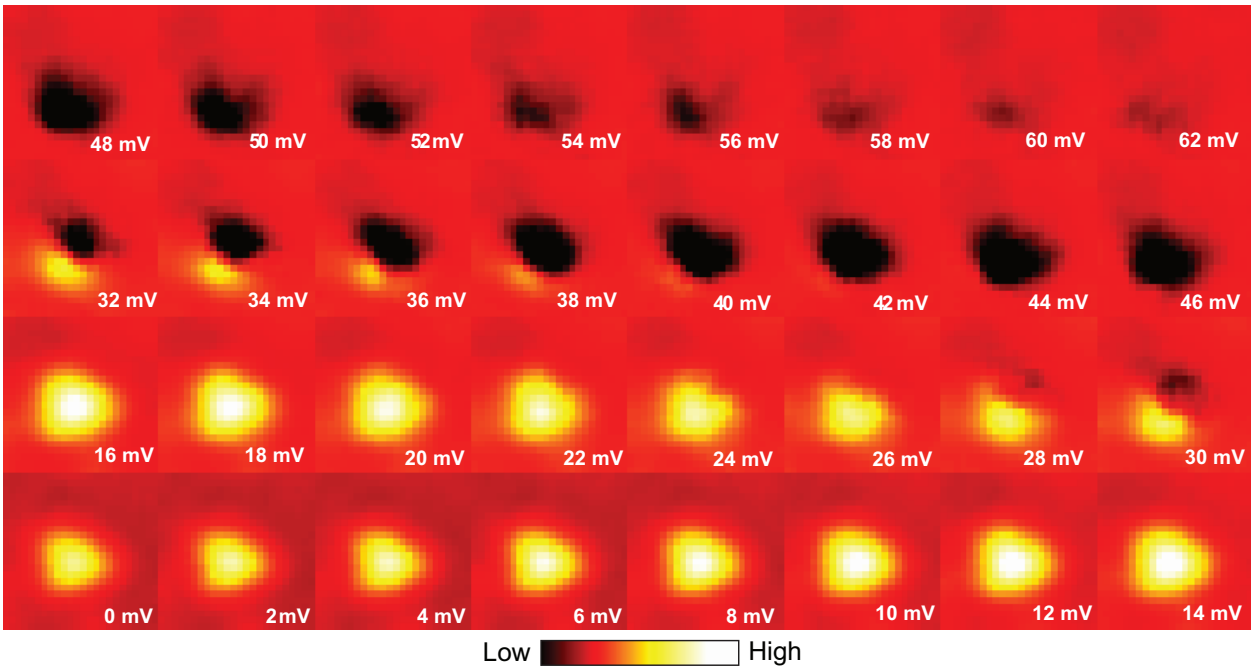

Figure 6.4.3: Series of dI/dV maps over a 800 pm square region with a single impurity at a bias ranging from 0 mV to 62 mV, showing C_4-symmetry breaking. This observation is consistent for several different impurities we closely investigated. Similar spatial dependence is observed at corresponding negative bias. Setup: I_{set}=100 pA and V_{set}= -120 mV.

pseudogap. As discussed in the previous section, the spectral gap we observe in Ca-YBCO is not of superconducting origin. Thus, our observation of impurity-induced bound states in this material provides additional support to the claim that these impurity states are not necessarily a signature of the superconducting state.

Many theoretical efforts have proposed different ways of extracting the strength of a potential scatterer based on the energy of an impurity-induced bound state [100]. We use the theoretical treatment by Salkola *et al.* used by other STM studies to extract the strength of the scatterer in terms of the phase shift δ_o [101]:

$$\Omega_o = c\Delta_o \frac{\pi/2}{\ln(8/(\pi c))} \tag{6.1}$$

where Ω_o is the resonance energy, Δ_o is the spectral gap magnitude, and $c = \cot(\delta_o)$. In our studies of Ca-YBCO, $\Omega_o \approx 10$ meV and $\Delta_o \approx 24$ meV, which allows us to determine the phase shift δ_o to be 0.36π. For direct comparison, δ_o is calculated to be 0.48π, 0.36π, and 0.48π for Zn dopants, Ni dopants and vacancies in Bi-2212 [96–98] and 0.40π for intrinsic defects in Bi-2201 [99]. In the strongest scattering (unitary) limit, $\delta_o = \pi/2$. Thus, the resonances we observed in Ca-YBCO are induced by strong, but not unitary scatterers.

6.5 Spectral Gap Inhomogeneity

In contrast to the consistent observation of spectral gap inhomogeneity in Bi-based cuprates, no such reports have been made in YBCO. To address this issue in Ca-YBCO samples, we acquire dI/dV spectra on a square, densely-spaced pixel grid, and calculate the magnitude of the gap at each point by fitting a Gaussian curve to the peak on the negative side of the spectrum. Fig. 6.5.1a shows a topograph, and Fig. 6.5.1b shows an inhomogeneous spectral gap map acquired simultaneously. The average gap value is 23.6 ± 3.2 meV, which represents $\sim 14\%$ variation within our FOV, comparable to $\sim 15\%$ variation we observe in optimally doped T_c=91 K Bi-2212 sample. Fig. 6.5.1c shows average dI/dV spectra binned by the magnitude of the gap. Azimuthally averaged autocorrelation of the gapmap in Fig. 6.5.1b shows a length scale of about 1-2 nm, which is slightly different from the gap maps of optimally-doped Bi-2212 with characteristic length scales of 2-3 nm (Fig. 6.5.1d). Cross-correlation coefficients between topograph and zero-bias conductance (ZBC), and topograph and the gap map are very weak (Fig. 6.5.1d),

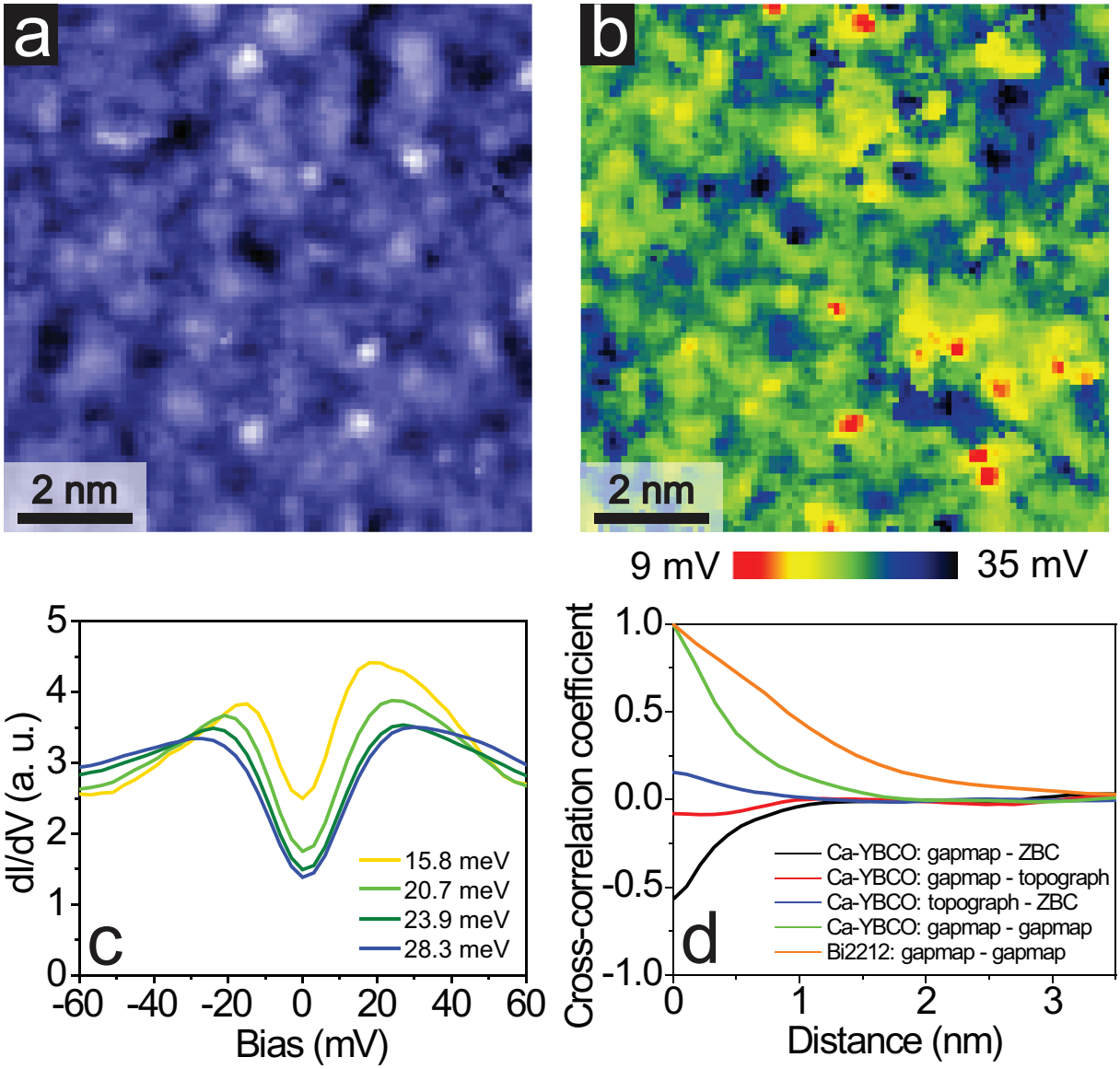

Figure 6.5.1: (a) Topograph and (b) spectral gap map acquired simultaneously over a ∼10 nm square region. (c) Average dI/dV spectra binned by the magnitude of the gap as determined by Gaussian fit to the negative side of the spectra. (d) Cross-correlation coefficients relating gapmap, ZBC, and topograph in Ca-YBCO (black, red and blue lines). Azimuthally averaged autocorrelation for Ca-YBCO with T_c=30 K and optimally-doped Bi-2212 with T_c=91 K are shown in green and orange respectively. Setup: I_{set}=50 pA, V_{set}=-60 mV, 7 K.

suggesting that the spatial distribution of the spectral gap and ZBC is not related to the surface disorder. We also map the spatial distribution of the energy of the NDC minimum (Fig. 6.5.2c) and the bound-state peak in the vicinity of a single impurity above Fermi level (Fig. 6.5.2d). Both show C_2- but not C_4-symmetric signatures.

6.6 Conclusion and Discussion

In summary, our detailed STM studies of Ca-YBCO have addressed several important issues. First, STM topographs confirm the hypothesis that Ca doping results in an alternative cleavage plane in YBCO distinct from previously known BaO or CuO surface terminations, likely to be the disordered Y/Ca layer. Second, based on insensitivity to temperature and magnetic field, the dominant spectral gap in dI/dV is not the superconducting gap. We also observe a set of impurity-induced resonances that break C_4 symmetry we attribute to Cu-site vacancies in the CuO chain plane. This observation provides further evidence that the impurity-induced bound states near the Fermi level are not necessarily a signature of the superconducting state, and that any depletion of states near the Fermi level would allow a resonance-like bound state near a non-magnetic impurity, as theory had predicted [102]. Finally, we have for the first time observed nanoscale inhomogeneity in the spectral gap on the surface of YBCO, with characteristic length scales of 1-2 nm, which is slightly shorter compared to the optimally-doped Bi-2212 samples.

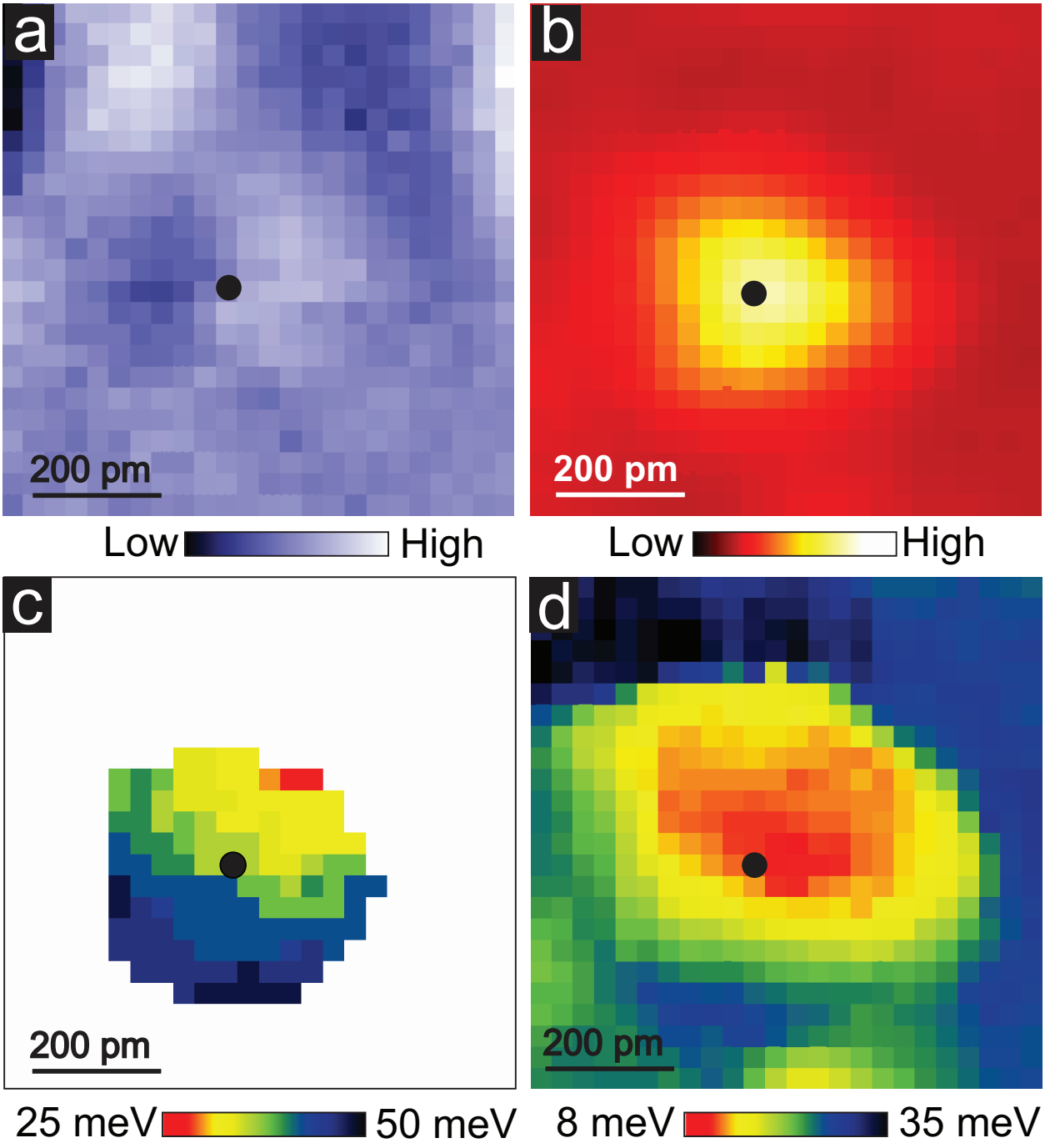

Figure 6.5.2: Simultaneous (a) topograph and (b) integral of dI/dV from -8 mV to +8 mV showing one impurity. Energy of the (c) NDC minima, and (d) the bound-state peak on the positive side of the dI/dV spectrum. Setup: I_{set}=100 pA and V_{set}= -120 mV.

7

Surface Element Identification and Dopant Homogeneity in $Pr_xCa_{1-x}Fe_2As_2$

In this chapter, we will show (I) the first definitive identification of the cleaved surface termination and (II) the first image of all individual dopants in any $CaFe_2As_2$ system which suggests that dopant inhomogeneity is unlikely to be responsible for the low volume fraction of high-T_c superconductivity in $Pr_xCa_{1-x}Fe_2As_2$.

7.1 Identification of Surface Chemical Composition

7.1.1 Surface controversy in AFe_2As_2 family of Fe-based superconductors

Like cuprates, Fe-based superconductors (Fe-SCs) are layered, with Fe-based superconducting planes separated by buffer layers. However, in contrast to those of cuprates, the nature of the cleavage surfaces in

many Fe-SCs has been difficult to pin down. Furthermore, surface cleanliness, flatness, and charge neutrality are all necessary, but not sufficient conditions to conclude that the surface is representative of intrinsic bulk properties of a material– surface can have different carrier concentration compared to the bulk, or it may exhibit structural or electronic reconstructions. Therefore, the first challenge in STM imaging of any new class of materials is to identify the surface structure and evaluate to what extent it is representative of the bulk.

The surface structure of the $A\mathrm{Fe_2As_2}$ system has been particularly controversial [50]. Due to the stronger bonding within the FeAs layer (Fig. 7.1.1a), the FeAs layer is expected to remain intact, leaving half a complete A layer on each surface [103]. However, a number of experiments have claimed that the cleaved surface is As-terminated in the Ba122 [104], Sr122 [105], and Ca122 [106] systems.

7.1.2 Typical STM topographs

We encounter three different surface morphologies in our STM topographs of $\mathrm{Pr}_x\mathrm{Ca}_{1-x}\mathrm{Fe_2As_2}$. The majority of the observed sample surface displays a 2×1 structure (Fig. 7.1.1b) frequently observed in other STM studies of 122 materials [107]. We occasionally observe a disordered, "web-like" structure (Fig. 7.1.1c), which smoothly merges with the 2×1 structure (Fig. 7.1.1d). The third type of surface, observed rarely, shows a 1×1 square lattice with ~ 4 Å periodicity (Fig. 7.1.1e).

7.1.3 Surface identification using local barrier height mapping

In order to identify these surfaces, we proceed to map the tunneling barrier height. The tunneling current I is expected to decay exponentially with the tip-sample separation z as

$$I \propto e^{-\sqrt{\frac{8m_e\Phi}{\hbar^2}}z}$$

where Φ is the local barrier height (LBH), approximately equal to the average of the tip and sample work functions [108] (see Section 2.2.4 for more details). However, the LBH is sensitive not only to the elemental composition of the tip, but also the geometric configuration of the tip's terminal atoms, and the tip-sample angle (which reduces the LBH by $\cos^2\theta$, where θ is the deviation between the sample surface perpendicular and the z direction of tip piezo motion [109]). Moreover, the LBH depends on the sample topograph through two opposing mechanisms. On the one hand, protruding atoms or clusters may

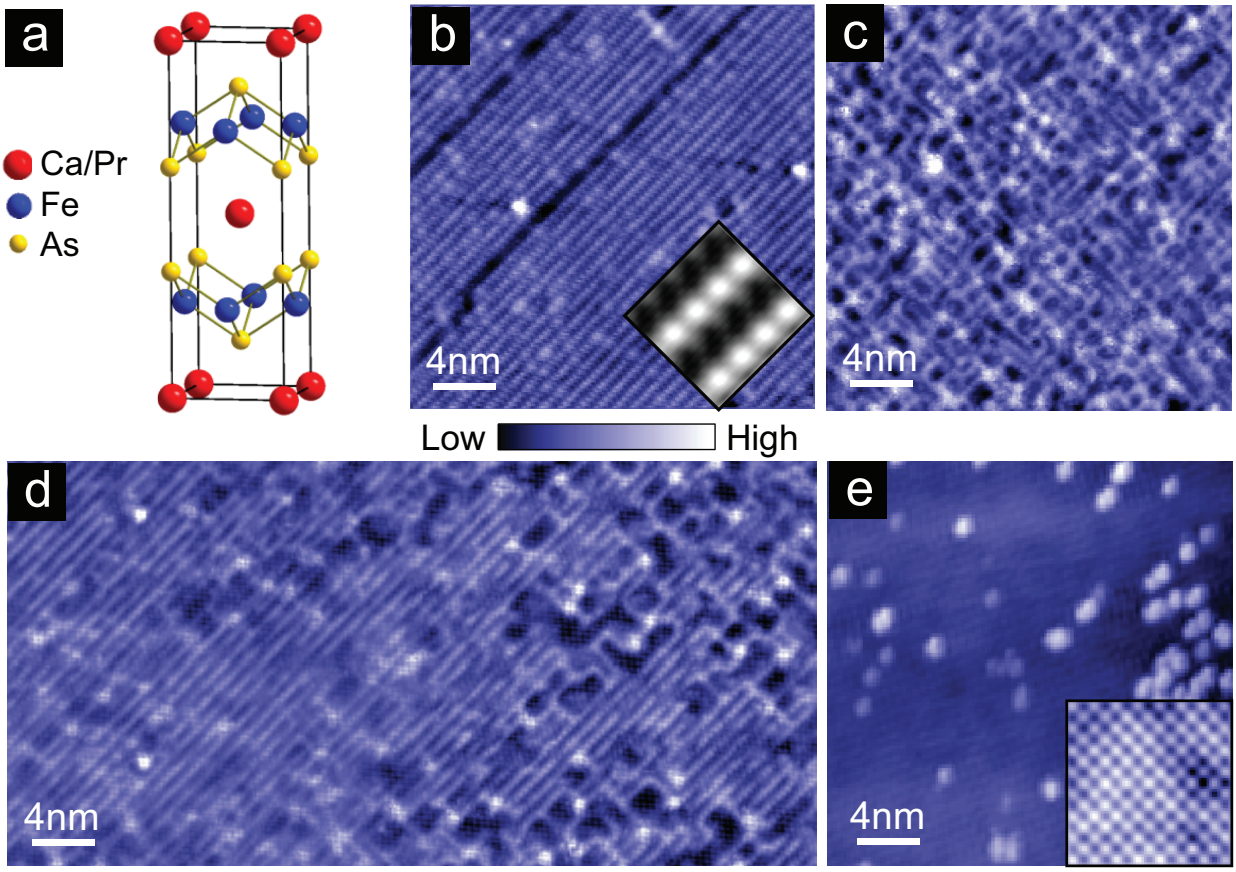

Figure 7.1.1: (a) Crystal structure of $Pr_xCa_{1-x}Fe_2As_2$. Topographs of (b) 2×1 surface structure (250 pA, +300 mV, 7 K) (c) disordered, "web-like" surface structure (15 pA, 100 mV, 7 K), (d) smooth transition between 2×1 and "web-like" structures (20pA, -100mV, 7K), and (e) 1×1 square lattice with ~ 4 Å lattice constant (5 pA, 50 mV, 25 K). Inset in (b) shows an average 30×15 pixel, 2×1 supercell tiled 2×4 times. Inset in (e) shows an enlarged, 4 nm topograph of 1×1 square lattice acquired at 50 mV and 50 pA. (Due to an external noise source present during the acquisition of the data in panel (e), the images in (e) have been filtered to remove all spurious spatial frequencies higher than the 4 Å periodicity.)

Table 7.1.1: Work functions for several elements[114].

Atom	Fe	As	Ca	Pr	Sr	Ba	Au	Pt	Ir
ϕ (eV)	4.65	3.75	2.71	2.7	2.76	2.35	5.32	5.40	5.6

stretch out as the tip is retracted, reducing the effective rate at which the tip-sample distance decreases, and thus suppressing the measured LBH above the protrusion [110]. On the other hand, the topographic corrugation appears smoothed out at distances far from the surface; this implies that the wave function decays faster above a protrusion than a depression, thus enhancing the measured LBH above a protrusion [111]. Without accounting for these factors, previous studies found the LBH on the 2×1 surface of $BaFe_2As_2$ to be much lower than the expected work functions for either Ba or As [112].

In contrast, the comparison of LBH measurements with the same tip (i.e. the same microscopic configuration of terminating atoms) across different flat regions of the same cleaved surface (i.e. the same tip-sample angle) can yield a robust measure of relative work functions, and can be utilized for element identification in cases where the sample consists of two different surfaces [113]. Here, we directly compare LBH values measured with the same STM tip across the different morphologies of Fig. 7.1.1 on the same cleaved sample.

Surface comparison of "2×1" *vs.* "1×1"

To extract the LBH at each point (x, y) in a field of view (FOV), a feedback loop first adjusts $z_o(x, y)$ to maintain $I = 100$ pA at $V_{set} = -100$ mV; the current $I(z)$ is then measured as the tip is retracted from z_o. Figure 7.1.2 shows simultaneous topographs and work function maps for the 1×1 square lattice across a step edge (Figs. 7.1.2a,c) and the 2×1 structure in a nearby flat area (Figs. 7.1.2b,d). Figure 7.1.2e shows two sets of representative $I(z)$ curves from the square regions in Figs. 7.1.2a-b, which are clearly distinct from one another. After correcting for the surface slope, the average LBH values is calculated to be $\Phi_{1\times1} = 4.50 \pm 0.42$ eV and $\Phi_{2\times1} = 3.57 \pm 0.34$ eV. Taking Table 7.1.1 and the tip work function into account, these values suggest that the 1×1 surface is a complete As layer, while the 2×1 surface is a half Ca layer.

We note that charge redistribution at a surface may give rise to an additional dipole barrier, which can

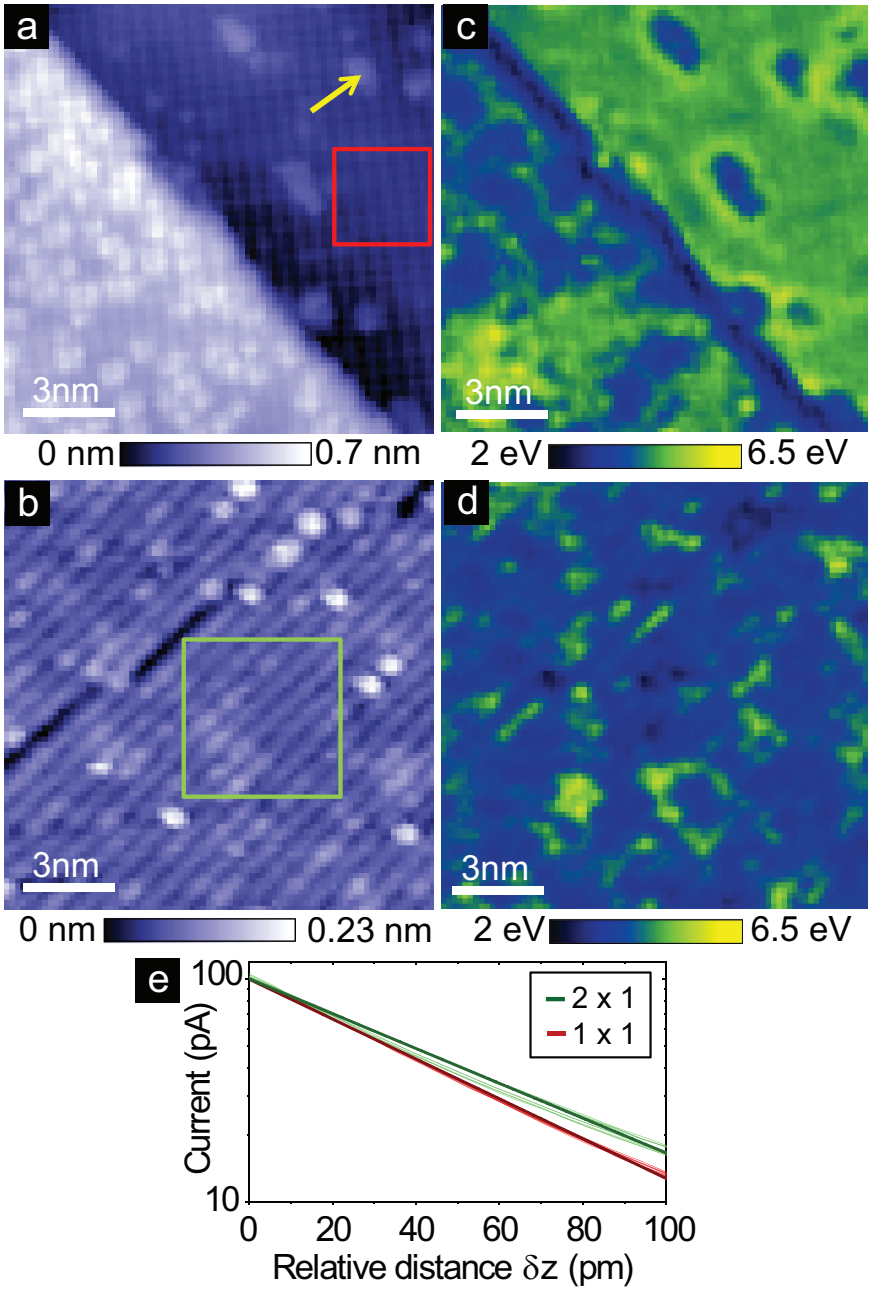

Figure 7.1.2: Topographs acquired at 25 K of (a) 1×1 (4 Å $\times$ 4 Å) square lattice appearing on both sides of a step edge and (b) 2×1 (8 Å $\times$ 4 Å) lattice. Simultaneously acquired LBH maps are shown in (c) and (d). Furthermore, sparse topographic protrusions on the 1×1 surface (e.g. marked by yellow arrow) show a lower LBH close to that of the flat 2×1 surface, suggesting that they are scattered remaining Ca or Pr atoms. Both datasets were acquired at I_{set}=100 pA and V_{set}=-100 mV. (e) Representative sets of $I(z)$ curves from square regions in (a) and (b) are shown as thin red and green lines respectively. Darker red and green lines represent linear fits to the average $I(z)$ curves from boxes in (a) and (b).

increase or decrease the measured LBH according to the dipole orientation [115]. We would therefore expect

$$\Phi_{1\times1} = \frac{\phi_{As} + E^{dip}_{As} + \phi_{tip}}{2};\ \Phi_{2\times1} = \frac{\phi_{Ca} + E^{dip}_{Ca} + \phi_{tip}}{2}$$

where ϕ_{As} and ϕ_{Ca} are the element work functions, and E^{dip}_{As} and E^{dip}_{Ca} are the additional energies for an electron to escape the dipole layers at the As- and Ca-terminated surfaces. Assuming $\phi_{tip} \lesssim \phi_{PtIr}$, the values of E^{dip}_{As}, E^{dip}_{Ca}, and their difference $E^{dip}_{As} - E^{dip}_{Ca} = 0.82$ eV are all of the correct magnitude for such dipole layers[115]. The sign of the difference, which indicates that it is harder to remove an electron from the dipole barrier of the As surface than that of the half-Ca surface, is physically justified because the half-Ca surface is nonpolar, whereas the As surface is deficient of electrons from the stripped Ca, and thus more electronegative. The inferred electron-deficiency of this As surface is consistent with the failure to observe even proximity-induced superconductivity on the As-terminated surface of the related $Sr_{0.75}K_{0.25}Fe_2As_2$ [116].

We also note the reduced LBH along the step edge in Fig. 7.1.2c, which may be attributed to two mechanisms [113]. First, the step edge is effectively an angled surface, so the LBH is reduced by $\cos^2\theta$. Second, the Smoluchowski smoothing of the electron wave functions along the step edge results in an additional dipole moment which reduces the LBH [117].

To further support the identification of the 2×1 surface, we show a high-resolution map of the intra-unit cell structure to rule out the possibility of "hidden" surface atoms. We correct for small piezoelectric and thermal drift by placing the Ca/Pr atoms of Fig. 7.1.1b on a perfect lattice [43]. We then use the whole FOV to create the average 2×1 supercell in the inset to Fig. 7.1.1b. We do not observe atom dimerization (as seen in $Ca_{0.83}La_{0.17}Fe_2As_2$ [106] and $Sr_{1-x}K_xFe_2As_2$ [105, 118]), but rather a single row of atoms, similar to the $CaFe_2As_2$ parent compound [119].

Surface comparison of "web-like" *vs.* "2×1"

For completeness, we investigate the nature of the "web-like" surface. Because it merges smoothly into the 2×1 surface without any evident step edges (Fig. 7.1.1d), it is also likely a reconstruction of the Ca layer. Simultaneous topograph and LBH map of the "web-like" surface are shown in Figs. 7.1.3a,c, with analogous maps for the 2×1 surface, acquired with the same tip for direct comparison, shown in Figs. 7.1.3b,d. Bright spots in the topograph of Fig. 7.1.3a exhibit anomalously high LBH, highlighting the

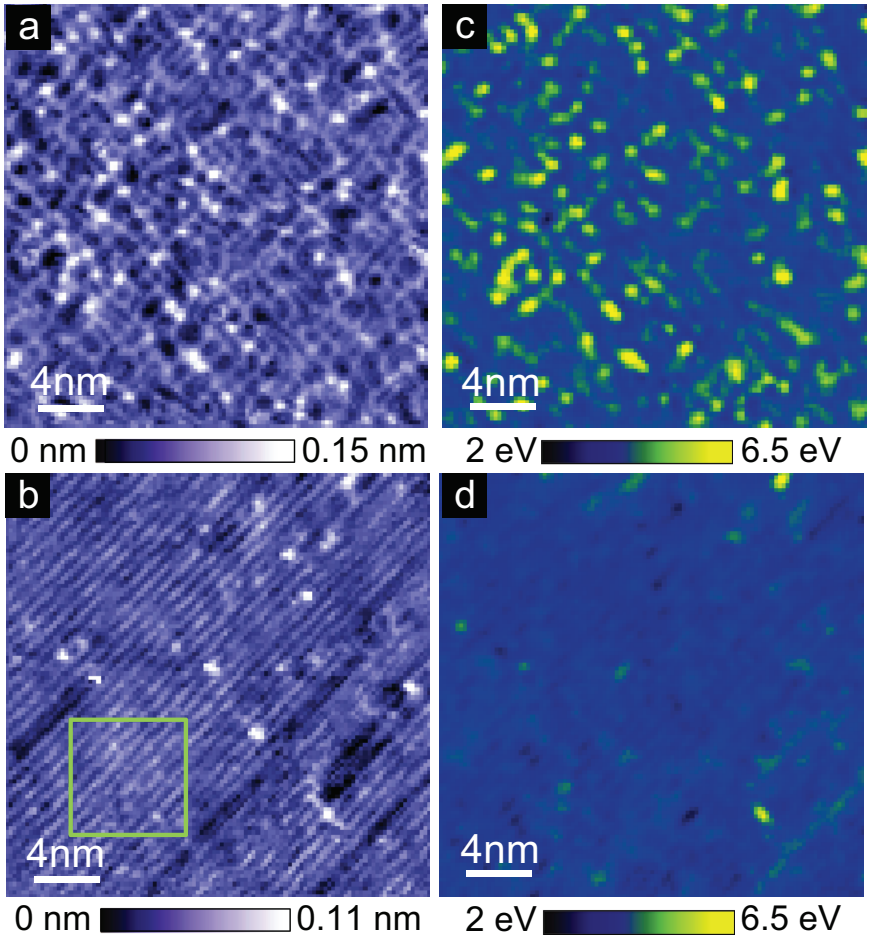

Figure 7.1.3: Topographs acquired at 7 K of (a) "web-like" surface and (b) 2×1 surface. Simultaneously acquired LBH maps are shown in (c) and (d). Both datasets were acquired at I_{set}=105 pA and V_{set}=-100 mV. The z calibration used here was obtained by assuming that the average LBH for the 2×1 surface in the boxed region of (b) here is the same as that in Fig. 7.1.2(d).

importance of the complex geometric effects of protrusions previously mentioned. This reinforces the necessity of flat atomic planes in order to extract a reliable LBH comparison. We reiterate that our identification of the 1×1 surface as a complete As layer and the 2×1 surface as a half-Ca layer is robustly drawn from the flat surfaces in Fig. 7.1.2.

7.2 Dopant Homogeneity in $Pr_xCa_{1-x}Fe_2As_2$

7.2.1 Rare-earth doped AFe_2As_2 family of Fe-based superconductors

In the first generation of AFe_2As_2 ($A122$) Fe-SCs, hole doping resulted in higher maximum T_c (38 K in $K_xBa_{1-x}Fe_2As_2$ [120]) than electron doping (25 K in $Ba(Fe_{1-x}Co_x)_2As_2$ [121]). However, the highest T_c among all Fe-SCs was 57 K in electron-doped $Sm_{1-x}La_xO_{1-y}F_yFeAs$ [26], prompting the suggestion that T_c could be enhanced in electron-doped $A122$'s by removing the damaging dopant disorder from the crucial Fe layer, and doping the buffer layer instead. The strategy was successful in the rare-earth-doped Ca122 family [122, 123], with T_c reaching 49 K in $Pr_xCa_{1-x}Fe_2As_2$. However, the high T_c appeared in only $\sim 10\%$ of the volume, while the bulk of the material showed $T_c \sim 10 - 20$ K.

Saha *et al.* performed a thorough search for the origin of the low volume fraction high-T_c phase, using bulk experimental probes. First, the high T_c was found to be impervious to etching or oxidation, arguing against surface superconductivity. Second, high-T_c resistive transitions were never observed for dopant concentrations below those necessary to suppress the parent antiferromagnetic phase, arguing against random inclusions as the origin. Furthermore, no such contaminant phases were observed in over 20 samples examined by X-ray diffraction. Third, the high T_c was unaffected by the global structural collapse phase transition (the abrupt $\sim 10\%$ shrinkage of the c-axis lattice constant that occurs in the Ca122 family under external or chemical pressure), arguing against any relationship to the collapsed phase or to interfaces between collapsed and non-collapsed phases. In fact, aliovalently-doped $CaFe_2(As_{1-x}P_x)_2$ also shows the structural collapse but no high-T_c volume fraction [124]. Saha *et al.* therefore concluded that the charge doping is an essential ingredient to the high-T_c phase, and speculated that it has "a localized nature tied to the low percentage of rare earth substitution."

Given the challenges in identifying the origin of the low volume fraction high-T_c phase from bulk experiments, a local probe is naturally required. Here we use scanning tunneling microscopy (STM) to investigate dopant clustering as a possible source of electronic inhomogeneity in $Pr_xCa_{1-x}Fe_2As_2$. Single

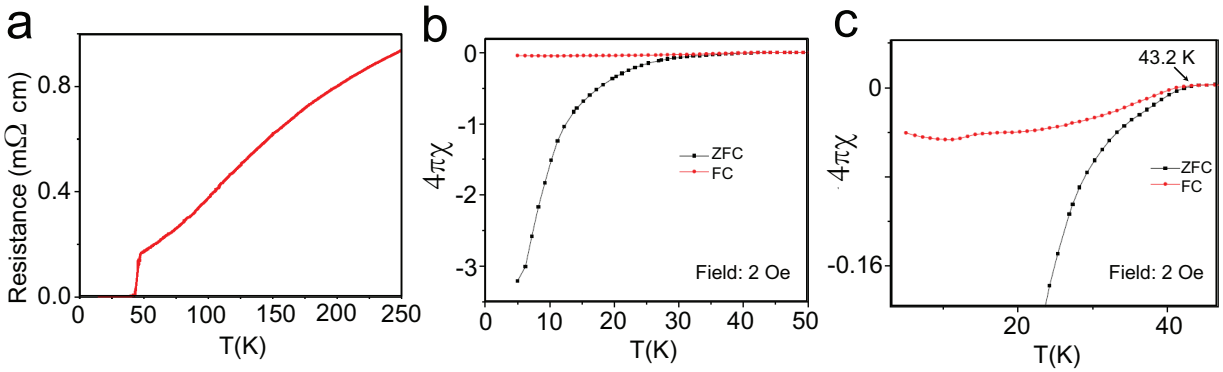

Figure 7.2.1: (a) Resistive measurements for the batch of $Pr_{0.105}Ca_{0.895}Fe_2As_2$ samples used in this study (b) Magnetic susceptibility measurements denoting the onset of superconductivity. (c) Zoom-in on the transition in (b) showing T_c=43.2 K onset.

crystals of $Pr_xCa_{1-x}Fe_2As_2$ are grown via self-flux with measured $x = 10.5\%$ and $T_c = 43.2$ K (Fig. 7.2.1). The crystals are handled exclusively in Ar environment, and cleaved in ultra-high vacuum at cryogenic temperature.

7.2.2 Dopant identification and lack of dopant clustering

Since ϕ_{Ca} and ϕ_{Pr} differ by less than 1% (Table 7.1.1), LBH mapping cannot be used to identify Pr atoms in the Ca surface layer. However, STM can image dopants using the differential conductance dI/dV, which is proportional to the local density of states. Substituting Pr^{3+} for Ca^{2+} creates a localized positive charge, so the impurity state is expected above the Fermi level. We therefore search for Pr dopants in dI/dV images at high bias. Figure 7.2.2a shows a dI/dV image obtained simultaneously with the topograph in Fig. 7.1.1b at +300 mV, revealing a set of bright, atomic-scale features. These features, which start to appear in dI/dV at biases higher than +70 mV, comprise ~10.4% of the total number of visible atoms in this FOV (Appendix B.2), matching the macroscopically measured $x = 10.5\%$ and confirming the half-Ca termination. Although a subset of Co dopants were previously imaged in $Ca(Fe_{1-x}Co_x)_2As_2$ [119], this is the first time that *all* dopants have been imaged in a Ca122 system.

Because we have imaged *all* dopants, we can investigate the possibility of clustering, which was suggested as the origin of the inhomogeneous high-T_c phase [122]. We compute a "radial distribution

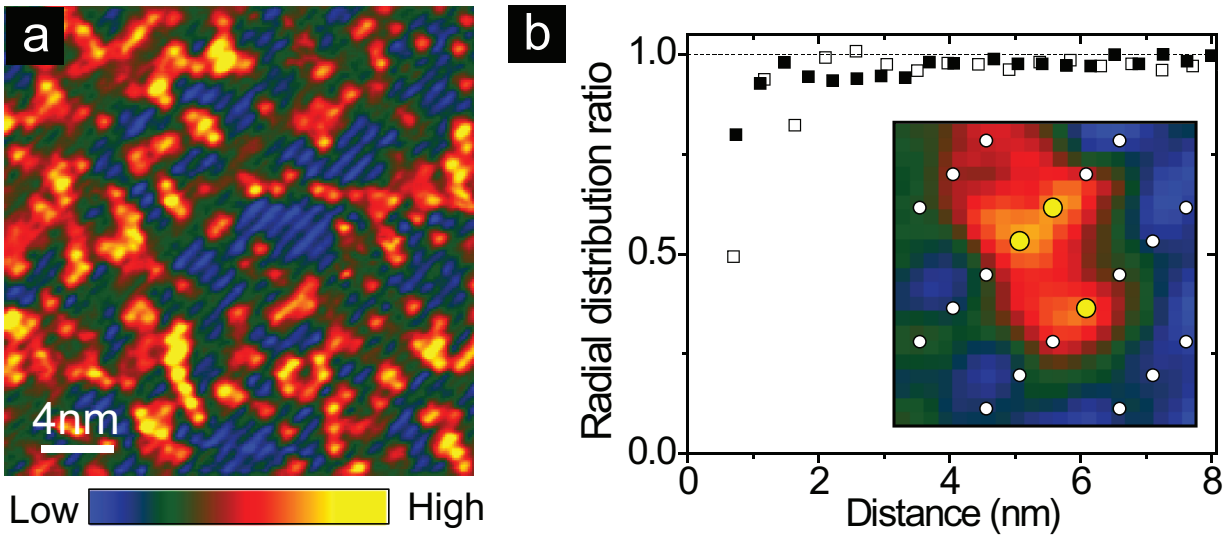

Figure 7.2.2: (a) dI/dV image at +300 mV showing Pr dopants as bright atomic-scale features from the same FOV as Fig. 7.1.1(b). (b) Radial distribution ratios for two sets of Pr dopants. Full squares represent the distribution of Pr dopants shown in (a), while open squares represent a different dataset used to confirm the conclusions. Inset shows a 2.5 nm × 2.5 nm region in which surface Ca positions (white dots) and Pr dopants (yellow dots) have been marked, demonstrating our ability to resolve individual Pr dopants even at adjacent Ca sites.

ratio" (RDR) by histogramming all observed Pr-Pr distances within a FOV, then dividing this observed histogram by an average histogram of 1000 simulated random dopant distributions at the same concentration. The RDR in Fig. 7.2.2b shows no clustering, and in fact slight repulsion of the Pr dopants at short distances, possibly due to their like charges. The repulsion is not an artifact of poor dopant identification, as illustrated by clear detection of two adjacent Pr dopants in the inset to Fig. 7.2.2b. The lack of dopant clustering in $Pr_xCa_{1-x}Fe_2As_2$ contrasts with the Se dopants in $FeTe_{1-x}Se_x$ that are prone to forming patches of ∼1 nm size [51]. This contrast may arise from the ∼10% size mismatch of Se (198 pm) and Te (221 pm) vs. the similar sizes of Ca (126 pm) and Pr (126.6 pm) [116, 125]. Our observation of the expected number of Pr dopants, more homogeneously distributed than would be expected for a random distribution, suggests that dopant clustering is unlikely to be responsible for the small volume fraction high-T_c superconducting state.

7.3 Conclusion and Discussion

In conclusion, STM images of $Pr_xCa_{1-x}Fe_2As_2$ have addressed its surface structure and dopant distribution, with bearing on its high-T_c volume fraction. First, we used LBH mapping to identify the 2×1 surface as a half-Ca termination, and the 1×1 surface as an As termination. This LBH mapping method could be used to resolve debated cleaved surface terminations in a wide variety of materials, such as other Fe-SCs [126] or heavy fermion materials [127, 128]. Second, we demonstrated by direct imaging that the Pr dopants responsible for superconductivity do not cluster, and in fact show a slight repulsion at very short length scales. The findings suggest that Pr inhomogeneity is unlikely to be the source of the high-T_c volume fraction, in contrast to previous speculation [122].

A

Appendix

A.1 Drift-correction Algorithm Details

In this section I will describe the algorithm, first implemented by Lawler *et al.* [43], used to correct the small thermal and piezoelectric drift present during the course of data acquisition (typically several hours to 2-3 days). Typical topographs of Bi-2212 show several different modulations: atomic Bragg wave vectors Q_x and Q_y, and supermodulation structural buckling with wave vector Q_{SM}. This idealized lattice structure is distorted due to thermal and piezoelectric drift; we can represent this picoscale "displacement" of atoms as a slowly-varying field $u(\vec{r})$ such that atomic positions $\vec{r} - u(\vec{r})$ form a perfect square lattice with Bi/Cu atom at $\vec{d} = 0$. We can write idealized topograph as:

$$T(\vec{r}) = T_0[\cos(Q_x\dot{(}\vec{r} - u(\vec{r}))) + cos(Q_y\dot{(}\vec{r} - u(\vec{r}))) + T_{sup}\cos(Q_{SM}\dot{(}\vec{r} - u(\vec{r})))] \tag{A.1}$$

In order to extract the drift field $u(\vec{r})$, we can first assume that it is constant over length scale of $1/\Lambda$,

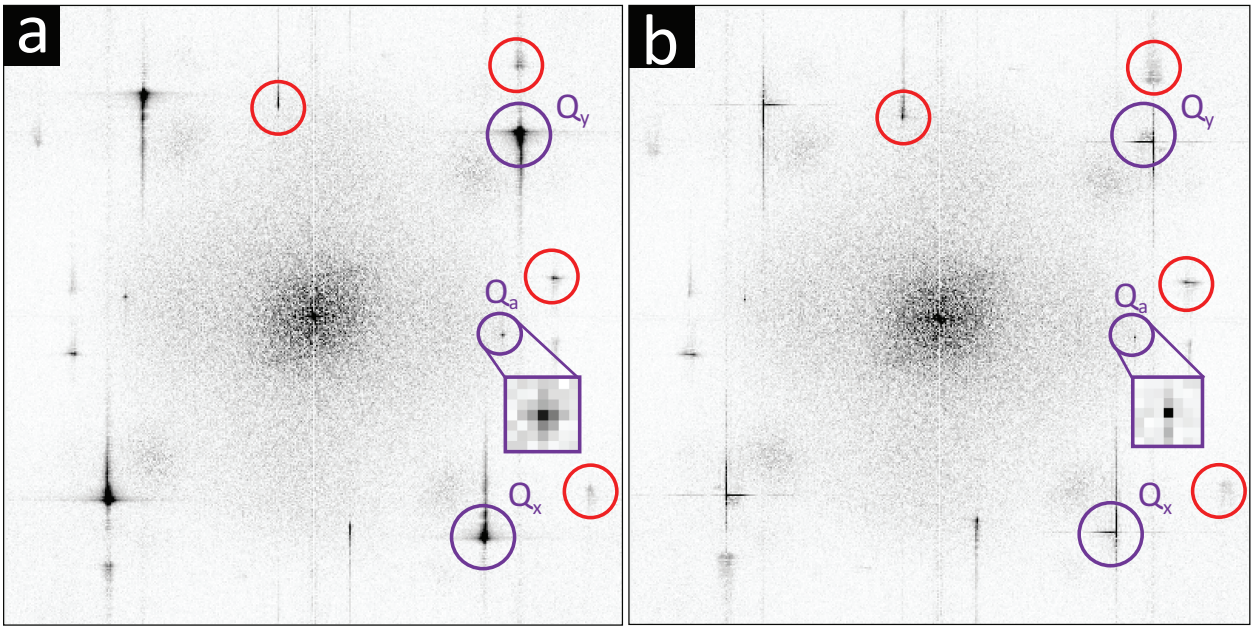

Figure A.1.1: Fourier transforms of STM topographs (a) before, and (b) after the application of drift-correction procedure. Atomic Bragg peaks Q_x and Q_y, and the orthorhombic peak Q_a that are blurred out in (a) are significantly sharper in (b).

where Λ is much smaller compared to magnitudes of Q_x, Q_y and Q_{SM}. Then, since atomic Bragg peaks are relatively sharp, we can simplify the expressions:

$$T_x(\vec{r}) = \sum_{\vec{r'}} T(\vec{r'}) e^{-\imath Q_x \vec{r'}} \left(\frac{\Lambda^2}{2\pi} e^{-\Lambda^2(\vec{r}-\vec{r'})^2/2}\right) \approx (T_o/2) e^{-\imath Q_x u(\vec{r})} \tag{A.2}$$

$$T_y(\vec{r}) = \sum_{\vec{r'}} T(\vec{r'}) e^{-\imath Q_y \vec{r'}} \left(\frac{\Lambda^2}{2\pi} e^{-\Lambda^2(\vec{r}-\vec{r'})^2/2}\right) \approx (T_o/2) e^{-\imath Q_y u(\vec{r})} \tag{A.3}$$

Using these two equations, we can extract the drift field $u(\vec{r})$. An example of a two dimensional Fourier transform before and after the process of drift-correction has been applied to the corresponding STM topograph can be seen in Fig. A.1.1. For more detailed description of the dependence of this algorithm on relevant parameters, see [48].

A.2 Details of Pseudogap *vs*. Dopants Correlations

A.2.1 Pseudogap determination

A number of different fitting techniques have been employed to extract the PG energy Δ_1 from raw STM spectra in previous studies [54, 129, 130]. However, without an accepted microscopic model for the PG, it is hard to justify the computationally intensive effort required for the use of any specific fitting function. We therefore use a simple, two part algorithm to extract the apparent PG energy Δ_1 from the positive bias conductance (empty states) between ε_F and +150 meV. For such spectra in which the global maximum in conductance lies between ε_F and +80 meV, this typically corresponds to a clear gap-edge peak, so we set Δ_1 equal to this energy. For spectra in which the global maximum in conductance occurs at energy greater than 80 meV, there is typically no clear gap-edge peak, so we instead set Δ_1 equal to the energy of the kink where the conductance slope abruptly flattens.

To demonstrate the reliability of this simple PG extraction algorithm, we focus on the most challenging sample, with T_c = 55 K, where we identify clear gap-edge peaks at $\Delta_1 \leqslant 80$ meV in only 55% of the spectra. From this sample, we show examples of typical spectra and their extracted Δ_1 in Fig. A.2.1. As a further demonstration, we bin all spectra by Δ_1, with bin size determined by the energy spacing at which the data was acquired. Fig. A.2.2 shows the complete set of spectra in each of 4 bins, exemplifying the quantitative spread but qualitative similarity of most spectra within each bin.

Because the slope-compare algorithm used for $\Delta_1 > 80$ meV is more sensitive to the noise level than the global maximum algorithm for $\Delta_1 \leqslant 80$ meV, we estimate the error of our Δ_1 extraction by repeating the same algorithm on increasingly smoothed data, and comparing results. Our final Δ_1 maps (shown in Fig. A.2.3) are determined from spectral surveys that have been smoothed with a 3 pixel boxcar average (corresponding to 0.48-0.69 nm, depending on the dataset, which is still far less than the superconducting coherence length $\varepsilon \sim$2.2 nm [93]). The pixel-by-pixel RMS differences between these Δ_1 maps and analogous Δ_1 maps from spectra surveys smoothed with 5 pixel boxcar average ($\sim$1 nm) are 12.1, 9.6, 4.9, and 2.7 meV from the T_c=55, 68, 82, and 91 K samples, respectively. In summary, we estimate that the PG extraction error is largest (up to $\sim$ 12 meV) in the T_c=55 K sample, and decreases to $<$ 3 meV in the T_c=91 K sample.

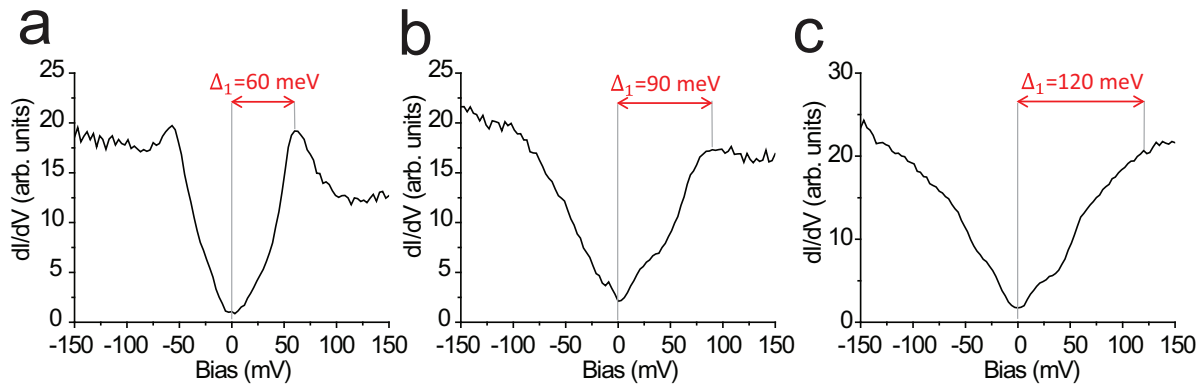

Figure A.2.1: (a) Δ_1=60 meV is obtained as the location of the global maximum on the positive side of the spectrum. (b-c) Δ_1=90 and Δ_1=120 meV are each obtained as the position of the first local maximum beyond 80 meV, which is typically an effective marker of the kink where the conductance slope flattens. All spectra have been 3 pixel boxcar averaged (9 spectra are averaged together, effectively smoothing on a 0.48 nm length scale). (Setup V_{sample}=-150 meV and I_{set}=800 pA.)

A.2.2 Crosscorrelation algorithm

To correlate the PG map $\Delta_1(\vec{r})$ with the locations of the dopants, one possibility would be to correlate it directly with the dI/dV map at the relevant energy. However, some dopants of the same type appear with slightly different size or brightness which might weight the cross-correlation unintentionally in favor of a subset of dopants. Instead, we create two-dimensional maps $D_A(\vec{r})$, $D_B(\vec{r})$, and $D_v(\vec{r})$ of the distance from the nearest type-A O, type-B O, and AOV, respectively. We compute the cross-correlation $C(\vec{R})$ between the PG map $\Delta_1(\vec{r})$ and each distance map $D(\vec{r})$ using the standard formula:

$$C(\vec{R}) = -\frac{\int [D(\vec{r}) - \bar{D}] \times [\Delta_1(\vec{r}+\vec{R}) - \bar{\Delta}_1] d^2r}{\sqrt{A_{D,D}(0) A_{\Delta,\Delta}(0)}} \tag{A.4}$$

$$A_{D,D}(\vec{R}) = \int [D(\vec{r}) - \bar{D}] \times [D(\vec{r}+\vec{R}) - \bar{D}] d^2r \tag{A.5}$$

A.2.3 Reproducibility of PG vs. O dopants correlations across different samples

Fig. A.2.4 shows large positive correlation between AOVs and the PG for the three underdoped samples. Type-A O dopants are correlated to a lesser extent, while type-B O dopants exhibit very weak correlation

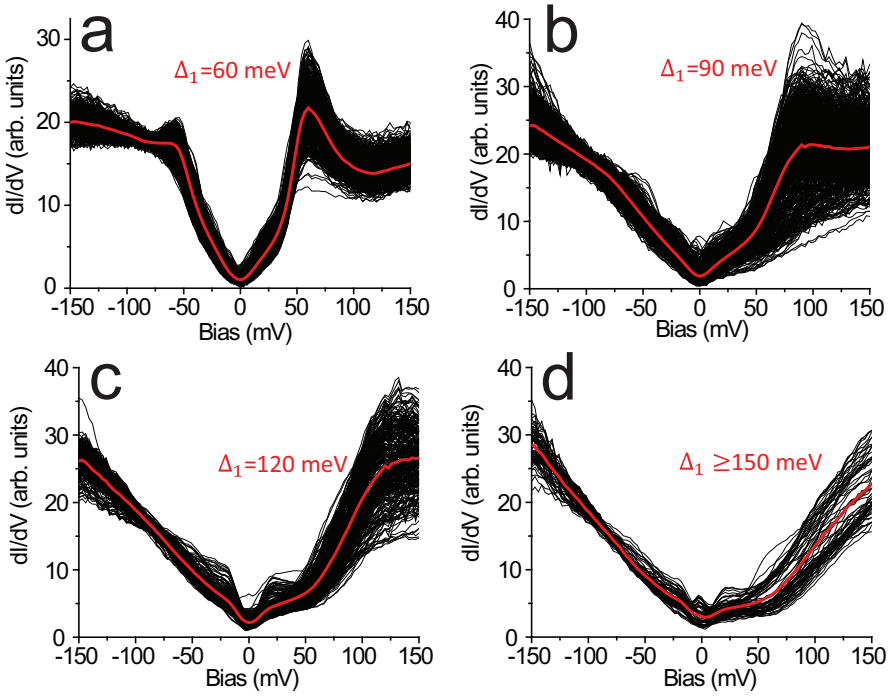

Figure A.2.2: Binned dI/dV spectra assigned a common Δ_1 of: (a) 60 meV, (b) 90 meV, (c) 120 meV, and (d) $\geqslant$ 150 meV. All black spectra have been 3 pixel boxcar averaged (9 spectra are averaged together, effectively smoothing on a 0.48 nm length scale). The bold, red curve in each panel represents the average of all the individual black spectra shown in that panel. (Setup V_{sample}=-150 meV and I_{set}=800 pA.)

with the PG. From the correlation length scales shown in Fig. A.2.4, we see that the AOVs influence the PG on a $\sim$2-3 nm length scale, and we speculate that they will also impact the superconducting state on this length scale. This is consistent with the PG map correlation length ε_{PG} $\sim$2-3 nm (Fig. A.2.3a inset), and with measurements of the superconducting coherence length $\varepsilon_{SC} = 2.2 \pm 0.3$ nm [93].

We also employ a second method to view the same information as in Fig. A.2.4. From a given distance map $\Delta(\vec{r})$, we bin the pixels based on their distance, then apply this binning to the corresponding PG map $\Delta_1(\vec{r})$, and compute the average gap within each distance bin. Fig. A.2.5 shows the average gap as a function of distance from the nearest impurity of each type.

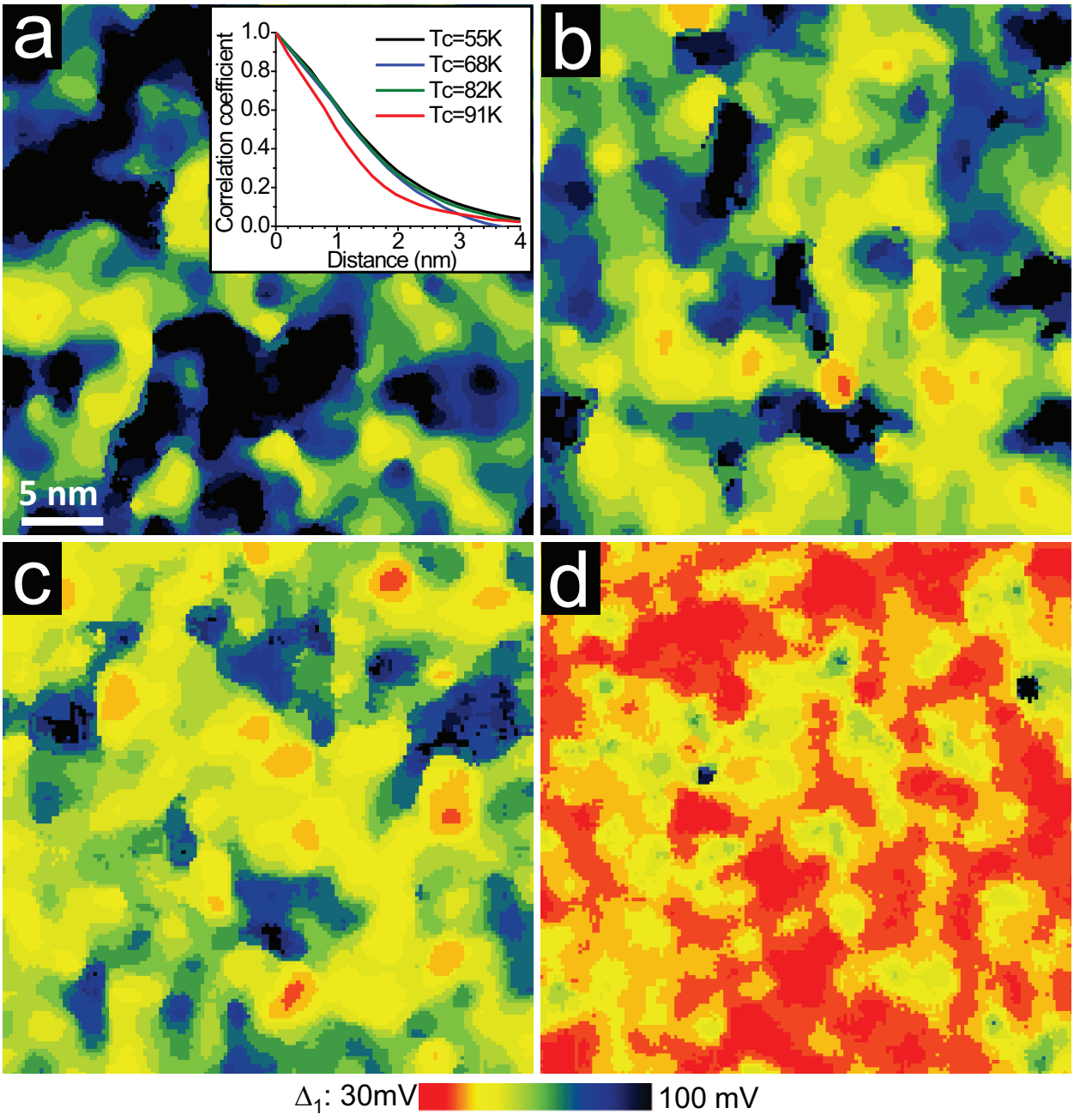

Figure A.2.3: Extracted Δ_1 map for (a) T_c=55 K, (b) T_c=68 K, (c) T_c=82 K, (d) T_c=91 K. All maps are 30 nm x 30 nm, and all are displayed using the same colorscale. Inset to (a) shows the azimuthally averaged autocorrelation of each gapmap, demonstrating a length scale ~2-3 nm. This justifies our initial smoothing of the spectral survey on the ~0.5-0.7 nm length scale, to reduce noise in each spectrum and ensure the reliability of the Δ_1 extraction algorithm.

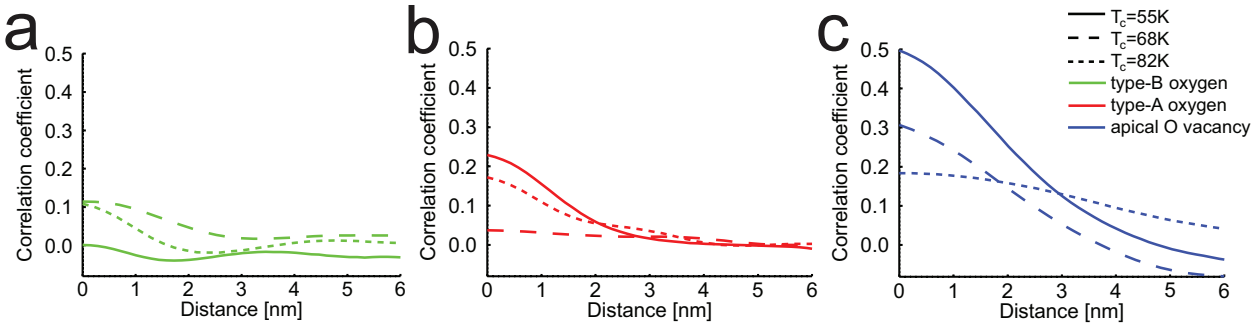

Figure A.2.4: Azimuthally averaged cross-correlation of the PG map Δ_1 and the map of distance to the nearest dopant $D(\vec{r})$ of (a) type-B O, (b) type-A O, and (c) AOV. Different curves within each panel represent data taken on different underdoped samples (solid: T_c=55 K, dashed: T_c=68 K, and dotted: T_c=82 K).

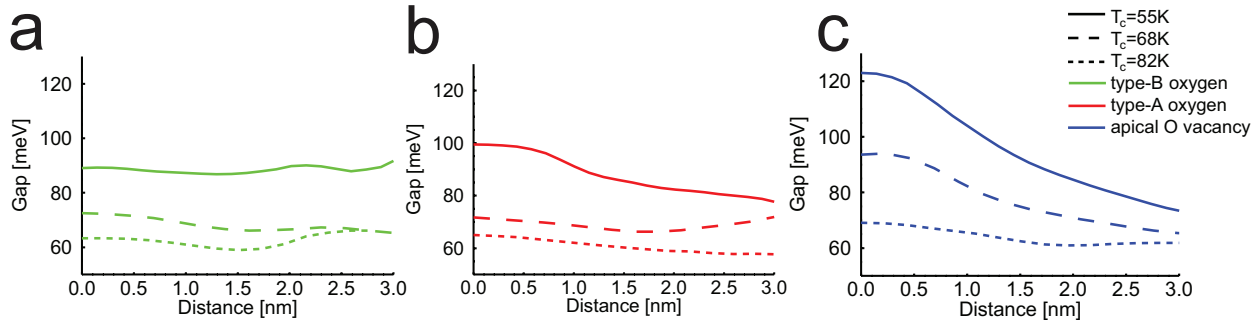

Figure A.2.5: Average PG as a function of distance from (a) type-B Os, (b) type-A Os, and (c) AOVs, respectively. Different curves within each panel represent data taken on different underdoped samples (solid: T_c=55 K, dashed: T_c=68 K, and dotted: T_c=82 K).

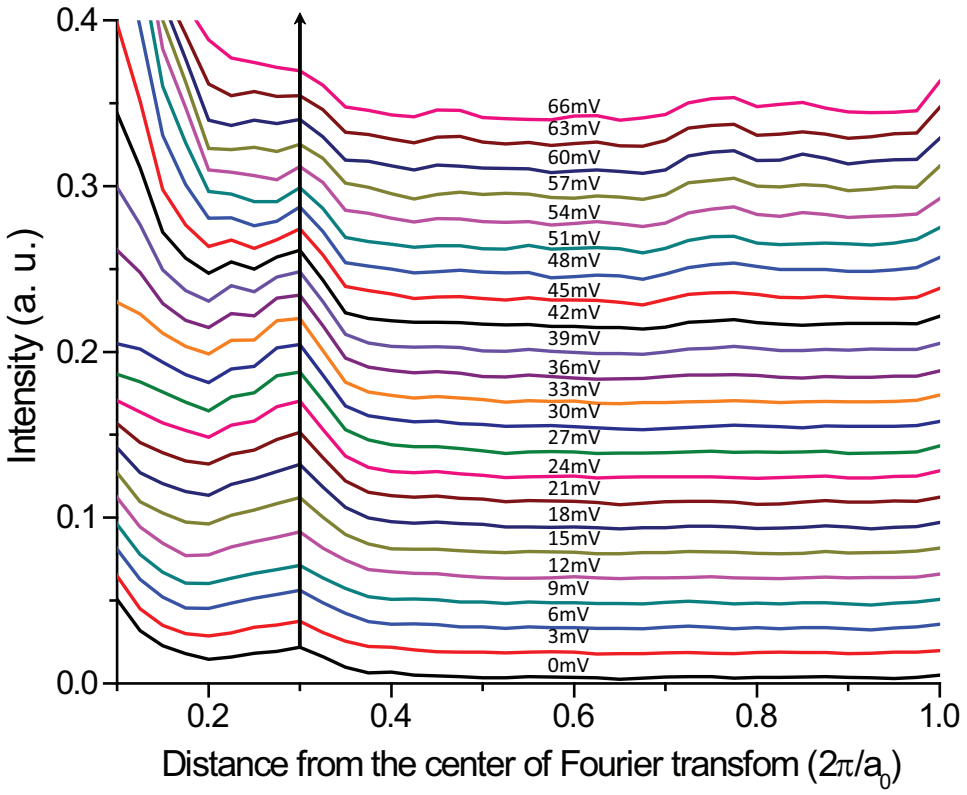

Figure A.3.1: Energy dependent linecut through the Fourier transform of dI/dV, along the Cu-O-Cu direction from $\vec{q}$=0 to the atomic Bragg peak, demonstrating the non-dispersing, incommensurate CB feature around $\vec{q}$ ~0.3. Data was acquired on the T_c=55 K sample, with setup V_{sample}=800 pA and I_{set}=-150 mV.

A.3 Details of "Checkerboard" *vs.* Dopants Correlations

A.3.1 Energy dependence of "checkerboard" wavevector

Utilizing two-dimensional Fourier transforms (FTs) of Bi-2212 dI/dV images from 0 mV to 66 mV, and extracting linecuts along the Cu-O-Cu direction, from the center of each FT to the atomic Bragg peak (Fig. A.3.1), it can be seen that the CB peak does not disperse with energy.

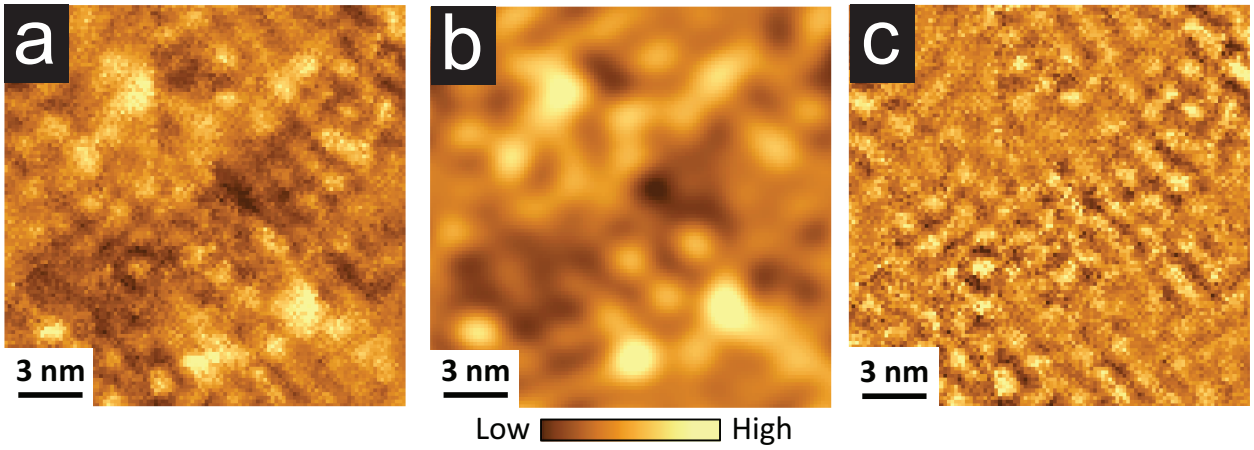

Figure A.3.2: (a) Raw dI/dV image from T_c=55 K, at energy +36 mV, with setup V_{sample}=-150 mV and I_{set}=800 pA. (b) Fourier-filtered image that contains only the wavevectors smaller than $2\pi/(10a_o)$. (c) Quotient: image (a) divided by image (b).

A.3.2 Determination of dopant positions with respect to "checkerboard"

In order to determine whether the dopants play a role in pinning the checkerboard, we first disentangle the long-range DOS variation (length scale $> 10a_o$) in the dI/dV maps from the checkerboard itself (typical wavelength $\lambda_c \sim 4a_o$), as demonstrated in Fig. A.3.2.

From the Fourier-filtered dI/dV image, it is easy to determine the centers of the 'checkers' (Fig. A.3.3a), and calculate the distance from each impurity to the center of the nearest 'checker' (Fig. A.3.3b). To produce Fig. 4.4.1b, I histogrammed the number of occurrences of each dopant type with respect to the distance d from the nearest 'checker', and normalized the count by the probability that any pixel would lie a distance d from a 'checker'. Because the CB does not disperse with energy, as shown in Fig. A.3.1, the analysis and conclusions about CB pinning are insensitive to the exact energy used for imaging the CB.

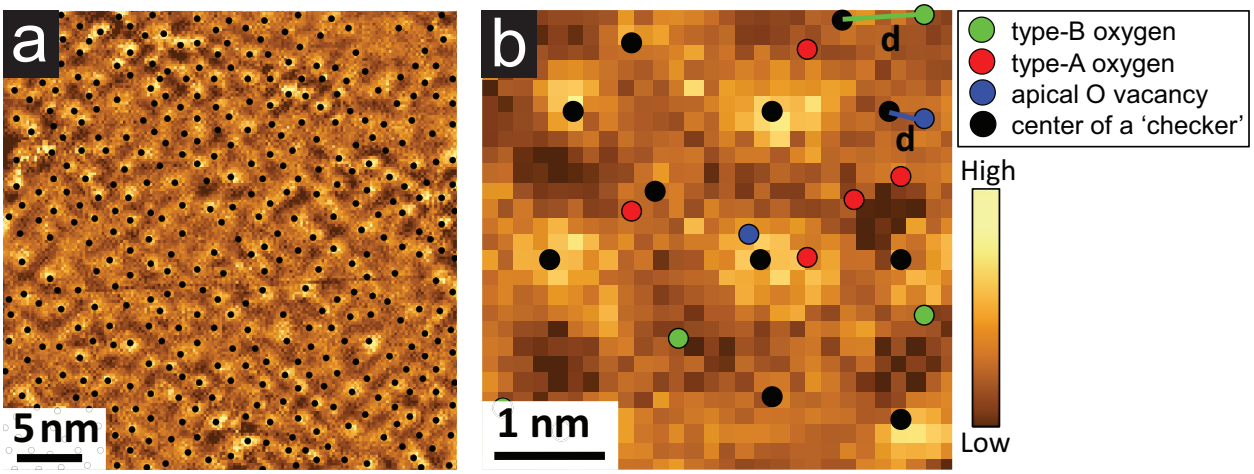

Figure A.3.3: (a) Fourier-filtered dI/dV image from T_c=55 K sample, at energy +35 mV, with setup V_{sample}=-150 mV and I_{set}=750 pA. The center of each peak is shown with a superimposed black circle. (b) Zoom on 4nm sub-FOV of the image in (a), exemplifying the distance of the dopants to the nearest CB peak.

B

Appendix

B.1 Dopant Distribution Algorithm

The algorithm used in Chapters 5 and 7 calculates how likely it is to have a dopant of one type (X) within a certain radius of another dopant of the same or different type (Y) compared to a completely random distribution of all dopants. More precisely, $N_i(r)$ is a number of dopants of type Y within a radius r of dopant X_i. We compute $N_i(r)$ for every X_i in the FOV and calculate the average $\bar{N}_o(r) = \frac{1}{n}\sum_{i=1}^{n} N_i(r)$, where n is the total number of dopants of type X. Then we repeat the process for 20,000 completely random distributions of both type X and type Y dopants to get $\bar{N}_j(r)$, where j takes values from 1 to 20,000. Finally, the value we plot on the y-axis in Fig. 5.5.1 is computed as:

$$\bar{N}_o(r)/(\frac{\sum_{j=1}^{20,000} \bar{N}_j(r)}{20,000}) \tag{B.1}$$

If the obtained ratio quotient is:

- > 1 then the dopants **attract** (prefer clustering)
- ~ 1 then the dopant distribution is **random**
- < 1 then the dopants **repel** and are even more homogenous than you would expect from a random distribution

B.2 Dopant Locator Algorithm

The dopant locator algorithm consists of four user-tunable parameters: neighborhood size (NS), duplicate distance (DD), smoothing window (SW), and local threshold (LT). For each pixel (x, y) in the field of view (FOV), the algorithm finds the position of the local maximum (LM) within a square of side NS centered at (x, y). From the set of LMs (x_i, y_i), the algorithm eliminates those within DD of a brighter LM, and those whose relative brightness compared to the regional average, defined as the average value within a square of side $2SW+1$ centered at (x_i, y_i), is less than LT.

To identify the dopants in Fig. 7.2.2, we used DD=2.4 Å (*cf.* Ca-Ca nearest-neighbor distance 4 Å), NS=4.8 Å, and SW=109 Å. Qualitative conclusions about the absence of clustering and short length scale repulsion of Pr dopants were unaffected by small errors in locating the centers of dopants (Fig. B.2.1(b)), and were robust up to 28% variation of SW (Fig. B.2.1(c)) and 15% variation of LT (Fig. B.2.1(d)).

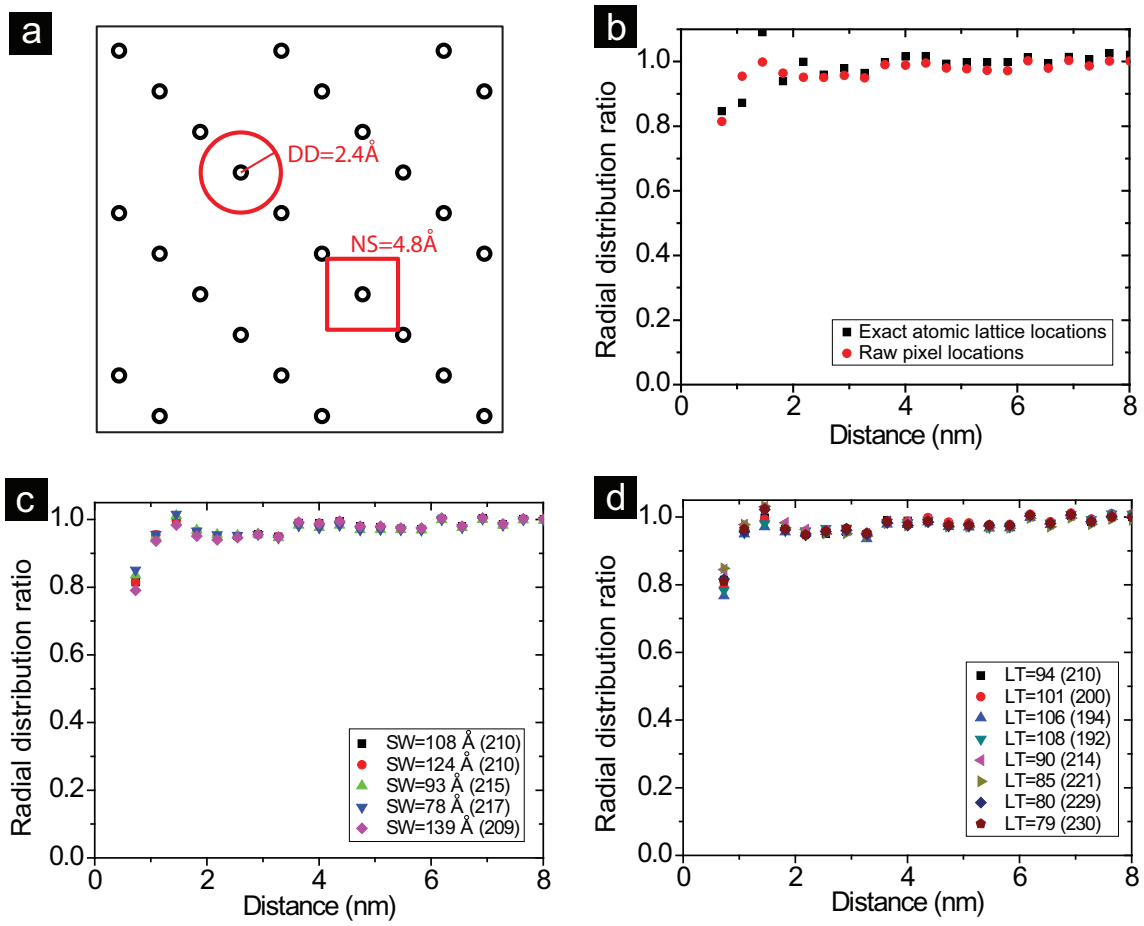

Figure B.2.1: (a) Schematic of a perfect 2 x 1 reconstruction, where the small black circles represent the locations of surface Ca/Pr atoms. The red circle and square denote the sizes of DD and NS parameters respectively. (b) RDR computed from the raw pixel positions of the dI/dV local maxima corresponding to Pr dopants (red squares). RDR computed using "corrected" Pr dopant positions (black squares). The "corrected" positions are calculated by taking the raw integer pixel positions obtained by the algorithm and "moving" them to the nearest ideal 2 x 1 lattice site, so that the new position is in fractional units of pixels. In other words, the raw pixel LM position was moved to the nearest exact atom position within a perfect 2 x 1 lattice. The impacts of varying (c) SW, and (d) LT parameters on the observed repulsion of Pr dopants. The numbers in parentheses show the number of Pr atoms found by the algorithm for each parameter set. LT is given in arbitrary units.

References

[1] Dirk van Delft and Peter Kes. The discovery of superconductivity. *Physics Today*, 63:38, 2010.

[2] W. Meissner and R. Ochsenfeld. Ein neuer effekt bei eintritt der supraleitfahigkeit. *Die Naturwissenschaften*, 21:787–788, 1933.

[3] J. Bardeen, L. N. Cooper, and J. R. Schrieffer. Theory of superconductivity. *Physical Review*, 108:1175–1204, 1957.

[4] W. McMillan. Transition temperature of strong-coupled superconductors. *Physical Review*, 167:331–344, 1968.

[5] J G Bednorz and K. A. Muller. Possible high T_c superconductivity in the Ba-La-Cu-O system. *Zeitschrift fur Physik B Condensed Matter*, 64:189–193, 1986.

[6] M. Wu, J. Ashburn, C. Torng, P. Hor, R. Meng, L. Gao, Z. Huang, Y. Wang, and C. Chu. Superconductivity at 93 K in a new mixed-phase Y-Ba-Cu-O compound system at ambient pressure. *Physical Review Letters*, 58:908–910, 1987.

[7] Philip Phillips. Colloquium: Identifying the propagating charge modes in doped mott insulators. *Reviews of Modern Physics*, 82:1719–1742, 2010.

[8] S Hüfner, M. A. Hossain, A. Damascelli, and G. A. Sawatzky. Two gaps make a high-temperature superconductor? *Reports on Progress in Physics*, 71:062501, 2008.

[9] V. J. Emery and S. A. Kivelson. Importance of phase fluctuations in superconductors with small superfluid density. *Nature*, 374:434–437, 1995.

[10] Hiroshi Maeda, Yoshiaki Tanaka, Masao Fukutomi, and Toshihisa Asano. A new high-T_c oxide superconductor without a rare earth element. *Japanese Journal of Applied Physics*, 27:L209–L210, 1988.

[11] M A Subramanian, C C Torardi, J C Calabrese, J Gopalakrishnan, K J Morrissey, T R Askew, R B Flippen, U Chowdhry, and A W Sleight. A new high-temperature superconductor: $Bi_2Sr_{3-x}Ca_xCu_2O_{8+y}$. *Science*, 239:1015–7, 1988.

[12] D Larbalestier, A Gurevich, D M Feldmann, and A Polyanskii. High-T_c superconducting materials for electric power applications. *Nature*, 414:368–77, 2001.

[13] I. Chong, Z. Hiroi, M. Izumi, J. Shimoyama, Y. Nakayama, K. Kishio, T. Terashima, Y. Bando, and M. Takano. High critical-current density in the heavily Pb-doped $Bi_2Sr_2CaCu_2O_{8+x}$ superconductor: Generation of efficient pinning centers. *Science*, 276:770–773, 1997.

[14] H. L. Edwards, J. T. Markert, and A. de Lozanne. Surface structure of $YBa_2Cu_3O_{7-x}$ probed by reversed-bias scanning tunneling microscopy. *Journal of Vacuum Science & Technology B: Microelectronics and Nanometer Structures*, 12:1886, 1994.

[15] S. H. Pan, E. W. Hudson, and J. C. Davis. $_3$He refrigerator based very low temperature scanning tunneling microscope. *Review of Scientific Instruments*, 70:1459, 1999.

[16] Makoto Maki, Terukazu Nishizaki, Kenji Shibata, and Norio Kobayashi. Identification of atomic layers of $YBa_2Cu_3O_{7-\delta}$ by scanning tunneling microscopy and spectroscopy. *Journal of the Physical Society of Japan*, 70:1877–1880, 2001.

[17] T. Nishizaki, K. Shibata, M. Maki, and N. Kobayashi. Vortex phase transition and oxygen vacancy in $YBa_2Cu_3O_y$ single crystals. *Journal of Low Temperature Physics*, 131:931–940, 2003.

[18] H. Edwards, J. Markert, and A. de Lozanne. Energy gap and surface structure of $YBa_2Cu_3O_{7-x}$ probed by scanning tunneling microscopy. *Physical Review Letters*, 69:2967–2970, 1992.

[19] H. Edwards, A. Barr, J. Markert, and A. de Lozanne. Modulations in the CuO chain layer of $YBa_2Cu_3O_{7-\delta}$: Charge density waves? *Physical Review Letters*, 73:1154–1157, 1994.

[20] Makoto Maki, Terukazu Nishizaki, Kenji Shibata, and Norio Kobayashi. Electronic structure of the CuO-chain layer in $YBa_2Cu_3O_{7-\delta}$ studied by scanning tunneling microscopy. *Physical Review B*, 65:140511, 2002.

[21] Yoichi Kamihara, Takumi Watanabe, Masahiro Hirano, and Hideo Hosono. Iron-based layered superconductor $La[O_{1-x}F_x]FeAs$ (x=0.05-0.12) with T_c = 26 K. *Journal of the American Chemical Society*, 130:3296–7, 2008.

[22] D. N. Basov and Andrey V. Chubukov. Manifesto for a higher T_c. *Nature Physics*, 7:272–276, 2011.

[23] David C. Johnston. The puzzle of high temperature superconductivity in layered iron pnictides and chalcogenides. *Advances in Physics*, 59:803–1061, 2010.

[24] G. Stewart. Superconductivity in iron compounds. *Reviews of Modern Physics*, 83:1589–1652, 2011.

[25] K Deguchi, Y Mizuguchi, Y Kawasaki, T Ozaki, S Tsuda, T Yamaguchi, and Y Takano. Alcoholic beverages induce superconductivity in $FeTe_{1x}Se_x$. *Superconductor Science and Technology*, 24:055008, 2011.

[26] Zheng Wei, Hai'ou Li, WeiLi Hong, Zhangming Lv, Huiyan Wu, Xiufeng Guo, and Keqing Ruan. Superconductivity at 57.3 K in La-doped iron-based layered compound $Sm_{0.95}La_{0.05}O_{0.85}F_{0.15}FeAs$. *Journal of Superconductivity and Novel Magnetism*, 21:213–215, 2008.

[27] Shaolong He, Junfeng He, Wenhao Zhang, Lin Zhao, Defa Liu, Xu Liu, Daixiang Mou, Yun-Bo Ou, Qing-Yan Wang, Zhi Li, Lili Wang, Yingying Peng, Yan Liu, Chaoyu Chen, Li Yu, Guodong Liu, Xiaoli Dong, Jun Zhang, Chuangtian Chen, Zuyan Xu, Xi Chen, Xucun Ma, Qikun Xue, and X. J. Zhou. Phase diagram and high temperature superconductivity at 65 K in tuning carrier concentration of single-layer FeSe films. 1207.6823, 2012.

[28] G. Binnig, H. Rohrer, Ch. Gerber, and E. Weibel. Surface studies by scanning tunneling microscopy. *Phys. Rev. Lett.*, 49:57–61.

[29] J. Bardeen. Tunnelling from a many-particle point of view. *Phys. Rev. Lett.*, 6:57–59, Jan 1961.

[30] J. Tersoff and D. R. Hamann. Theory of the scanning tunneling microscope. *Phys. Rev. B*, 31:805–813, 1985.

[31] Jian-Xin Li, Chang-Qin Wu, and Dung-Hai Lee. Checkerboard charge density wave and pseudogap of high-T_c cuprate. *Phys. Rev. B*, 74:184515, 2006.

[32] J. Zaanen and O. Gunnarsson. Charged magnetic domain lines and the magnetism of high-T_c oxides. *Phys. Rev. B*, 40:7391–7394, 1989.

[33] S. A. Kivelson, E. Fradkin, and V. J. Emery. Electronic liquid-crystal phases of a doped mott insulator. *Nature*, 393:550–553, 1998.

[34] Sudip Chakravarty, R. Laughlin, Dirk Morr, and Chetan Nayak. Hidden order in the cuprates. *Physical Review B*, 63:094503, 2001.

[35] C. M. Varma. Non-fermi-liquid states and pairing instability of a general model of copper oxide metals. *Physical Review B*, 55:14554–14580, 1997.

[36] A. Kaminski, S. Rosenkranz, H. M. Fretwell, J. C. Campuzano, Z. Li, H. Raffy, W. G. Cullen, H. You, C. G. Olson, C. M. Varma, and H Höchst. Spontaneous breaking of time-reversal symmetry in the pseudogap state of a high-T_c superconductor. *Nature*, 416:610–3, 2002.

[37] Makoto Hashimoto, Rui-Hua He, Kiyohisa Tanaka, Jean-Pierre Testaud, Worawat Meevasana, Rob G. Moore, Donghui Lu, Hong Yao, Yoshiyuki Yoshida, Hiroshi Eisaki, Thomas P. Devereaux, Zahid Hussain, and Zhi-Xun Shen. Particle–hole symmetry breaking in the pseudogap state of Bi2201. *Nature Physics*, 6:414–418, 2010.

[38] J. E. Hoffman, E. W. Hudson, K. M. Lang, V. Madhavan, H. Eisaki, S. Uchida, and J. C. Davis. A four unit cell periodic pattern of quasi-particle states surrounding vortex cores in $Bi_2Sr_2CaCu_2O_{8+\delta}$. *Science*, 295:466–9, 2002.

[39] C Howald, H Eisaki, N Kaneko, and A Kapitulnik. Coexistence of periodic modulation of quasiparticle states and superconductivity in $Bi_2Sr_2CaCu_2O_{8+\delta}$. *Proceedings of the National Academy of Sciences of the United States of America*, 100:9705–9, 2003.

[40] Michael Vershinin, Shashank Misra, S. Ono, Y. Abe, Yoichi Ando, and Ali Yazdani. Local ordering in the pseudogap state of the high-T_c superconductor $Bi_2Sr_2CaCu_2O_{8+\delta}$. *Science*, 303:1995–1998, 2004.

[41] K. McElroy, D.-H. Lee, J. Hoffman, K. Lang, J. Lee, E. Hudson, H. Eisaki, S. Uchida, and J. Davis. Coincidence of checkerboard charge order and antinodal state decoherence in strongly underdoped superconducting $Bi_2Sr_2CaCu_2O_{8+\delta}$. *Physical Review Letters*, 94:197005, 2005.

[42] W. D. Wise, M. C. Boyer, Kamalesh Chatterjee, Takeshi Kondo, T. Takeuchi, H. Ikuta, Yayu Wang, and E. W. Hudson. Charge-density-wave origin of cuprate checkerboard visualized by scanning tunnelling microscopy. *Nature Physics*, 4:696–699, 2008.

[43] M. J. Lawler, K. Fujita, J. Lee, A. R. Schmidt, Y. Kohsaka, C. K. Kim, H. Eisaki, S. Uchida, J. C. Davis, J. P. Sethna, and E. A. Kim. Intra-unit-cell electronic nematicity of the high-T_c copper-oxide pseudogap states. *Nature*, 466:347–351, 2010.

[44] W. D. Wise, Kamalesh Chatterjee, M. C. Boyer, Takeshi Kondo, T. Takeuchi, H. Ikuta, Zhijun Xu, J. S. Wen, G. D. Gu, Yayu Wang, and E. W. Hudson. Imaging nanoscale fermi-surface variations in an inhomogeneous superconductor. *Nature Physics*, 5:213–216, 2009.

[45] Colin V. Parker, Pegor Aynajian, Eduardo H. da Silva Neto, Aakash Pushp, Shimpei Ono, Jinsheng Wen, Zhijun Xu, Genda Gu, and Ali Yazdani. Fluctuating stripes at the onset of the pseudogap in the high-T_c superconductor $Bi_2Sr_2CaCu_2O_{8+x}$. *Nature*, 468:677–680, 2010.

[46] Roman Gladyshevskii, Nicolas Musolino, and René Flükiger. Structural origin of the low superconducting anisotropy of $Bi_{1.7}Pb_{0.4}Sr_2Ca_{0.9}Cu_2O_8$ crystals. *Physical Review B*, 70:184522, 2004.

[47] Jinho Lee, M. P. Allan, M. A. Wang, J. Farrell, S. A. Grigera, F. Baumberger, J. C. Davis, and A. P. Mackenzie. Heavy *d*-electron quasiparticle interference and real-space electronic structure of $Sr_3Ru_2O_7$. *Nature Physics*, 5:800–804, 2009.

[48] Tess L. Williams. *Nanoscale Electronic Structure of Cuprate Superconductors Investigated with Scanning Tunneling Spectroscopy*. PhD thesis, Harvard University, 2011.

[49] M Presland, J Tallon, R Buckley, R Liu, and N Flower. General trends in oxygen stoichiometry effects on T_c in Bi and Tl superconductors. *Physica C: Superconductivity*, 176:95–105, 1991.

[50] Jennifer E Hoffman. Spectroscopic scanning tunneling microscopy insights into Fe-based superconductors. *Reports on Progress in Physics*, 74:124513, 2011.

[51] Xiaobo He, Guorong Li, Jiandi Zhang, A. Karki, Rongying Jin, B. Sales, A. Sefat, M. McGuire, D. Mandrus, and E. Plummer. Nanoscale chemical phase separation in $FeTe_{0.55}Se_{0.45}$ as seen via scanning tunneling spectroscopy. *Physical Review B*, 83:220502, 2011.

[52] K. M. Lang, V. Madhavan, J. E. Hoffman, E. W. Hudson, H. Eisaki, S. Uchida, and J. C. Davis. Imaging the granular structure of high-T_c superconductivity in underdoped $Bi_2Sr_2CaCu_2O_{8+\delta}$. *Nature*, 415:412–6, 2002.

[53] M. C. Boyer, W. D. Wise, Kamalesh Chatterjee, M. Yi, Takeshi Kondo, T. Takeuchi, H. Ikuta, and E. W. Hudson. Imaging the two gaps of the high-temperature superconductor $Bi_2Sr_2CuO_{6+x}$. *Nature Physics*, 3:802–806, 2007.

[54] Aakash Pushp, Colin V. Parker, Abhay N. Pasupathy, Kenjiro K. Gomes, Shimpei Ono, J. S. Wen, Zhijun Xu, Genda Gu, and Ali Yazdani. Extending universal nodal excitations optimizes superconductivity in $Bi_2Sr_2CaCu_2O_{8+\delta}$. *Science*, 324:1689–93, 2009.

[55] R.-H. He, M. Hashimoto, H. Karapetyan, J. D. Koralek, J. P. Hinton, J. P. Testaud, V. Nathan, Y. Yoshida, H. Yao, K. Tanaka, W. Meevasana, R. G. Moore, D. H. Lu, S.-K. Mo, M. Ishikado, H. Eisaki, Z. Hussain, T. P. Devereaux, S. a. Kivelson, J. Orenstein, A. Kapitulnik, and Z.-X. Shen. From a single-band metal to a high-temperature superconductor via two thermal phase transitions. *Science*, 331(6024):1579–1583, 2011.

[56] Takeshi Kondo, Rustem Khasanov, Tsunehiro Takeuchi, Jörg Schmalian, and Adam Kaminski. Competition between the pseudogap and superconductivity in the high-T_c copper oxides. *Nature*, pages 296–300.

[57] Y. Kohsaka, C. Taylor, P. Wahl, A. R. Schmidt, Jhinhwan Lee, K. Fujita, J. W. Alldredge, K. McElroy, Jinho Lee, H. Eisaki, S. Uchida, D.-H. Lee, and J. C. Davis. How cooper pairs vanish approaching the mott insulator in $Bi_2Sr_2CaCu_2O_{8+\delta}$. *Nature*, 454:1072–1078, 2008.

[58] J. E. Hoffman, K. McElroy, D.-H. Lee, K. M. Lang, H. Eisaki, S. Uchida, and J. C. Davis. Imaging quasiparticle interference in $Bi_2Sr_2CaCu_2O_{8+\delta}$. *Science (New York, N.Y.)*, 297:1148–51, 2002.

[59] V. J. Emery, S. A. Kivelson, and O. Zachar. Spin-gap proximity effect mechanism of high-temperature superconductivity. *Physical Review B*, 56:6120–6147, 1997.

[60] I Martin and A. V. Balatsky. Doping-induced inhomogeneity in high-T_c superconductors. *Physica C: Superconductivity*, 357-360:46–48, 2001.

[61] K. McElroy, Jinho Lee, J. A. Slezak, D.-H. Lee, H. Eisaki, S. Uchida, and J. C. Davis. Atomic-scale sources and mechanism of nanoscale electronic disorder in $Bi_2Sr_2CaCu_2O_{8+\delta}$. *Science (New York, N.Y.)*, 309:1048–52, 2005.

[62] Tamara S. Nunner, Brian M. Andersen, Ashot Melikyan, and P. J. Hirschfeld. Dopant-modulated pair interaction in cuprate superconductors. *Phys. Rev. Lett.*, 95:177003, 2005.

[63] Wei Chen, Marc Gabay, and P J Hirschfeld. Doping dependence of gap inhomogeneities at $Bi_2Sr_2CaCu_2O_{8+\delta}$ surfaces. *New J. of Phys.*, 14:033004, 2012.

[64] Sen Zhou, Hong Ding, and Ziqiang Wang. Correlating off-stoichiometric doping and nanoscale electronic inhomogeneity in the high-T_c superconductor $Bi_2Sr_2CaCu_2O_{8+\delta}$. *Physical Review Letters*, 98:076401, 2007.

[65] D. B. Mitzi, L. W. Lombardo, A. Kapitulnik, S. S. Laderman, and R. D. Jacowitz. Growth and properties of oxygen- and ion-doped $Bi_2Sr_2CaCu_2O_{8+\delta}$ single crystals. *Phys. Rev. B*, 41:6564–6574, 1990.

[66] T. Hanaguri, Y. Kohsaka, J. C. Davis, C. Lupien, I. Yamada, M. Azuma, M. Takano, K. Ohishi, M. Ono, and H. Takagi. Quasiparticle interference and superconducting gap in $Ca_{2x}Na_xCuO_2Cl_2$. *Nature Physics*, 3:865–871, 2007.

[67] H. Eisaki, N. Kaneko, D. Feng, A. Damascelli, P. Mang, K. Shen, Z.-X. Shen, and M. Greven. Effect of chemical inhomogeneity in bismuth-based copper oxide superconductors. *Physical Review B*, 69:064512, 2004.

[68] G. Kinoda and T. Hasegawa. Observations of electronic inhomogeneity in heavily Pb-doped $Bi_2Sr_2CaCu_2O_y$ single crystals by scanning tunneling microscopy. *Physical Review B*, 67:224509, 2003.

[69] Jennifer E. Hoffman. *A Search for Alternative Electronic Order in the High Temperature Superconductor BSCCO by Scanning Tunneling Microscopy*. PhD thesis, University of California at Berkeley, 2003.

[70] H. Mashima, N. Fukuo, Y. Matsumoto, T. Kondo, H. Ikuta, T. Hitosugi, and T. Hasegawa. Electronic inhomogeneity of heavily overdoped $Bi_{2x}Pb_xSr_2CuO_y$ studied by low-temperature scanning tunneling microscopy/spectroscopy. *Physical Review B*, 73:060502, 2006.

[71] D. Zech, H. Keller, K. Conder, E. Kaldis, E. Liarokapis, N. Poulakis, and K. A. Müller. Site-selective oxygen isotope effect in optimally doped $YBa_2Cu_3O_{6+x}$. *Nature*, 371:681–683, 1994.

[72] Y. Ohta, T. Tohyama, and S. Maekawa. Apex oxygen and critical temperature in copper oxide superconductors: Universal correlation with the stability of local singlets. *Phys. Rev. B*, 43:2968–2982, 1991.

[73] E. Pavarini, I. Dasgupta, T. Saha-Dasgupta, O. Jepsen, and O. K. Andersen. Band-structure trend in hole-doped cuprates and correlation with t_{cmax}. *Phys. Rev. Lett.*, 87:047003, 2001.

[74] Erez Berg, Dror Orgad, and Steven A. Kivelson. Route to high-temperature superconductivity in composite systems. *Phys. Rev. B*, 78:094509, 2008.

[75] Lilach Goren and Ehud Altman. Enhancement of the critical temperature in cuprate superconductors by inhomogeneous doping. *Physical Review B*, 84:094508, 2011.

[76] E. W. Hudson, S.-H. Pan, A. K. Gupta, K.-W. Ng, and J. C. Davis. Atomic-scale quasi-particle scattering resonances in $Bi_2Sr_2CaCu_2O_{8+\delta}$. *Science*, 285:88–91, 1999.

[77] Ali Yazdani, C. Howald, C. Lutz, A. Kapitulnik, and D. Eigler. Impurity-induced bound excitations on the surface of $Bi_2Sr_2CaCu_2O_8$. *Physical Review Letters*, 83:176–179, 1999.

[78] Y. Le Page, W. McKinnon, J.-M. Tarascon, and P. Barboux. Origin of the incommensurate modulation of the 80-K superconductor $Bi_2Sr_2CaCu_2O_{8.21}$ derived from isostructural commensurate $Bi_{10}Sr_{15}Fe_{10}O_{46}$. *Phys. Rev. B*, 40:6810–6816, 1989.

[79] Akiji Yamamoto, Mitsuko Onoda, Eiji Takayama-Muromachi, Fujio Izumi, Toru Ishigaki, and Hajime Asano. Rietveld analysis of the modulated structure in the superconducting oxide $Bi_2(Sr,Ca)_3Cu_2O_{8+x}$. *Phys. Rev. B*, 42:4228–4239, 1990.

[80] Vaclav Petricek, Yan Gao, Peter Lee, and Philip Coppens. X-ray analysis of the incommensurate modulation in the 2:2:1:2 Bi-Sr-Ca-Cu-O superconductor including the oxygen atoms. *Phys. Rev. B*, 42:387–392, 1990.

[81] A A Levin, Yu I Smolin, and Yu F Shepelev. Causes of modulation and hole conductivity of the high-T_c superconductor $Bi_2Sr_2CaCu_2O_{8+x}$ according to X-ray single-crystal data. *Journal of Physics: Condensed Matter*, 6:3539–3551, 1994.

[82] Y. He, T. S. Nunner, P. J. Hirschfeld, and H.-P. Cheng. Local electronic structure of $Bi_2Sr_2CaCu_2O_8$ near oxygen dopants: A window on the high-T_c pairing mechanism. *Phys. Rev. Lett.*, 96:197002, 2006.

[83] P.A Miles, S.J Kennedy, G.J McIntyre, G.D Gu, G.J Russell, and N Koshizuka. Refinement of the incommensurate structure of high quality Bi-2212 single crystals from a neutron diffraction study. *Physica C: Superconductivity*, 294:275–288, 1998.

[84] J. A. Slezak, Jinho Lee, M Wang, K McElroy, K Fujita, B M Andersen, P J Hirschfeld, H Eisaki, S Uchida, and J C Davis. Imaging the impact on cuprate superconductivity of varying the interatomic distances within individual crystal unit cells. *Proceedings of the National Academy of Sciences of the United States of America*, 105:3203–8, 2008.

[85] J. Frenkel. Die elektrodynamik des rotierenden elektrons. *Zeitschrift fur Physik*, 37:243–262, 1926.

[86] Yunbin He, Olga Dulub, Hongzhi Cheng, Annabella Selloni, and Ulrike Diebold. Evidence for the predominance of subsurface defects on reduced anatase $tio_2(101)$. *Phys. Rev. Lett.*, 102:106105, 2009.

[87] V. Zabolotnyy, S. Borisenko, A. Kordyuk, J. Geck, D. Inosov, A. Koitzsch, J. Fink, M. Knupfer, B. Büchner, S.-L. Drechsler, H. Berger, A. Erb, M. Lambacher, L. Patthey, V. Hinkov, and B. Keimer. Momentum and temperature dependence of renormalization effects in the high-temperature superconductor $YBa_2Cu_3O7\delta$. *Physical Review B*, 76:1–6, 2007.

[88] H. Edwards, D. Derro, A. Barr, J. Markert, and A. de Lozanne. Spatially varying energy gap in the cuo chains of $YBa_2Cu_3O_{7-x}$ detected by scanning tunneling spectroscopy. *Physical Review Letters*, 75:1387–1390, 1995.

[89] D. J. Derro, E. W. Hudson, K. M. Lang, S. H. Pan, J. C. Davis, J. T. Markert, and A. L. de Lozanne. Nanoscale one-dimensional scattering resonances in the CuO chains of $yba_2cu_3O_{6+x}$. *Phys. Rev. Lett.*, 88:097002, 2002.

[90] I. Maggio-Aprile, Ch. Renner, A. Erb, E. Walker, and Ø ystein Fischer. Direct vortex lattice imaging and tunneling spectroscopy of flux lines on $YBa_2Cu_3O_{7-\delta}$. *Physical Review Letters*, 75:2754–2757, 1995.

[91] Ruixing Liang, D. A. Bonn, and W. N. Hardy. Evaluation of cuo_2 plane hole doping in $yba_2cu_3o_{6+x}$ single crystals. *Phys. Rev. B*, 73:180505, 2006.

[92] S. Misra, S. Oh, D. J. Hornbaker, T. DiLuccio, J. N. Eckstein, and A. Yazdani. Atomic scale imaging and spectroscopy of a Cuo_2 plane at the surface of $Bi_2Sr_2CaCu_2O_{8+x}$. *Phys. Rev. Lett.*, 89:087002, 2002.

[93] S.-H. Pan, E. W. Hudson, A. K. Gupta, K.-W. Ng, H. Eisaki, S. Uchida, and J. C. Davis. Stm studies of the electronic structure of vortex cores in $Bi_2Sr_2CaCu_2O_{8+\delta}$. *Physical Review Letters*, 85:1536–1539, 2000.

[94] Y. Yin. *The Investigation of Scanning Tunneling Microscopy and Spectroscopy on High-T_c Superconductors : Cuprates and Pnictides*. PhD thesis, Harvard University, 2009.

[95] R Liang, D.A Bonn, W.N Hardy, J.C Wynn, K.A Moler, L Lu, S Larochelle, L Zhou, M Greven, L Lurio, and S.G.J Mochrie. Preparation and characterization of homogeneous YBCO single crystals with doping level near the SC-AFM boundary. *Physica C: Superconductivity*, 383:1–7, 2002.

[96] S.-H. Pan, E. W. Hudson, K. M. Lang, H. Eisaki, S. Uchida, and J. C. Davis. Imaging the effects of individual zinc impurity atoms on superconductivity in $Bi_2Sr_2CaCu_2O_{8+\delta}$. *Nature*, 403:746–50, 2000.

[97] E. W. Hudson, K. M. Lang, V. Madhavan, S.-H. Pan, H. Eisaki, S. Uchida, and J. C. Davis. Interplay of magnetism and high-T_c superconductivity at individual ni impurity atoms in $Bi_2Sr_2CaCu_2O_{8+\delta}$. *Nature*, 411:920–4, 2001.

[98] E Hudson. Stm study of novel resonances in $Bi_2Sr_2CaCu_2O_{8+\delta}$. *Physica B: Condensed Matter*, 329-333:1365–1366, 2003.

[99] Kamalesh Chatterjee, M. C. Boyer, W. D. Wise, Takeshi Kondo, T. Takeuchi, H. Ikuta, and E. W. Hudson. Visualization of the interplay between high-temperature superconductivity, the pseudogap and impurity resonances. *Nature Physics*, 4:108–111, 2008.

[100] A. V. Balatsky, I. Vekhter, and J.-X. Zhu. Impurity-induced states in conventional and unconventional superconductors. *Reviews of Modern Physics*, 78:373–433, 2006.

[101] M. Salkola, A. Balatsky, and D. Scalapino. Theory of scanning tunneling microscopy probe of impurity states in a *d*-wave superconductor. *Physical Review Letters*, 77:1841–1844, 1996.

[102] H. V. Kruis, I. Martin, and A. V. Balatsky. Impurity-induced resonant state in a pseudogap state of a high-T_c superconductor. *Phys. Rev. B*, 64:054501, Jun 2001.

[103] M. Gao, F. Ma, Z. Y. Lu, and T. Xiang. Surface structures of ternary iron arsenides $A Fe_2As_2$ (A=Ba, Sr, or Ca). *Phys. Rev. B*, 81:193409–, 2010.

[104] V. B. Nascimento, A. Li, D. R. Jayasundara, Y. Xuan, J. O'Neal, S. Pan, T. Y. Chien, B. Hu, X. B. He, G. Li, A. S. Sefat, M. A. McGuire, B. C. Sales, D. Mandrus, M. H. Pan, J. Zhang, R. Jin, and E. W. Plummer. Surface geometric and electronic structures of $BaFe_2As_2(001)$. *Phys. Rev. Lett.*, 103:076104–, 2009.

[105] F. C. Niestemski, V. B. Nascimento, B. Hu, W. Plummer, J. Gillett, S. E. Sebastian, Z. Wang, and V. Madhavan. Unveiling the atomic and electronic structure at the surface of the parent pnictide $SrFe_2As_2$. *arXiv*, 0906.2761, 2009.

[106] Y. B. Huang, P. Richard, J. H. Wang, X. P. Wang, X. Shi, N. Xu, Z. Wu, A. Li, J. X. Yin, T. Qian, B. Lv, C. W. Chu, S. H. Pan, M. Shi, and H. Ding. Experimental investigation of the electronic structure of $Ca_{0.83}La_{0.17}Fe_2As_2$. *arXiv*, 1210.7288, 2012.

[107] F. Massee, S. de Jong, Y. Huang, J. Kaas, E. van Heumen, J. B. Goedkoop, and M. S. Golden. Cleavage surfaces of the $BaFe_{2-x}Co_xAs_2$ and $Fe_ySe_{1-x}Te_x$ superconductors: A combined stm plus leed study. *Phys. Rev. B*, 80:140507–, 2009.

[108] G. Binnig, N. Garcia, H. Rohrer, J. Soler, and F. Flores. Electron-metal-surface interaction potential with vacuum tunneling: Observation of the image force. *Phys. Rev. B*, 30:4816–4818, 1984.

[109] R. Wiesendanger, L. Eng, H. R. Hidber, P. Oelhafen, L. Rosenthaler, U. Staufer, and H. J. Guntherodt. Local tunneling barrier height images obtained with the scanning tunneling microscope. *Surf. Sci.*, 189-190, 1987.

[110] Y. Yamada, A. Sinsarp, M. Sasaki, and S. Yamamoto. Local tunneling barrier height measurement on Au(111). *Jap. J. App. Phys.*, 42:4898–4900, 2003.

[111] Roland Wiesendanger. *Scanning probe microscopy and spectroscopy*. Cambridge University Press, 1994.

[112] F. Massee. *A tunneler's view on correlated oxides and iron based superconductors*. PhD thesis, University of Amsterdam, Amsterdam, The Netherlands, 2011.

[113] J. F. Jia, K. Inoue, Y. Hasegawa, W. S. Yang, and T. Sakurai. Variation of the local work function at steps on metal surfaces studied with stm. *Phys. Rev. B*, 58:1193–1196, 1998.

[114] James Speight. *Lange's Handbook of Chemistry*. McGraw-Hill, 16$^{\text{th}}$ ed. edition, 2005.

[115] E. Wigner and J. Bardeen. Theory of the work functions of monovalent metals. *Phys. Rev.*, 48:84–87, 1935.

[116] Can-li Song, Yi Yin, Martin Zech, Tess Williams, Michael Yee, Gen-Fu Chen, Jian-lin Luo, Nan-lin Wang, Eric W Hudson, and Jennifer E Hoffman. Electronic inhomogeneity and vortex disorder in superconducting $Sr_{0.75}K_{0.25}Fe_2As_2$. 1212.3240, 2012.

[117] R. Smoluchowski. Anisotropy of the electronic work function of metals. *Phys. Rev.*, 60:661–674, 1941.

[118] M. C. Boyer, K. Chatterjee, W. D. Wise, G. F. Chen, J. L. Luo, N. L. Wang, and E. W. Hudson. Scanning tunneling microscopy of the 32 K superconductor $Sr_{1-x}K_xFe_2As_2$. *arXiv*, 0806.4400, 2008.

[119] T-M Chuang, M P Allan, Jinho Lee, Yang Xie, Ni Ni, S L Bud'ko, G S Boebinger, P C Canfield, and J C Davis. Nematic electronic structure in the "parent" state of the iron-based superconductor $Ca(Fe_{1-x}Co_x)_2As_2$. *Science (New York, N.Y.)*, 327:181–4, 2010.

[120] M. Rotter, M. Tegel, and D. Johrendt. Superconductivity at 38 K in the iron arsenide $Ba_{1-x}K_xFe_2As_2$. *Phys. Rev. Lett.*, 101:107006–, 2008.

[121] Yasuyuki Nakajima, Toshihiro Taen, and Tsuyoshi Tamegai. Possible superconductivity above 25 K in single-crystalline Co-doped $BaFe_2As_2$. *Journal of the Physical Society of Japan*, 78:023702, 2009.

[122] S. Saha, N. Butch, T. Drye, J. Magill, S. Ziemak, K. Kirshenbaum, P. Zavalij, J. Lynn, and J. Paglione. Structural collapse and superconductivity in rare-earth-doped $CaFe_2As_2$. *Physical Review B*, 85:024525, 2012.

[123] Bing Lv, Liangzi Deng, Melissa Gooch, Fengyan Wei, Yanyi Sun, James K Meen, Yu-Yi Xue, Bernd Lorenz, and Ching-Wu Chu. Unusual superconducting state at 49 K in electron-doped $CaFe_2As_2$ at ambient pressure. *Proceedings of the National Academy of Sciences of the United States of America*, 108:15705–9, 2011.

[124] S. Kasahara, T. Shibauchi, K. Hashimoto, Y. Nakai, H. Ikeda, T. Terashima, and Y. Matsuda. Abrupt recovery of Fermi-liquid transport following the collapse of the *c* axis in $CaFe_2(As_{1-x}P_x)_2$ single crystals. *Phys. Rev. B*, 83:060505–, 2011.

[125] R. D. Shannon. Revised effective ionic radii and systematic studies of interatomic distances in halides and chalcogenides. *Acta Crystall. A*, 32:751–767, 1976.

[126] S. Grothe, Shun Chi, P. Dosanjh, Ruixing Liang, W. Hardy, S. Burke, D. Bonn, and Y. Pennec. Bound states of defects in superconducting lifeas studied by scanning tunneling spectroscopy. *Physical Review B*, 86:174503, 2012.

[127] A R Schmidt, M H Hamidian, P Wahl, F Meier, a V Balatsky, J D Garrett, T J Williams, G M Luke, and J C Davis. Imaging the fano lattice to 'hidden order' transition in URu_2Si_2. *Nature*, 465:570–6, 2010.

[128] Pegor Aynajian, Eduardo H da Silva Neto, András Gyenis, Ryan E Baumbach, J D Thompson, Zachary Fisk, Eric D Bauer, and Ali Yazdani. Visualizing heavy fermions emerging in a quantum critical kondo lattice. *Nature*, 486:201–6, 2012.

[129] J. W. Alldredge, Jinho Lee, K. McElroy, M. Wang, K. Fujita, Y. Kohsaka, C. Taylor, H. Eisaki, S. Uchida, P. J. Hirschfeld, and J. C. Davis. Evolution of the electronic excitation spectrum with strongly diminishing hole density in superconducting $Bi_2Sr_2CaCu_2O_{8+\delta}$. *Nat. Phys.*, 4:319–326, 2008.

[130] J. W. Alldredge, K. Fujita, H. Eisaki, S. Uchida, and Kyle McElroy. Three-component electronic structure of the cuprates derived from spectroscopic-imaging scanning tunneling microscopy. *Phys. Rev. B*, 85:174501, 2012.